FRACTURED RESERVOIR POTENTIAL AND TECTONIC DEVELOPMENT OF THE INISKIN – TUXEDNI REGION, LOWER COOK INLET, ALASKA

By

Jacob L. Rosenthal, B. S.

A Thesis Submitted in Partial Fulfillment of the Requirements

For the Degree of

Master of Science

in

Geology

University of Alaska Fairbanks

December 2016

APPROVED:

Elisabeth Nadin, Ph.D., Committee Chair
Anupma Prakash, Ph.D., Committee Co-Chair
Paul Betka, Ph.D., Committee Member
Robert Gillis, M.Sc., Committee Member
Paul McCarthy, Ph.D., Chair
Department of Geosciences
Paul Layer, Ph.D., Dean
College of Natural Science and Mathematics
Michael Castellini, Ph.D., Dean
Dean of the Graduate School

Abstract

Fracture patterns can provide insight into the strain history and stress evolution of deformed strata. In southern Alaska's Cook Inlet forearc basin, hydrocarbon traps are typically fault-cored anticlines, where fractures likely aid in the migration of hydrocarbons from lower Jurassic marine strata into Cenozoic non-marine deposits. Consequently, understanding the distribution and orientation of fracture sets with respect to these structures is necessary to improving the understanding of one of Alaska's largest petroleum provinces. Furthermore, recent refinements in understanding southern Alaska's Dynamic Cenozoic tectonic evolution allow us to interpret fractures in a regional tectonic context. Despite the important role fractures likely play in the Cook Inlet petroleum system, limited work exists linking fractures to regional tectonic events and structures.

The objective of chapter one is to characterize from field and remote sensing observations the orientations, distributions, and relative ages of several regionally prominent fracture sets. Field observations focus on the area of the western Cook Inlet near Augustine Volcano, north to Tuxedni Bay. Remote sensing observations expand the study area from the Alaska Peninsula in the south to Mount Spurr in the north. I identified four fracture sets—with common orientations, opening modes, and relative ages—within the sedimentary sequence that spans early Jurassic to Miocene time in the Cook Inlet forearc basin. Within the field area, these sets fall into two structural domains: 1) the Iniskin Peninsula, site of an anticline–syncline pair and reverse slip on the SW-striking Bruin Bay fault; and 2) north of Chinitna Bay, where the Bruin Bay fault strikes ~N–S and preserves primarily sinistral displacement.

Chapter two is aimed at quantifying the fracture intensity of the four regional fracture sets defined in Chapter 1, which are pervasive in deformed forearc basin strata of Jurassic age in the Iniskin–Tuxedni region of the lower Cook Inlet, Alaska. I document how fracture intensity changes between the four regionally identified fracture sets of chapter one. Analysis of fracture intensity indicates that changes in fracture intensity are guided by the opening of other fractures and grain size. I also measured fractures at the thin-section scale, via back-scattered electron microscopy, to test the feasibility of using micro fracture analysis to estimate macro fracture abundance.

I conclude by discussing how natural fractures could enhance sub-surface permeability for the lower Cook Inlet hydrocarbon province; and serve as migration pathways in the lower and upper Cook Inlet petroleum systems.

Table of Contents

Page

List of Figures

Page

List of Tables

Page

Acknowledgments

I would like to acknowledge the help of my advisors Paul Betka and Elisabeth Nadin for their assistance in the creation of this document. Their feedback has been invaluable in my growth as a scientist. Paul's assistance in planning and executing fieldwork, as well as his mentoring in the field was extremely helpful. Additional assistance from my other committee members Robert Gillis and Anupma Prakash has been greatly beneficial. The Alaska Division of Geological and Geophysical Surveys provided partial support of this thesis through providing a year of a research assistantship, field support and logistics, and mentorship through their Cook Inlet basin analysis program, and without this support this study would not have been possible. I would also like to thank Jeff Benowitz, Robert Gillis, and Marwan Wartes for their advice in constructive discussions regarding Alaska tectonics. This thesis and the work contained within unless otherwise cited is that of the author. This document was improved greatly from substantial reviews from Paul Betka, Robert Gillis, and Elisabeth Nadin.

0. Introduction

Importance of Fractures

Tectonics

Sediment filling forearc basins can provide a record of subsidence and exhumation driven by convergent margin tectonics. The tectonic processes by which such basins evolve are understood by interpreting the style and chronology of preserved structures that deform them. This is particularly true for long-lived continental subduction margins, which can undergo a host of deformational events such as accretion, subduction erosion, and/or subduction of aseismic or actively spreading ridges. Structural studies in forearc settings often focus on major fault and fold systems that deform the basins and their margins (e.g., Dickinson and Seely, 1979; Haeussler et al., 2000; Trop et al., 2005). Less well studied at these sites is the evolution of fracture systems that are associated with development of local and regional structures and that record changes in the regional state of stress with time. Fractures —expressed as mode I, II, or III—preserve the stress history of the hosting rock body at the time of deformation (e.g., Hancock, 1985). Furthermore, these fractures create mechanical anisotropies (gaps) within the hosting rock body (e.g., Hancock, 1985) that not only create pathways for subsurface fluid flow, but lead to fracture abutment, or the prevention of subsequent tensile brittle deformation (fractures) from propagating across the gaps. These abutting relationships preserve the sequential timing of fracture formation within the host rock. To determine the tectonic history of the lower Cook Inlet region, I combine local stress histories determined from observed fracture orientations with relative timing constraints obtained from abutting and cross cutting relationships, and interpret these in the context of published regional tectonic interpretations (e.g., Lacombe et al., 2011; Branellec et al., 2015).

Fractured reservoirs associated with folding in collisional environments can create large oil fields (Lacombe et al., 2011; Stephenson et al., 2007). Fault-cored folds of the upper Cook Inlet form hydrocarbon reservoirs (e.g., Kirschner and Lyon, 1973, Bruhn and Haeussler, 2006; Stanley et al., 2011). Because folds can serve as significant hydrocarbon traps, and fractures can enhance permeability in folded rocks, many studies have addressed the relationships between folding and the timing, orientations, and types of fractures that develop in them (e.g., Lacombe et al., 2011; Bellahsen et al., 2006; Branellec et al., 2015; Ahmadhadi et al., 2007; Price, 1966; Hancock, 1985). Fracture patterns with regional trends can provide insight into regional stress fields prior to or at the onset of folding (Engelder and Geiser, 1980; Engelder et al., 2009; Ahmadhadi et al., 2008; Lacombe et al., 2011; Branellec et al.,

2015; Weil and Yonkee, 2012). Fold-related fractures have been modeled by numerous authors to predict or understand the orientation of fractures that form during folding (e.g., Price, 1966; Friedman, 1969; Hancock, 1985; Amrouch et al., 2010; Ahmadhadi et al., 2007; Bellahsen et al., 2006; Lacombe et al., 2011; Branellec et al., 2015). Models from field-based observations predict that four fracture sets will occur: (J1) a tensile set perpendicular to the fold axis; (J3, J4) a conjugate pair that shares the same shortening direction as the first tensile set; and (J2) a final tensile set that opens parallel to the fold axis during flexure of the outer layers (Figure 0.1; e.g., Price, 1966; Stearns and Friedman, 1972; Hancock, 1985). However, the predicted model sometimes fails to explain more complex orientations or opening modes of fracture sets observed in the field (e.g., Bergbauer and Pollard, 2004; Amrouch et al., 2010; Ahmadhadi et al., 2008; Bellahsen et al., 2006; Lacombe et al., 2011; Branellec et al., 2015). Bergbauer and Pollard (2004) explain

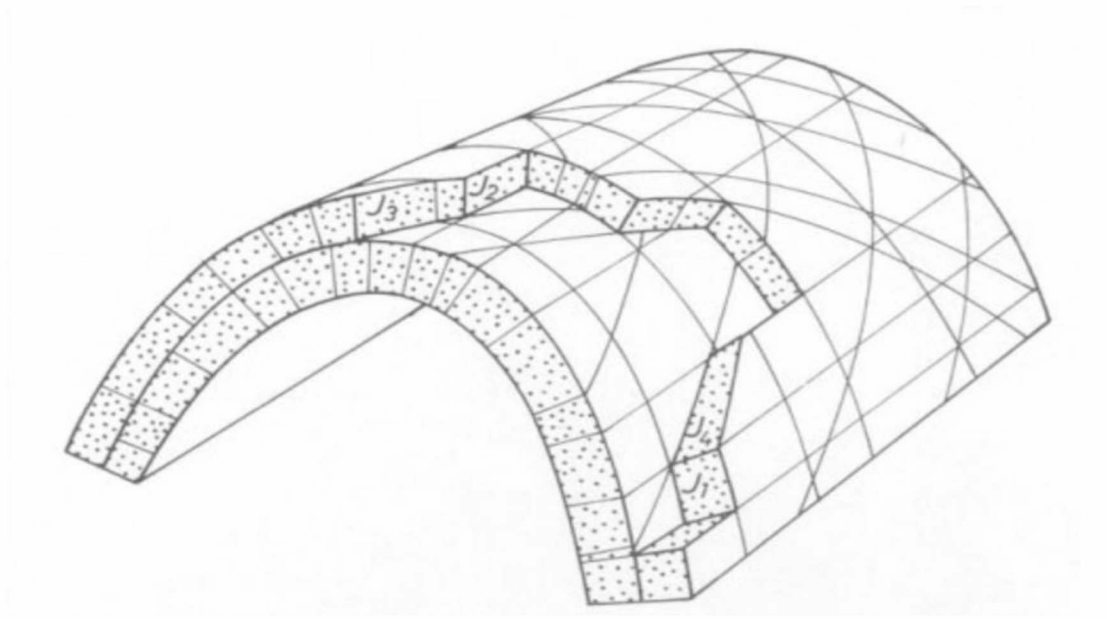

Figure 0.1 Predicted fold fracture relationships from Ramsey and Huber (1987). See text for discussion of labeled fractures (J1-J4)

this incongruity with the suggestion that fractures that pre-date folding create mechanical anisotropies that influence the orientations and types of subsequent fracture sets. Therefore, when trying to predict the orientations and densities of fractures sets with respect to folds, knowing the sequential development of these fractures is vital. My study aims to establish timing relationships of fractures in order to determine if they could have developed during folding in lower Cook Inlet.

Petroleum

Fractures control the movement of basinal fluids and serve as a secondary source of permeability in reservoir rocks where primary porosity and permeability have been lost due to diagenesis (e.g., Engelder et al., 2009; Lianbo and Xiang-Yang, 2009; Ortega et al., 2010). On Alaska's Iniskin Peninsula and surrounding areas within the lower Cook Inlet forearc basin, such fractures control the locations of oil shows and seeps, as well as the migration of hydrocarbons (Lepain et al., 2013; AOGCC, 2015; Detterman and Hartsock, 1966). Despite the rarity of forearc petroleum systems (Dickinson, 1995), economic potential in low primary porosity and primary permeability reservoirs such as the Mesozoic rocks of the Cook Inlet could be realized with properly placed well bores that more effectively exploit fracture networks (e.g., Engelder et al., 2009). Therefore, clarifying fracture types, orientations, and controls on fracture density are critical to further regional petroleum exploration and production in tight rocks.

Fracture intensity (the number of fractures per unit length), the relationship of fractures to local anticlinal traps, and the orientations of regional fracture sets are important parameters in the characterization of fractured reservoirs. The normalized fracture intensity (the number of fractures of a given size or larger per unit length) is a scale-independent quantity for predicting the density and size distributions of a fracture set. Therefore, normalized fracture intensity can be used to evaluate how properties such as grain size, facies, or structural position control the density of a fracture set (e.g., Ortega et al., 2010). Because large fractures control the migration of fluids in basins with low-porosity rocks (e.g., Laubach, 1997), understanding the parameters that control size-normalized fracture intensity is crucial to characterizing fluid flow in reservoirs with poor primary porosity and permeability. Previous workers have determined that the primary controls on fracture intensity are stratigraphic and structural position, rock type, and rock texture (e.g., Narr, 1996; Nelson, 1985; Ortega et al., 2010). Fracture intensity seems to correlate well with grain size (Sinclair, 1980; Lianbo and Xiang-Yang, 2009). Lianbo and Xiang-Yang (2009) demonstrated that fractures in immature clastic rocks correlate strongest with grain size, and that despite heavy diagenetic alteration, such rocks can serve as good fractured reservoirs. I seek to establish if additional textural controls (such as grain size) correlate with observed fracture intensity at outcrop scale in the arc-derived immature clastic rocks of the lower Cook Inlet. With further refinement of factors leading to fracture formation, I can better constrain which formations would be suitable for further exploration. Using a size-normalized approach for modeling fracture intensity following methods after Ortega et al. (2006), this study will determine the controls on fracture

intensity throughout the field area. This size-normalized approach allows for objective comparison between lithologies, structural and stratigraphic position, and textures of rocks in various locations.

Objectives

The principle objectives of this study were to interpret (1) how the orientations of numerous fracture sets in the lower Cook Inlet region are related to local structures and regional tectonic events, and (2) how the fracture intensities play a role in the potential fluid reservoir quality of the basin.

Research Questions

This study addresses three primary questions:

1. What was the relative timing of deformation in the Cook Inlet, did the fractures develop in tandem with local structures, and what were the major tectonic driver(s) for deformation in the area?
2. What controls fracture intensity within the fractured Mesozoic strata of Cook Inlet?
3. What role do fractures play in the unconventional fractured resource potential of the region?

I address these questions in the following two chapters. The first addresses the orientations, spatial distribution, and tectonic history of several fracture sets in the region. The second chapter addresses the density and fracture intensity of the fracture sets identified in the region.

Geologic Background

Tectonic Setting

Southern Alaska is composed of an amalgamation of allochthonous terranes, sedimentary basins, magmatic belts, and subduction complex materials that were accreted to the North American margin during Mesozoic and Cenozoic time (e.g., Plafker et al., 1989; Plafker and Berg, 1994; Trop and Ridgway, 2007). Within this series of geological elements lies the Cook Inlet basin, a northeast-trending collisional forearc basin located between the Mesozoic and early Cenozoic Talkeetna arc and modern Aleutian Arc to the northwest—representing sporadic arc magmatism since Mesozoic time—and the Aleutian trench and a massive accretionary prism to the southeast (Nokleberg et al., 1994). The Cook Inlet forearc is a long-lived sedimentary basin, with rocks spanning late Paleozoic to modern time, with several major unconformities.

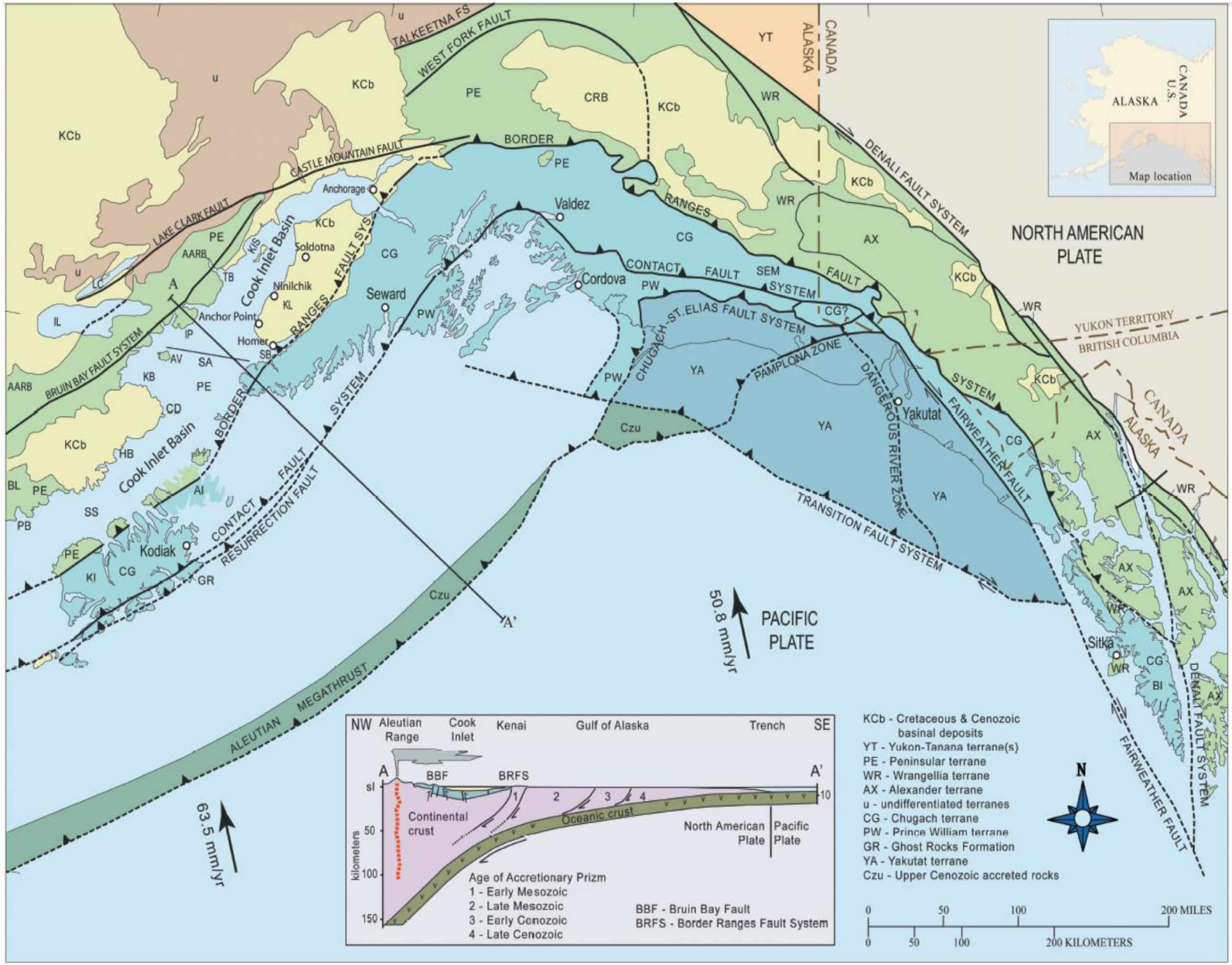
TALKEETNA FS
WEST FORK FAULT
CASTLE MOUNTAIN FAULT
LAKE CLARK FAULT
BORDER RANGES FAULT SYSTEM
CONTACT FAULT SYSTEM
CHUGACH-ST. ELIAS FAULT SYSTEM
PAMPLONA ZONE
DANGEROUS RIVER ZONE
FAIRWEATHER FAULT SYSTEM
TRANSITION FAULT SYSTEM
DENALI FAULT SYSTEM
BRUIN BAY FAULT SYSTEM
RESURRECTION FAULT
ALEUTIAN MEGATHRUST
NORTH AMERICAN PLATE
PACIFIC PLATE
50.8 mm/yr
63.5 mm/yr
CANADA
ALASKA
YUKON TERRITORY
BRITISH COLUMBIA
Anchorage
Valdez
Cordova
Seward
Soldotna
Anchor Point
Homer
Ninilchik
Kodiak
Yakutat
Sitka
Cook Inlet Basin
Map location
NW Aleutian Range Cook Inlet Kenai Gulf of Alaska Trench SE
Continental crust
Oceanic crust
North American Plate
Pacific Plate
Age of Accretionary Prizm
1 - Early Mesozoic
2 - Late Mesozoic
3 - Early Cenozoic
4 - Late Cenozoic
BBF - Bruin Bay Fault
BRFS - Border Ranges Fault System
KCb - Cretaceous & Cenozoic basinal deposits
YT - Yukon-Tanana terrane(s)
PE - Peninsular terrane
WR - Wrangellia terrane
AX - Alexander terrane
u - undifferentiated terranes
CG - Chugach terrane
PW - Prince William terrane
GR - Ghost Rocks Formation
YA - Yakutat terrane
Czu - Upper Cenozoic accreted rocks
0 50 100 200 MILES
0 50 100 200 KILOMETERS

Figure 0.2 Simplified tectonic map of southern Alaska showing major tectonic elements. From Lepain et al. (2013). Modified from Winkler (2000). Inset cross-section modified from Fisher and Magoon (1978). Key to abbreviations not defined on map: AARB = Aleutian- Alaska Range Batholith; AI = Afognak Island; AV = Augustine Volcano; BI = Baranof Island; BL = Becharof Lake; CD = Cape Douglas; CRB = Copper River Basin; HB = Hallo Bay; KB = Kamishak Bay; KI = Kodiak Island; KIS = Kalgin Island; IP = Iniskin Peninsula; LC = Lake Clark; IL = Iliamna Lake; KL = Kenai Lowland; PB = Puale Bay; TB = Tuxedni Bay; SB = Seldovia Bay; SA = Seldovia arch; SS = Shelikof Strait; SEM = St. Elias Mountains.

Two of these major unconformities separate the Jurassic – Cretaceous boundary and the Cretaceous – Cenozoic boundary (Nokleberg et al., 1994). This study focuses on the lower Cook Inlet as defined by Lepain et al. (2013).

Two distinct intervals of sedimentary rocks, separated by a significant regional unconformity, fill the Cook Inlet basin (see figure 1.2, Chapter One). The first is a 35,000-foot-thick Mesozoic section composed of primarily marine to deep marine siltstones, sandstones, and shales (Detterman and Hartsock, 1966; Kirschner and Lyon, 1973). These rocks record sedimentation adjacent to an emergent island arc and are composed primarily of volcanogenic and plutonic detritus shed during the subaerial exposure of the arc and its roots (Detterman and Hartsock, 1966; Lepain et al., 2013). The second succession of sedimentary rocks is the 25,000-foot-thick Cenozoic section composed almost entirely of non-marine sandstones, conglomerates, siltstones, and minor coal (Kirschner and Lyon, 1973). These rocks represent resumed subsidence and a switch from almost entirely marine sedimentation in the Mesozoic to almost entirely non-marine sedimentation in the Cenozoic. In the study area, a thin Late Cretaceous unit uncomformably overlies the Jurassic section and is overlain by the Cenozoic section. This suggests that the basin could have experienced significant exhumation during the Cretaceous.

Driven by subduction, the Aleutian/ Talkeetna arc on the northwestern flank of the Cook Inlet has been sporadically active since Mesozoic time, with hiatuses in the latest Jurassic to mid Cretaceous and again in early Paleocene (Plafker et al., 1989; Plafker and Berg, 1994; Nokleberg et al., 1994; Trop and Ridgway, 2007). Possible mechanisms for these hiatuses are (1) a gradual flattening of the down-going slab during latest Jurassic–Early Cretaceous subduction (Plafker et al., 1989; Ridgway et al., 2002; Trop et al., 2002), (2) possible ridge subduction in Cretaceous time (Pavlis and Roeske, 2007), or (3) ridge subduction in Late Paleocene time (e.g., Bradley et al., 2000).

During this period of continuous subduction, a massive subaerially exposed accretionary prism was growing and eventually defining the southern margin of the Cook Inlet basin. This accretionary prism is composed primarily of Cretaceous mélange and flysch deposits, with minor amounts of Triassic (?) to Jurassic (?) greenschist and blueschist (Plafker et al., 1994).

There is significant geologic evidence that the present-day configuration of the Cook Inlet forearc basin is the result of several well-recorded and inferred tectonic events modifying the southern Alaska margin. These possible events are 1) the collision of Wrangellia with the North American continental margin spanning Jurassic to Cretaceous time (Trop and Ridgway, 2007; Hampton et al., 2007; Hults et al., 2013);

2) the migration and subduction of a spreading ridge during Paleocene–Eocene time (Bradley et al., 2003; Haeussler et al., 2003); 3) changes in Pacific plate convergence trajectory in Eocene time (Engebretson et al., 1985; Lonsdale, 1988; Haeussler et al., 2003; Doubrovine and Tarduno, 2008); and 4) collision of the Yakutat microplate during Oligocene time (Plafker, 1987; Ridgway et al., 1986; Eberhart-Phillips et al., 2006; Fuis et al., 2008). Of these four events, two represent significant addition of continental crustal material to the margin of southern Alaska: the Mesozoic docking of Wrangellia and the Cenozoic subduction and collision of the Yakutat plate.

Mesozoic

The Wrangellia composite terrane is composed of three allochthonous terranes: the Wrangellia, Peninsular, and Alexander terranes (Plafker and Berg, 1994; Nokleberg et al., 2001). The Wrangellia Terrane is Cambrian metasedimentary schist and Permian to Tertiary volcanics and volcanogenic sedimentary rocks (Nokleberg et al., 1994). The Alexander Terrane is composed primarily of Paleozoic metamorphic rocks, Permian and Jurassic plutonic rocks, and Tertiary volcanics (Nokleberg et al., 1994). The Peninsular Terrane consists of unnamed Paleozoic (?) metamorphic rocks, Late Triassic (?) limestone and basalt, the Early Jurassic Talkeetna Arc, the Middle Jurassic Alaska-Aleutian range batholith, and finally the Mesozoic sedimentary rocks of the Cook Inlet forearc (Plafker et al., 1989; Plafker et al., 1994; Nokleberg et al., 1994).

The Alexander and Wrangellia terranes were combined by Pennsylvanian time, as shown from pluton stitching (Gardner et al., 1988) and from sedimentary overlaps (Plafker and Berg, 1994). Paleomagnetic declinations indicate they were 20–30° south of the current latitude at that time (Plafker et al., 1989). The Talkeetna arc was either built upon the combined Wrangellia and Alexander terranes, or was accreted to the margin of that composite terrane during Jurassic time (Nokleberg et al., 2001; Trop et al., 2005; Rioux et al., 2006; Clift et al., 2005a; 2005b). The Wrangellia composite terrane then collided with the North American margin during latest Jurassic–Early Cretaceous time (Trop and Ridgway, 2007). Suturing of the Wrangellia composite terrane was complete by latest Cretaceous (80–60 Ma), as shown by late Cretaceous dated intrusive plutons that stitch the accreted terranes with the former continental margin (Plafker et al., 1989; Moll-Stalcup, 1994, Trop and Ridgway, 2007). Since at least Eocene time, all terranes in southern Alaska have been subject to the deformation associated with Pacific margin subduction (Plafker et al., 1989; Plafker et al., 1994).

Cenozoic

The majority of growth and deformation of southern Alaska during Cenozoic time was likely the result of the Paleocene collision and subduction of a spreading ridge (Moore et al., 1983; Bradley et al., 2003; Haeussler et al., 2003) and the arrival and ongoing collision of the Yakutat terrane (e.g., Plafker, 1987; Eberhart-Phillips et al., 2006; Fuis et al., 2008; Ridgway et al., 1986; Benowitz et al., 2014). The authors of this thesis prefer the Kula – Resurrection model for ridge subduction (e.g., Haeussler et al., 2003) to the Kula – Farallon ridge subduction model (Byrne, 1979; Hudson et al., 1979), and as such refer to the possible ridge subduction event in Paleocene – Eocene time as the Kula – Resurrection ridge. We can neither confirm nor deny either hypothesis, and acknowledge that both are possible. During Eocene time, it's possible that the subduction of the actively spreading Kula – Resurrection spreading ridge led to uplift and deformation of the Mesozoic sedimentary strata in the upper crust (Cloos, 1993; Corrigan et al., 1990). This event *could* have spawned significant deformation of the Mesozoic strata of the Cook Inlet (Lepain et al., 2013). The arrival of the Yakutat block at the southern Alaska margin likely occurred ca. 25 Ma (Plafker, 1987), although some suggest it occurred as late as 19 Ma (Ridgway et al., 1986) and others as early as 40 Ma (Finzel et al., 2016).

Within the Cook Inlet, deformation related to the arrival of the Yakutat block is manifest in a series of offshore transpressional fault-cored anticlines and significant uplift and exposure of Cenozoic and Mesozoic forearc sedimentary rocks (Haeussler et al., 2000; Bruhn and Haeussler, 2006; Trop and Ridgway, 2007). Further inland in Alaska, the collision of Yakutat is resulting in modern seismicity on the Denali Fault, and renewed uplift of the Alaska Range (Benowitz et al., 2014).

Cook Inlet Study Area

Iniskin Peninsula and Southeastern Lake Clark National Park

The Iniskin Peninsula and Lake Clark National Park, within the lower upper Cook Inlet, contain Early Jurassic to latest Jurassic strata deformed into an anticline–syncline pair (Fitz Creek anticline and Tonnie syncline) bounded on the northwestern side by the NE-striking, westward-dipping Bruin Bay fault system. 35,000 feet of Mesozoic clastic sedimentary rocks in this NE-trending basin record forearc subsidence and sedimentation at a convergent margin since the early Jurassic, and contain the oil source rocks for the petroliferous upper Cook Inlet petroleum system (e.g., Kirschner and Lyon, 1973; Magoon and Anders, 1990; Nokleberg et al., 1994; Magoon, 1994; Trop and Ridgway, 2007; Lillis and Stanley, 2011). These immature arkosic, lithic, and volcanoclastic arc-derived sandstones, siltstones, and shales

represent exhumation of the Mesozoic arc located to the northwest of the basin (e.g., Plafker et al., 1989; Nokleberg et al., 1994; Trop and Ridgway, 2007).

Conventional reservoir potential in these rocks is poor; their primary porosity has been greatly reduced through diagenetic alteration (Helmold et al., 2013). However, these rocks are pervasively fractured and oil seeps that occur along faults and fractures were first drilled on the Iniskin Peninsula from 1900–1906. The last well drilled on the Iniskin Peninsula was in 1959 and economical production was never realized (Blasko, 1976). One well offshore has successfully exploited a fractured Jurassic reservoir in the upper Cook Inlet. This fractured Jurassic reservoir has produced 180,000 barrels of oil (Lepain et al., 2013, and references therein). Understanding complex fracture orientation relationships can allow for placement of well bores that more effectively exploit fracture networks (e.g., Engelder et al., 2009), and could therefore bring economic potential to these low-porosity reservoirs.

Detterman and Hartsock (1966) compiled mapping done in the 1940's and 1950's on the western margins of the Iniskin Tuxedni region (figure 1.1) and laid the framework for modern structural interpretations in the area. They ascribed multiple phases of regional deformation to the westward-dipping Bruin Bay Fault system and regional folds. They mapped 20 km of sinistral slip, with up to 3,000 meters of thrust on the Bruin Bay Fault system. Additionally, they mapped two principal joint sets, one striking 305˚ and the other striking roughly orthogonal at 225˚, and associated these fractures with folds in the region.

Using sedimentological constraints, others have proposed that active arc uplift and slip on the Bruin Bay Fault began in the middle Jurassic (e.g., Wartes et al., 2013; Trop and Ridgway, 2007). They interpret that coarse-grained arkosic lithologies and tilted contacts of the Mesozoic stratigraphy adjacent to the trace of the Bruin Bay Fault resulted from Jurassic uplift and exhumation of the arc in the hanging wall of the fault.

Recent studies have identified a complex deformational history along the Bruin Bay Fault, with evidence of dextral, sinistral, and thrust fault kinematics (e.g., Gillis et al., 2011; Gillis et al., 2013a; Gillis et al., 2013b; Betka and Gillis, 2014a; Betka and Gillis, 2014b). Betka and Gillis (2014a) determined two major shortening events in their kinematic analysis of the region: a principal SSE–NNW shortening direction and a subsidiary E–W shortening. Based on the sparsely populated paleomagnetic data of Coe and others (1985), and modern convergence directions (Ruppert, 2008; Fletcher and Freymueller, 2003),

they suggested that the deformation may result from Kula-Resurrection ridge subduction and clockwise oroclinal bending of southern Alaska during the Paleogene.

1. Fracture Development of the Lower Cook Inlet Alaska with Implications for Southern Alaska Tectonics

Introduction[1]

In Alaska's Cook Inlet forearc basin (figure 1.1), fractures control the locations of oil shows and seeps, and the migration of hydrocarbons (Detterman and Hartsock, 1966; Lepain et al., 2013; AOGCC, 2015). In the Cook Inlet, hydrocarbon traps are typically fault cored anticlines (e.g., Kirschner and Lyon, 1973; Bruhn and Haeussler, 2006) where fractures presumably aid in the migration of hydrocarbons from lower Jurassic marine strata into Cenozoic non-marine deposits.

Consequently, an understanding of the distribution and orientation of several well-developed fracture sets with respect to folds in the Cook Inlet, is necessary to improving the scientific community's and petroleum industry's knowledge of one of Alaska's largest petroleum provinces. Despite the important role fractures likely play in the Cook Inlet petroleum system, no detailed fracture study has been published. Early mapping campaigns on the Iniskin Peninsula cite the presence of two master joint sets (Detterman and Hartstock, 1966). However, only limited work has been done to understand the role of these fractures in a tectonic context (Detterman and Hartsock, 1966; Gillis et al., 2013a; Gillis et al., 2013b; Rosenthal et al., 2015a; 2015b; 2016).

Fractures open in the direction of minimum compressive stress at the time of deformation, and thus their orientations can be used to interpret stress orientations at the time of failure (e.g., Engelder and Geiser, 1980; Hancock, 1985; Engelder, 1987). In addition, relative ages of fractures can be determined through crosscutting and abutting relationships. The mechanical discontinuity that a fracture creates should inhibit subsequent fracture propagation, causing younger fractures to terminate in unambiguous intersections with older fractures, unless a fracture is cemented, in which case a younger fracture will crosscut an older fracture (Hancock, 1985). Thus, one can interpret the evolving deformation pattern by measuring the orientations and abutting/crosscutting relationships between multiple fracture sets (e.g., Berbauer and Pollard, 2004; Ahmadhadi et al., 2008; Yonkee and Weil, 2010a; Pastor-Galán et al., 2011; Lacombe et al., 2011). If fracture sets are regional, they can be used to estimate regional stress states (Engelder and Geiser, 1980; Engelder et al., 2009; Lacombe et al., 2011; Branellec et al., 2015).

[1] This Chapter will be revised and reformatted for submission with co-authors E. Nadin, P. Betka, R. Gillis, and J. Benowitz to Geosphere. The work presented in this chapter is the sole work of the author of this thesis.

Therefore, I use fracture orientations to define sets, and then define a relative timing of fracture development that coincides with documented tectonic events.

Summary

In this study I present field- and remote sensing- based observations of the orientations, distributions, and relative ages of several regionally prominent fracture sets. Field observations focus on the Iniskin Peninsula area of the western Cook Inlet (outlined in red in figure 1.1). Remote sensing observations expand the study to an area to the north and south along strike of the western Cook Inlet (dashed outline in figure 1.1). This study focuses on the sedimentary sequence that spans early Jurassic – Oligo-Miocene (Late Oligocene (?) to Early Late Micocene; Wolfe et al., 1966; Wolfe, 1969) time of the Cook Inlet forearc basin. I establish the sequential fracture development of the region in an attempt to unravel where, how, and in what order the regionally present fractures have formed. The results of the analyses are synthesized in a conceptual model for the tectonic development of the region in which most fractures formed early during the onset of deformation and were subsequently tilted and rotated locally during an episode of progressive deformation. The data presented in this study have broader implications about the effects of Eocene ridge subduction, and the Oligocene collision of the Yakutat terrane with southern Alaska.

Background

General Geology

The Cook Inlet basin (CIB) is a northeast-trending collisional forearc basin located in southern Alaska (e.g., Nokleberg et al., 1994; Plafker et al., 1994). The CIB is bound by the Jurassic Talkeetna Arc (a volcanic island arc sutured to the southern Alaska margin) and modern Aleutian Arc to the northwest, and the Border Ranges Fault to the southeast. The Border Ranges Fault separates the CIB from the Mesozoic – Cenozoic accretionary prism (Chugach-Prince William terranes) and Aleutian trench (the modern subduction zone) to the southeast (figure 1.1). These elements record Mesozoic and Cenozoic subduction and terrane accretion on the southern Alaska margin (Nokleberg et al., 1994). Sixty thousand feet of Mesozoic through Early Cenozoic sedimentary rock fill the Cook Inlet basin, recording ca. 200 million years of tectonic activity on the southern Alaska margin (Kirschner and Lyon, 1973). Sedimentary rocks of the Cook Inlet forearc basin span the Mesozoic – Cenozoic. Thus, the depositional and erosional patterns of these rocks should reflect tectonic events that the region experienced during Mesozoic –

Cenozoic time. The tectonic events most likely to be reflected in the sedimentary record are: 1) the docking of the Wrangellia composite terrane (Trop et al., 2005; Trop and Ridgway, 2007);

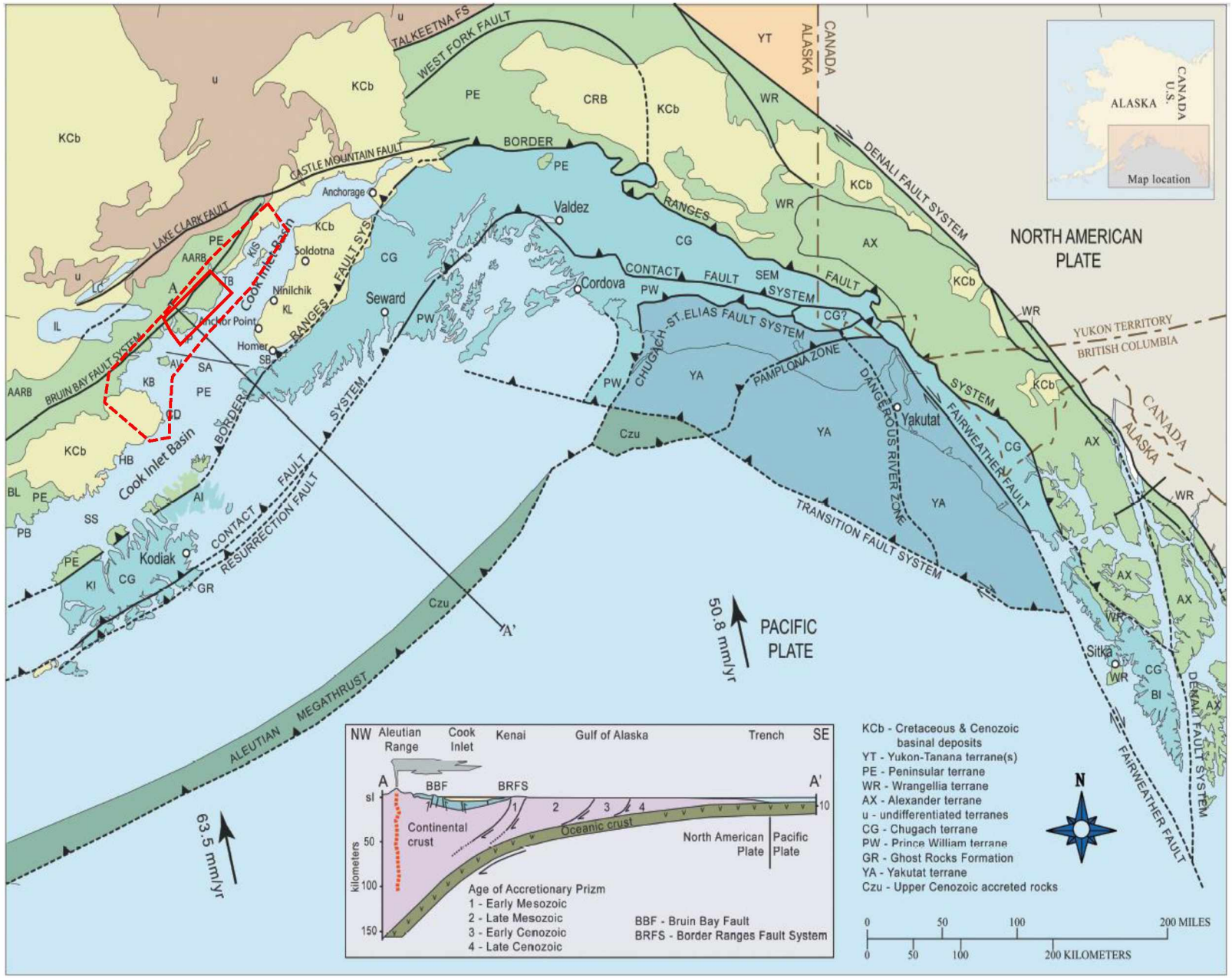
TALKEETNA FS
WEST FORK FAULT
CASTLE MOUNTAIN FAULT
LAKE CLARK FAULT
BRUIN BAY FAULT SYSTEM
BORDER RANGES FAULT SYSTEM
CONTACT FAULT SYSTEM
CHUGACH-ST ELIAS FAULT SYSTEM
PAMPLONA ZONE
DANGEROUS RIVER ZONE
FAIRWEATHER FAULT SYSTEM
TRANSITION FAULT SYSTEM
DENALI FAULT SYSTEM
RESURRECTION FAULT
ALEUTIAN MEGATHRUST
Cook Inlet Basin
Anchorage
Valdez
Cordova
Seward
Soldotna
Kenai
Homer
Anchor Point
Ninilchik
Kodiak
Yakutat
Sitka
NORTH AMERICAN PLATE
PACIFIC PLATE
50.8 mm/yr
63.5 mm/yr
YUKON TERRITORY
BRITISH COLUMBIA
CANADA
ALASKA
Map location
KCb - Cretaceous & Cenozoic basinal deposits
YT - Yukon-Tanana terrane(s)
PE - Peninsular terrane
WR - Wrangellia terrane
AX - Alexander terrane
u - undifferentiated terranes
CG - Chugach terrane
PW - Prince William terrane
GR - Ghost Rocks Formation
YA - Yakutat terrane
Czu - Upper Cenozoic accreted rocks
NW Aleutian Range Cook Inlet Kenai Gulf of Alaska Trench SE
A A'
BBF BRFS
Continental crust
Oceanic crust
North American Plate
Pacific Plate
kilometers
Age of Accretionary Prizm
1 - Early Mesozoic
2 - Late Mesozoic
3 - Early Cenozoic
4 - Late Cenozoic
BBF - Bruin Bay Fault
BRFS - Border Ranges Fault System
0 50 100 200 MILES
0 50 100 200 KILOMETERS

Figure 1.1 Outline of the study area (solid line) and remote sensing observations (dotted line) within the simplified tectonic map of southern Alaska (Modified from Lepain et al., 2013). Figure originally modified from Winkler (2000) by Lepain et al., 2013. Inset cross-section modified from Fisher and Magoon (1978). Red Box represents study area. Key to abbreviations not defined on map: AARB = Aleutian- Alaska Range Batholith; AI = Afognak Island; AV = Augustine Volcano; BI = Baranof Island; BL = Becharof Lake; CD = Cape Douglas; CRB = Copper River Basin; HB = Hallo Bay; KB = Kamishak Bay; KI = Kodiak Island; KIS = Kalgin Island; IP = Iniskin Peninsula; LC = Lake Clark; IL = Iliamna Lake; KL = Kenai Lowland; PB = Puale Bay; TB = Tuxedni Bay; SB = Seldovia Bay; SA = Seldovia arch; SS = Shelikof Strait; SEM = St. Elias Mountains

2) early Paleogene subduction of the Kula-Resurrection Ridge (Bradley et al., 2003; Haeussler et al., 2003); 3) plausible Paleocene oroclinal bending (Coe et al., 1985; Glen, 2004), 4) Miocene collision of the Yakutat microplate (Plafker, 1987; Ridgway et al., 1986; Ridgway et al., 1996; Eberhart-Phillips et al., 2006; Fuis et al., 2008), and 5) modern deformation related to Pacific plate subduction beneath North America (Plafker et al., 1989; Plafker and Berg, 1994).

While several major tectonic events have been outlined for southern Alaska, the detailed deformation patterns of the forearc strata in the southern Cook Inlet are poorly constrained (Wartes et al., 2013; Betka and Gillis, 2014a; 2014b). This study attempts to link brittle deformation with the regional tectonic events that likely deformed Cook Inlet forearc basin strata. The 35,000-foot Mesozoic section records the construction and exhumation of an oceanic island arc (figure 1.2) (Talkeetna, Tuxedni, Chinitna, and Naknek Formations). It has been proposed that the several hundred-foot-thick lower Cenozoic rocks of the West Foreland formation (that represent a small portion of the 25,000-foot-thick Cenozoic section) records the initiation of subsidence after rapid forearc basin uplift induced by the subduction of buoyant crust during the passing of the Kula – Resurrection Ridge (e.g., Bradley et al., 2003; Trop and Ridgway, 1999). The mechanisms for subsidence of the forearc for the majority of Cenozioc time are poorly understood. This study will not speculate on the mechanisms of forearc basin subsidence in the later Cenozoic when the majority of Cenozoic sediment was deposited in the Cook Inlet. Deformation of these Cenozoic rocks in the form of transpressional anticlines in the upper Cook Inlet was likely driven by the collision of the Yakutat Terrane to the southeast (Nokleberg et al., 1994; Lepain et al., 2013), though it's possible that changes in the obliquity or rate of subduction could have contributed to the creation of these Cenozoic structures (e.g., Engebretson et al., 1985; Bruhn and Hauessler, 2006).

Sedimentary Section

Jurassic

The early Jurassic Talkeetna formation, composed primarily of lava flows, volcanic breccias, agglomerates, tuffs, conglomerates, sandstones and shales represents the carapace of the SE facing Jurassic Talkeetna oceanic arc (Detterman and Hartsock, 1966; Clift et al., 2005a; Lepain et al., 2013). These rocks are commonly exposed in proximity with the Bruin Bay fault, frequently in the hanging wall, where they are often deformed.

The Tuxedni Group is composed primarily of volcanolithic shales, siltstones, sandstones, and subordinate conglomerates (Detterman and Hartsock, 1966; Lepain et al., 2013). The Tuxedni group is further divided into two unconformity-bound sequences, the upper and lower Tuxedni (Lepain et al., 2011). At the base of the Tuxedni is the Red Glacier Formation, a several hundred feet thick, deep marine, organic-rich shale that is the likely source rock for the Cook Inlet petroleum system (Magoon and Claypool, 1981; Lepain et al., 2013). Above the Red Glacier Formation are the Gaikema Sandstone, Fitz Creek Siltstone, and Cynthia Falls Sandstones that represent two transgressive–regressive cycles (Lepain et al., 2011; 2013). In the upper sections of the Tuxedni group are the Bowser and Twist Creek Siltstone Formations, which are composed primarily of fossiliferous marine sandstone and siltstone, respectively (Detterman and Hartsock, 1966; Lepain et al., 2013). These two units were deposited on top of local unconformities that incise the Cynthia Falls Sandstone across the study area (Detterman and Hartsock, 1966; Lepain et al., 2011). Altogether, the lower to middle Jurassic sedimentary rocks of the Tuxedni Group record the uplift, exhumation, and erosion of the Talkeetna arc carapace (Detterman and Hartsock, 1966; Plafker et al., 1989; Trop et al., 2005).

The middle Jurassic Chinitna formation is composed of two siltstone units with minor sandstone: the Tonnie Siltsone and the Paveloff Siltstone. These two units uncomformably overlie the top of the Tuxedni Group and are uncomformably overlain by the Naknek Formation (Detterman and Hartsock, 1966). They were deposited in a predominantly deep continental shelf setting and are representative of an overall deepening of the forearc (Lepain et al., 2013).

The overlying upper Jurassic Naknek Formation is a thick unit representing the exhumation and unroofing of the Jurassic Talkeetna arc plutonic roots after the arc carapace had been largely eroded (Detterman and Hartsock, 1966; Trop et al., 2005; Wartes et al., 2013; Herriot et al., 2016). The basal member, the Chisik conglomerate, is primarily conglomerate and coarse sandstone with dioritic and granodioritic clasts, and it fills incisions in the underlying Chinitna Formation (Detterman and Hartsock, 1966; Wartes et al., 2011). The overlying Snug Harbor siltstone is primarily composed of thin-bedded, fossiliferous, fine- to very fine-grained, interbedded sandstone and siltstone (Wartes et al., 2013). This unit represents a transgressive succession and subsidence of the forearc in Late Jurassic time (Detterman and Hartsock, 1966; Wartes et al., 2013). The top member of the Naknek is the Pomeroy Arkose member, a thick dominantly arkosic sandstone with minor conglomerate and siltstone (Detterman and Hartsock, 1966; Wartes et al., 2013; Wartes and Herriott, 2014). This unit likely represents basin floor and slope deposits (Lepain et al., 2013; Wartes et al., 2013).

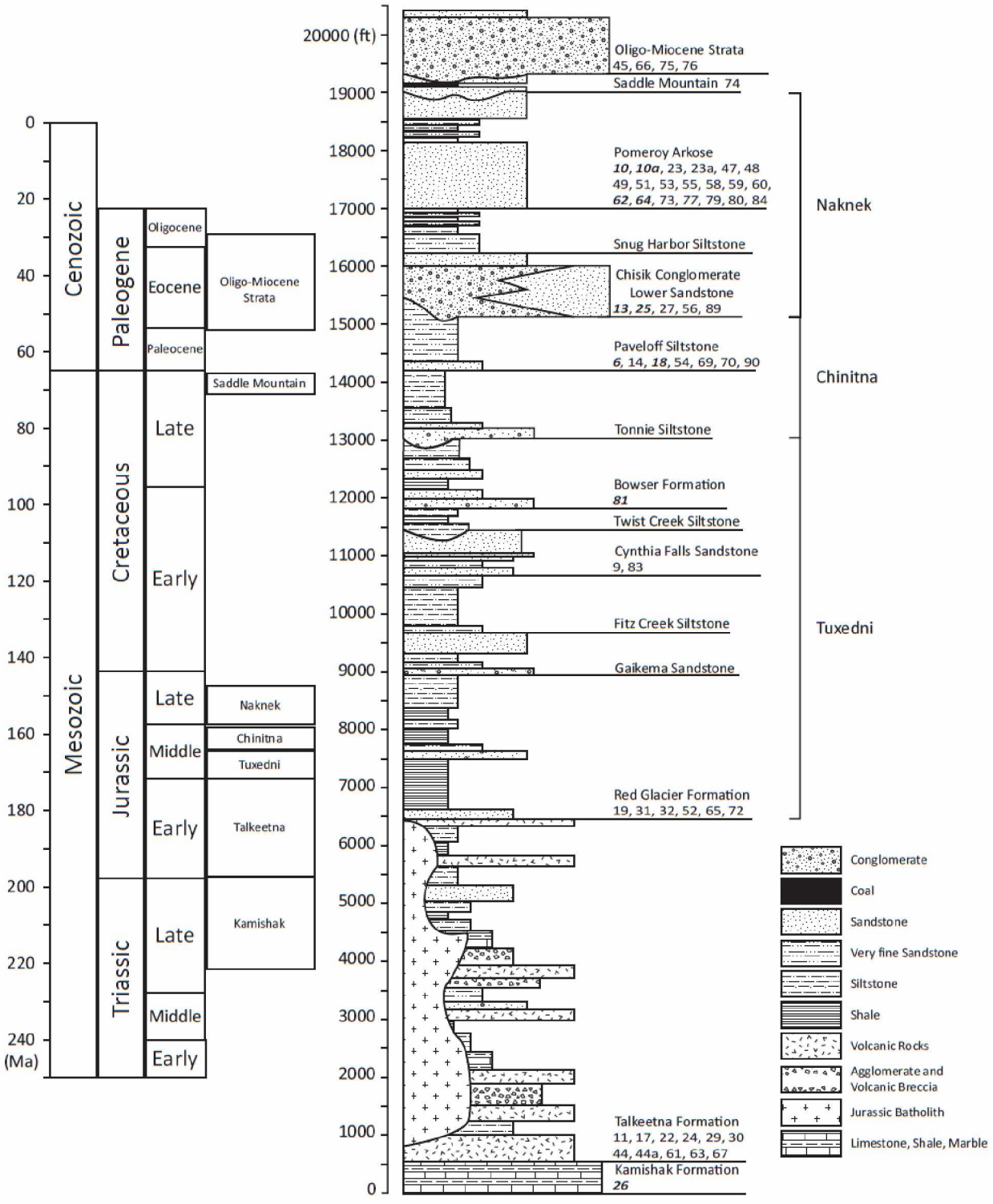
0
20
40
60
80
100
120
140
160
180
200
220
240
(Ma)
Cenozoic
Mesozoic
Paleogene
Cretaceous
Jurassic
Triassic
Oligocene
Eocene
Paleocene
Late
Early
Late
Middle
Early
Late
Middle
Early
Oligo-Miocene Strata
Saddle Mountain
Naknek
Chinitna
Tuxedni
Talkeetna
Kamishak
20000 (ft)
19000
18000
17000
16000
15000
14000
13000
12000
11000
10000
9000
8000
7000
6000
5000
4000
3000
2000
1000
0
Oligo-Miocene Strata
45, 66, 75, 76
Saddle Mountain 74
Pomeroy Arkose
10, 10a, 23, 23a, 47, 48
49, 51, 53, 55, 58, 59, 60,
62, 64, 73, 77, 79, 80, 84
Snug Harbor Siltstone
Chisik Conglomerate
Lower Sandstone
13, 25, 27, 56, 89
Paveloff Siltstone
6, 14, 18, 54, 69, 70, 90
Tonnie Siltstone
Bowser Formation
81
Twist Creek Siltstone
Cynthia Falls Sandstone
9, 83
Fitz Creek Siltstone
Gaikema Sandstone
Red Glacier Formation
19, 31, 32, 52, 65, 72
Talkeetna Formation
11, 17, 22, 24, 29, 30
44, 44a, 61, 63, 67
Kamishak Formation
26
Naknek
Chinitna
Tuxedni
Conglomerate
Coal
Sandstone
Very fine Sandstone
Siltstone
Shale
Volcanic Rocks
Agglomerate and Volcanic Breccia
Jurassic Batholith
Limestone, Shale, Marble

Figure 1.2 Simplified Stratigraphic Column of the Lower Cook Inlet
Stratigraphic thicknesses after Detterman and Hartsock (1966). Formations are drawn with typical lithologic packages and stratigraphic stacking patterns after Detterman and Hartsock (1966) and Lepain et al. (2013). Numbers beneath formation names represent station numbers for sites visited in each formation in the field.

Cretaceous

The latest Cretaceous Saddle Mountain succession unconformably overlies the Naknek formation in three observed localities in the study area (Magoon et al., 1980; Gillis et al., 2016). This formation is composed of fluvial sandstones, conglomerates and some minor coal, and represents renewed erosion of the arc batholith (Magoon et al., 1978; Magoon et al., 1980). These non-marine rocks furthermore represent a shoaling of the Cook Inlet forearc, transitioning from a predominantly marine setting in the Jurassic to predominantly non-marine from the latest Cretaceous onward. This unit has been dated through palynology on abundant sporomorphs, confining the age of the unit to the Maastrichtian stage (Magoon et al., 1980). Previous workers have suggested the unconformity separating the Maastrichtian and Late Jurassic strata in this region was angular, with a discordance of roughly 14° (Magoon et al., 1980). This would suggest that significant pre-Maastrichtian deformation tilted older Jurassic strata differentially, prior to deposition of the Saddle Mountain succession. However, recent work by Gillis and others (2016) suggests that these units were tilted uniformly locally. The mechanism for the uplift and unconformity between Late Jurassic and Late Cretaceous is unclear. Lepain et al. (2013) suggest that uplift was likely caused by collision of the Wrangellia Composite Terrane with the southern Alaska Margin. It is possible that as subduction along the northern margin of the Kahiltna basin gradually ceased, plate motion was accommodated by one subduction zone to the SE (Trop and Ridgway, 2007). As the suturing of the Wrangellia Terrane to the North American Margin continued, and plate motion was accommodated by one subduction zone, it is possible that the forearc experienced significant uplift without necessarily folding or deforming the Jurassic stratigraphic section. This would potentially create the significant unconformity between Maastrichtian and Late Jurassic strata.

Cenozoic

The Eocene (?) to Oligo-Miocene (?) strata that has been mapped on the western shores of the lower Cook Inlet is predominantly a coarse conglomerate with subordinate sandstone that unconformably overlies the Pomeroy Member of the Naknek formation (or the Saddle Mountain succession where it is present). The age constraints for the unit are poor in the study area, but elsewhere in the upper Cook Inlet, the potentially correlative lower West Foreland has been dated as Eocene with ages spanning ~47.9 – ~38.7 Ma (Gillis et al., 2016; Finzel et al., 2016). Based on plant fossil constraints, it is possible the formations mapped as West Foreland in the lower portion of the Cook Inlet in our study area are as young as Oligo-Miocene (Wolfe et al., 1966; Kirschner and Lyon, 1973). This Oligo-Miocene aged lower Cenozoic strata would be significantly younger than the Eocene aged West Foreland of the upper Cook

Inlet. Thus, it's possible that the lower Cenozoic rocks mapped as West Foreland formation were mapped incorrectly and represent a different stratigraphic unit (e.g., Triplehorn et al., 1984; Gillis, 2016, Personal Correspondence). The lower Cenozoic rocks in the lower Cook Inlet have only been dated using the one plant macrofossil, and thus the Oligo-Miocene age by Wolfe et al. (1966) represents the only age for the sampled rocks in the area. In addition to having a different age, these units are missing some of the characteristic interlayered tuffs of the West Foreland in the upper Cook Inlet (Calderwood and Fackler, 1972). Thus, because of the uncertainty in the age, and formation call, we will refer to the formation mapped as West Foreland as Lower Cenozoic or Oligo-Miocene strata for the remainder of the paper. The implications for age changes of this unit are discussed in the discussion section of this paper.

Major Study Area Structures

Detterman and Hartsock (1966) compiled mapping done in the1940's and 1950's on the western margins of the Iniskin Tuxedni region (figure 1.1) thereby laying the framework for modern structural interpretations in the area. Early to Latest Jurassic strata are deformed, forming an anticline–syncline pair (Fitz Creek anticline and Tonnie syncline) on the Iniskin Peninsula. North of the Iniskin Peninsula Early Jurassic to lower Cenozoic/Oligo-Miocene strata are tilted toward the southeast. The Bruin Bay fault bounds the Cook Inlet Basin (CIB) to the northwest, including the study area. Along much of its length, this fault separates the Jurassic aged plutonic roots of the Talkeetna Arc and portions of the Jurassic Talkeetna Arc carapace from the immature arkosic, lithic, and volcanoclastic arc-derived sandstones, siltstones, and shales of the Cook Inlet forearc basin (Detterman and Hartsock, 1966; Detterman and Reed, 1980; Gillis et al., 2013a; 2013b). In the northern reaches of the study area the fault displaces Talkeetna plutonic roots against Talkeetna plutonic roots (Detterman and Hartsock, 1966).

Detterman and Hartsock (1966) interpret multiple deformation events spanning Jurassic-Cenozoic time on the basis of regional and local unconformities (figure 1.2). On the Bruin Bay Fault, Detterman and Hartsock (1966) mapped 20km of sinistral slip based on displaced tracts of Talkeetna Formation and interpret up to 3,000 meters of stratigraphic throw. However, the poorly understood piercing points used for these interpretations are unclear, and the significance ambiguous (Betka and Gillis, 2014a). Additionally, they interpret two fault related principal joint sets, one striking 305˚ and the other striking roughly orthogonally at 225˚.

Using sedimentological constraints additional workers maintain that deformation along the Bruin Bay fault began in the middle Jurassic (e.g., Detterman and Hartsock, 1966; Trop et al., 2005; Trop and Ridgway, 2007; Wartes et al., 2013). They interpret that coarse-grained lithologies, tilted Mesozoic stratigraphy, and angular unconformities within the Mesozoic stratigraphic section result from Jurassic uplift and exhumation of the Talkeetna Arc in the hanging wall of the Bruin Bay Fault. This uplift might have resulted from the collision of either the Peninsular Terrane with the combined Wrangellia and Alexander Terranes, or the Wrangellia Composite Terrane with North America (Trop et al., 2005). Using apatite and zircon fission-track analyses Gillis et al. (2008) interpret a second possible event in the Paleogene. Younger activity on the Bruin Bay fault, and deformation within the study area could have resulted from the subduction of the Kula – Resurrection spreading ridge during Eocene time (Lepain et al., 2013; Gillis et al., 2008; this study) and potentially the arrival of Yakutat during Oligocene time (this study).

Recent studies have identified a complex, polyphase, deformational history along the Bruin Bay Fault, with evidence of dextral, sinistral, and thrust faulting (e.g., Gillis et al., 2013a; 2013b; Betka and Gillis, 2014a; 2014b; 2015; 2016). Two major shortening events include a principal SSE–NNW shortening event and a subsidiary E–W shortening event with unknown relative ages (Betka and Gillis, 2014a; 2014b). Betka and Gillis (2015) speculate that the E-W shortening event could represent suturing of the Wrangellia Composite Terrane to North America and the southeast shortening event likely records Eocene deformation during subduction of the Kula-Resurrection spreading ridge.

Methods

Introduction to Methods

This study focuses on the relative timing of fracturing and folding in the Iniskin Tuxedni region. I restore fracture orientations by unfolding bedding to establish relative ages of fractures and folding (Hancock, 1985). Following Yonkee and Weil (2010a) I use a strike test to evaluate the potential kinematic relationship between fracturing and folding in the study area. I establish relative chronologies of fractures by using abutting and cross cutting field relationships after Branellec et al. (2015). I constrain the absolute timing of fracture formation by using an $^{40}Ar/^{39}Ar$ age from an igneous dike in the field area that is cut by fractures.

In order to understand the relationship of fractures with regional deformation, I mapped fracture orientations, fracture type, and relative fracture ages encompassing all potential structural domains across the study area (e.g., Ahmadhadi et al., 2008; Pastor-Galán et al., 2011; Branellec et al., 2015). It was necessary for me to measure fractures in areas where the rocks are folded and faulted to determine any effect of local structures on fracture formation (Bergbauer and Pollard, 2004; Ahmadhadi et al., 2008). Furthermore, to evaluate regional presence of fracture sets, I initiated a wide spread analysis of fracture character using satellite imagery (e.g., Mobasher and Babaie, 2008). The spatial variation of fracture sets, and their apparent relationships with local structures were used to evaluate the relative timing between fracturing, folding, and tilting (e.g., Bergbauer and Pollard, 2004; Ahmadhadi et al., 2008; Engelder et al., 2009; Lacombe et al., 2011; Branellec et al., 2015). The regional presence of a fracture set allows us to discriminate if there are structure-specific fracture sets that may be related to local folds and faults (e.g., Mobasher and Babaie, 2008; Ahmadhadi et al., 2008). Fracture abutting relationships were assessed and used to constrain the relative timing of fracture set formation (e.g., Kulander et al., 1979; Hancock, 1985; Pollard and Aydin, 1988; Aydin and Degraff, 1988; Rives et al., 1994). I used a strike test to correlate the dispersion of fracture set strikes with bedding strikes and test for local vertical axis-rotation of the fracture sets during folding (e.g., Yonkee and Weil, 2010a; 2010b).

Orientation Data

A minimum of 20 fracture strike and dip measurements were made at each station to establish general outcrop fracture character (Engelder and Geiser, 1980). I measured the strike and dip of bedding multiple times at each station and averaged those numbers. Once I determined bedding orientation, I rotated the fracture data on a station-by-station basis around a horizontal axis parallel to the strike of

bedding. Restoring bedding to zero helped me evaluate if the observed fracture sets developed pre-folding or tilting (Hancock, 1985). Resistant beds were measured most often, as they were the most likely to preserve fracture character; however, the sampling strategy reflects efforts to also measure fractures in less weather-resistant formations to eliminate bias. I plotted the measurements for each site on a Schmidt lower hemisphere stereographic projection in Stereonet© (Allmendinger et al., 2013; Cardozo and Almendinger, 2013). I identified clearly formed fracture sets at most sites. Fracture sets form well-defined clusters on pole to plane stereographic projections (figure 1.3). Errant fractures that fell outside of the well-defined sets were ignored because they likely resulted from small local variations in stress or from unloading. To determine the relative timing of intersecting fractures I recorded abutting relationships by noting the number of times a specific set either abutted, or cross-cut an adjacent set along scan-lines placed parallel to each set in several locations.

Strike Test

In this study, I perform a strike test to constrain the relative ages between fractures and folds in the Iniskin – Tuxedni Region. Strike tests are typically used to estimate the changes in regional structural trend with regard to regional deformation fabrics or paleo-magnetic declinations (e.g., Schwartz and Van der Voo, 1983; Weil and Yonkee, 2012). Typically, these strike tests are used to estimate the degree of rotation of regional structures that has occurred during the formation of regional oroclines. The data collected and presented in this study are localized to a small region of the Cook Inlet. Thus, the rotations, if any, are likely to be of local significance.

When these rotations are combined with abutting relationships, fracture stratigraphy, and fractures sets throughout the study area, they help constrain the relative timing between fracturing and folding. Furthermore, because fractures and folds often form under regional stress fields, relative timing between folding and fracturing can be used to understand the sequential development of regional stress states.

I used the strike test to evaluate the correlation between the trend of regionally folded and tilted strata with local changes in fracture set strike (e.g., Yonkee and Weil, 2010a; 2010b; Pastor-Galán et al., 2011). By evaluating systematic correlations between the strike of bedding and fractures, I attempt to establish if fractures were rotated when bedding was tilted and possibly rotated during folding. To test whether fractures rotated about a local vertical axis, I apply the technique that Yonkee and Weil (2010a; 2010b) used to test for regional fracture rotations. I seek to evaluate if fracture sets developed during the formation of regionally folded and tilted strata by establishing if there is a correlation between deviation

in strike of bedding from a regional reference bedding strike and deviation in orientation of a fracture set from a reference fracture set. I rotate measured fracture sets on a station-by-station basis about a vertical axis by restoring the strike and dip of bedding at each individual station to a regional reference strike and dip of bedding. These rotations would only better constrain the relative timing of deformation, and would fail in testing for regionally consistent rotations in fracture strike as what would occur in an oroclinal setting. The fold test was applied to determine the correlation between rotation of the fracture sets and bedding during the formation of the local folds in the study area (e.g., Pastor-Galán et al., 2011); this study was not designed to test for oroclinal bending.

The strike test begins by subtracting the strike of bedding (So) at a specific station from a regional reference strike of bedding (Sr). I then subtracted the strike of a given fracture set (Fo) from the expected strike of that given fracture set (Fr). For example, if a fracture set typically strikes normal to the strike of bedding, the expected strike of this fracture set would be normal to the regional reference strike of bedding. If the fracture sets developed prior to folding I would expect to see a one-to-one correlation between strike of bedding and strike of a fracture set (for example, a 40˚ deviation in bedding strike would result in a 40˚ deviation in fracture strike). The previous example only works as an end member case assuming only one possible horizontal axis rotation during folding. If the fracture sets formed during the folding process, the relationship should be less than a one to one correlation, and greater than a zero correlation, indicating that there was prior deviation in bedding strike before the fracture set opened, but subsequent deviation in bedding strike after the fracture set opened and folding progressed. If the fractures formed after folding, the correlation should be zero, because there would be no relationship between the strike of folded strata and fracture set orientations with respect to their regional orientation. To establish a correlation between So-Sr and Fo-Fr, the weighted linear regression from Yonkee and Weil (2010a) is calculated for the data with stations with higher errors being weighed less significantly than stations with lower errors. Statistical methods of significance follow from Yonkee and Weil (2010a).

To calculate Fo I used average fracture strikes calculated at each station for each identified fracture set. Average fracture set orientations were determined from Fischer mean vectors calculated for each individual set at each outcrop (Allmendinger et al., 2013). Stations where fractures were not systematic were ignored, as local structural complexity or local small block rotations likely prevented the opening of systematic fracture sets. Fracture sets were identified on the basis of consistent orientations after first restoring bedding dip to horizontal, and then restoring bedding strike to a regional reference strike

(calculated from a pi diagram). In using this method, I make the assumption that most fractures formed early during folding, or prior to folding. Commonly there were two dominant sets at each station, a fracture set striking normal to the strike of the orogen (roughly 310°) and a fracture set sub parallel to the strike of the orogen (roughly 210°). After fracture sets were identified at each station, the individual sets were delineated, separated, and then plotted in Stereonet^{tm} where the Fischer mean vector was calculated. I determined error in the strike of fracture sets by using the 95% confidence interval from Fischer mean vectors for each fracture set. Although there is some dispersion and overlap in the total data set, the vector statistics demonstrate that the fracture sets identified are distinct and statistically significant. Furthermore, at the outcrop it is easy to distinguish fracture sets because their orientations are commonly oblique or orthogonal to one another. I realize that fracture sets identified in this method can in some instances exhibit overlap. I try to account for this overlap by using the relative orientations between fracture sets to assign identities to the specific fracture sets. The results reflect that while there is significant overlap initially in the non-dip and non-strike restored field measurements, the fractures cluster more closely together after having bedding, and strike restored to a regional reference orientation (see K-Parameter test). I also realize, that it is possible for multiple horizontal axis rotations to skew the results of the strike test (i.e. folding a fold). In this scenario, our vertical axis rotations would only restore the majority of the deformation, not recognizing a smaller component of horizontal axis rotation which could have led to some additional vertical axis rotation. I feel comfortable with our rotations as I suspect that the majority of the deformation was likely during one folding event, and any subsequent horizontal axis rotations would be of a small magnitude that have little effect on the results. There are four possible end members of the strike test: 1) Primary arc-Uniform Slip where the resulting slope of the strike test is zero suggesting there was no vertical axis rotation 2) Primary arc-Radial Slip where the resulting slope of the strike test is one as fractures formed normal to a previously curved margin 3) Progressive arc-curved slip yielding a strike test slope less than one and greater than zero and 4) Secondary orocline bending where fractures form in an uncurved orogen that is subsequently rotated during a separate deformation event yielding a strike test slope of one (see figure 1 of Yonkee and Weil, 2010a).

Bedding strike and dip were averaged from several measurements. Errors associated with bedding were determined on the basis of steeper beds having considerably less error in measurement of strike than more shallowly dipping beds. As such, errors in bedding were assigned on the steepness of bedding with shallowly dipping beds receiving a greater error and steeply dipping beds a smaller error (table 1.1).

Beds dipping 0-15° received 5° of error, 15-20° received 4° of error, 20-25° received 3° of error, and >25° received 2° of error.

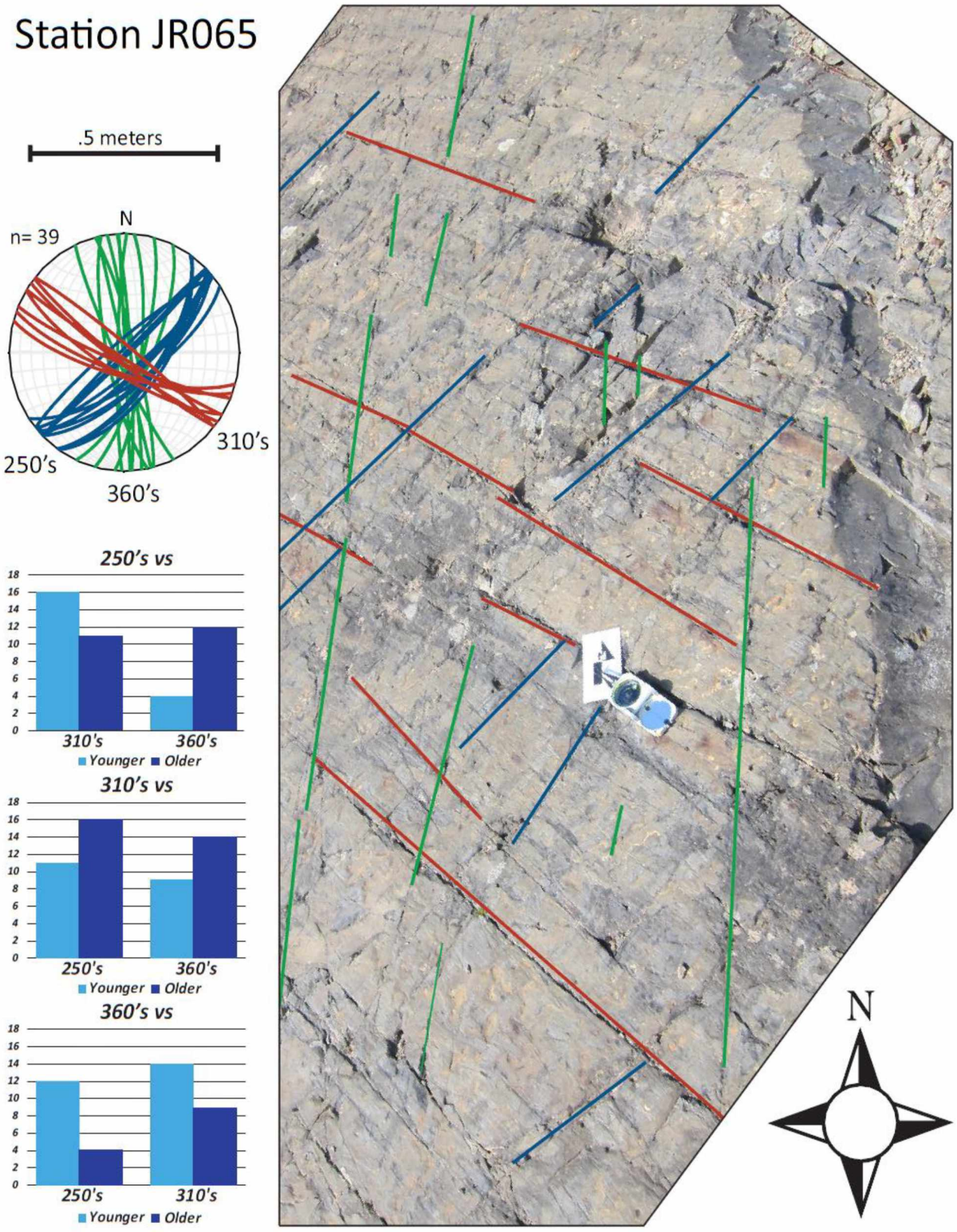

Figure 1.3 Sample Station JR065
Fracture sets are labeled and color coded. Histograms on the left represent the relative ages of the fracture sets. The bar graphs are read as follows: the title is the reference fracture set and the x-axis represents the two fracture sets being compared against the reference set. If the light blue bar is larger, than the compared fracture set is younger than the reference fracture set. If the dark blue bar is larger, the reference fracture set is younger. For example, in the 210's vs plot, the 310's are younger and the 360's are older.

Reference bedding ("strike of the orogen") was determined on the basis of kilometer scale map patterns and a pi diagram representing the poles to planes for all bedding measurements in the field. The regional fold axis from this test yields a trend and plunge of 130° and 1° respectively. Because the folds are largely cylindrical and regional plunge of the fold is minimal, I deduce that fold plunge would not make significant difference in the interpretations. While the very northern and very southern portions of the Iniskin Peninsula are likely part of plunging folds, the majority of the data was sampled from strata in the middle of the folds, in the non-plunging regions.

Fractures from Satellite Imagery

To determine the distribution and orientations of large fractures across the study area (>5m) I used satellite imagery to map fracture lineaments. I imported and mosaicked SPOT (Satellite Pour L'Observation de la Terre) 2.5-meter-resolution images using the ESRI ArcMap 10.2^{tm} Geospatial Information System (GIS). I mapped all visible lineaments as macroscopic fractures and faults. When drawing lineaments in GIS I preferentially mapped clear lineaments that cut across bedding or clearly controlled landscape development. I used a simple Python script in GIS to calculate the orientations of the traced lineaments:

*Orientation = 180+math.atan2((!Shape.firstpoint.X! - !Shape.lastpoint.X!),(!Shape.firstpoint.Y! - !Shape.lastpoint.Y!)) * (180 / math.pi)* (1)

Because fracture dip cannot be measured in aerial images, I considered only the trend of the lineaments. We make the assumption that because fractures measured in the field are commonly vertical to sub-vertical, and because fractures generally open normal to bedding surfaces (e.g., Hancock, 1985), the trend of the lineament and therefore strike of the fracture are subparallel. These data are then exported to Stereonet© where they are evaluated using rose diagrams.

Aerial images taken from helicopter flyovers were also used for outcrop analysis of fracture distributions. A continuous series of photographs was taken over outcrops of exceptional exposure by flying over the outcrop at low altitude with a Garmin VIRB^{tm}. Video stills were later cropped from the videos and mosaicked with Agisoft^{tm}. The resulting high resolution photo mosaics were then imported into ESRI ArcMap 10.2^{tm}. Using field sketches, I oriented photos towards north, and traced fracture and fault lineaments remotely. I used equation (1) to calculate the orientation of the traced lineaments.

Stations	Unit	Age	Latitude	Longitude	Bedding	310°	210°	260°	360°
JR06	Paveloff	165	59.658	-153.31	65, 20 (±3)	344, 80 (±7.3); K = 25; n = 17		264.1, 77.5 (±7.3); K = 70.6; n = 6	
JR09	Cynthia Falls	170	60.166	-152.68	20, 15 (±5)	304, 90 (±3.8); K = 104; n = 14	204.5, 81.8 (±4.1); K = 80.2; n = 16	60.4, 85 (±8.6); K = 43; n = 7	
JR10	Pomeroy	152	59.648	-153.18	47, 19 (±4)	318, 90 (±3.5); K = 43; n = 40	213, 80.6 (±9.5); K = 35.1; n = 6	253.7, 89.8 (±21.4); K = 11; n = 5	192.3, 80.1 (±5.2); K = 70.8; n = 12
JR11	Talkeetna	190	59.945	-153.03	60, 20 (±3)	341, 72 (±16.8); K = 9; n = 9			206.1, 89.7 (±6.9); K = 31.8; n = 14
JR13	Lower SS	162	59.652	-153.31	46, 20 (±3)	300.5, 82.6 (±5.1); K = 54; n = 15			
JR14	Paveloff	165	59.884	-152.99	25, 22 (±3)	297, 76 (±8.8); K = 35; n = 8	201.2, 85.2 (±4.4); K = 91.8; n = 11		
JR17	Talkeetna	190	60.154	-152.95	65, 20 (±3)	322.2, 70.4 (±6); K = 101; n = 7	228.5, 89.7 (±8.4); K = 21.8; n = 13		
JR18	Paveloff	165	59.833	-153.03	40, 20 (±3)	126.2, 81 (±4.9); K = 42; n = 21			371.7, 85.1 (±7.5); K = 27.3; n = 13
JR19	Red Glacier	175	60.026	-152.95	37, 12 (±5)	318, 80.9 (±8.6); K = 49.7; n = 7	46.9, 87.3 (±11.1); K = 20.1; n = 9		351.3, 89.4 (±25); K = 10.8; n = 4
JR22	Talkeetna	190	59.906	-153.1	60, 30 (±2)	151.4, 87.9 (±8.8); K = 25.4; n = 12	219.4, 66.9 (±4.8); K = 28.1; n = 32	92.6, 87.1 (±3.6); K = 63.8; n = 29	
JR23	Pomeroy	152	59.878	-152.92	16, 17 (±4)	304.1, 81.1 (±6.6); K = 20; n = 14		218.7, 84.2 (±14.9); K = 14.9; n = 7	158.3, 73.4 (±7.3); K = 26.8; n = 15
JR23a	Pomeroy	152	59.878	-152.92	17, 13 (±5)	285.5, 71.9 (±4.9); K = 32; n = 23		57.7, 89.4 (±7.9); K = 14.2; n = 25	171.1, 76.2 (±10.9); K = 14.2; n = 14
JR24	Talkeetna	190	60.041	-152.95	10, 13 (±5)	302.7, 64.4 (±6.3); K = 48; n = 11		240.5, 81.5 (±2.9); K = 138; n = 18	
JR25	Naknek	162	59.551	-153.59	70, 40 (±2)	156.4, 74.1 (±5.3); K = 17; n = 36	49.1, 82.9 (±12.1); K = 19.3; n = 8		
JR26	Kamishak	225	59.553	-153.62	50, 65 (±2)	148.8, 85.4 (±6.6); K = 16; n = 23			
JR27	Chisik	163	60.158	-152.57	31, 13 (±5)	130.2, 89.2 (±3.2); K = 133; n = 14		252.2, 73.2 (±7.3); K = 26.6; n = 15	
JR29	Talkeetna	190	60.139	-152.88	20, 22 (±3)	291.5, 79.2 (±12.1); K = 25.8; n = 7			173, 69.7 (±19.2); K = 13.1; n = 6
JR30	Talkeetna	190	60.136	-152.88	45, 30 (±3)	324.9, 82 (±15); K = 12.8; n = 7			
JR31	Red Glacier	175	60.135	-152.87	50, 20 (±3)	324.1, 84.4 (±9.2); K = 23.4; n = 11		256, 75 (±7.2); K = 41.5; n = 5	182.6, 88.1 (±14.5); K = 18.7; n = 5
JR32	Red Glacier	175	60.135	-152.87	45, 20 (±3)	131.7, 84.8 (±10.7); K = 17.3; n = 12	218.1, 64 (±16.5); K = 56; n = 3		
JR44a	Talkeetna	190	60.157	-152.93	50, 35 (±2)	304.7, 86.4 (±9.3); K = 28; n = 10	210.5, 82.6 (±15.3); K = 9; n = 12		
JR45	Paleogene	?	60.286	-152.42	20, 17 (±4)	125.2, 88.5 (±2.7); K = 191.1; n = 15	39.1, 76.2 (±3.8); K = 131.9; n = 11		
JR47	Pomeroy	152	60.04	-152.58	35, 17 (±4)		33.9, 89 (±7.4); K = 58; n = 7	68.4, 89.1 (±7.9); K = 18.2; n = 7	
JR48	Pomeroy	152	60.041	-152.58	20, 25 (±3)	103, 85.9 (±23.5); K = 5.7; n = 7		225.9, 70.7 (±15.5); K = 16.3; n = 5	341.5, 84.2 (±6.7); K = 105.9; n = 5
JR49	Pomeroy	152	60.042	-152.63	45, 15 (±5)	315.6, 86.2 (±4.6); K = 81.7; n = 13		246.6, 87.5 (±9.4); K = 36.2; n = 7	373.6, 90 (±7.2); K = 34; n = 11
JR51	Pomeroy	152	60.053	-152.64	20, 15 (±5)	110, 87 (±8.7); K = 36.7; n = 7	26, 85 (±6.4); K = 52.4; n = 10	71, 86.4 (±7.3); K = 59.2; n = 7	172.8, 87.4 (±6.5); K = 35.3; n = 13
JR52	Red Glacier	175	60.13	-152.85	20, 17 (±4)	283.4, 89 (±10.5); K = 6.8; n = 16	14.9, 89.2 (±9.5); K = 30.6; n = 7		
JR53	Pomeroy	152	59.981	-152.71	31, 18 (±4)	111.2, 85.7 (±24.4); K = 31.7; n = 11	202.3, 80.2 (±8); K = 157.5; n = 3	243.8, 90 (±9.1); K = 76.8; n = 2	342.5, 85.8 (±10.1); K = 16.6; n = 11
JR54	Paveloff	165	60.172	-152.58	18, 15 (±5)			260.3, 85.4 (±6.8); K = 35.2; n = 13	334.6, 84.5 (±19.6); K = 12.9; n = 5
JR55	Pomeroy	152	60.094	-152.56	30, 25 (±3)	300.9, 83.3 (±2.9); K = 243.1; n = 4	200.8, 87.9 (±3.9); K = 95.2; n =	246.8, 87.8 (±4.7); K = 45.1; n = 11	352, 86 (±6.6); K = 73.3; n = 7
JR56	Lower SS	162	59.947	-152.9	20, 20 (±3)	305.3, 65.6 (±6.9); K = 15.7; n = 15			164, 81.5 (±22.4); K = 10.1; n = 5
JR58	Pomeroy	152	59.951	-152.88	40, 25 (±3)	305.5, 89.3 (±9.4); K = 16.5; n = 8	205.8, 70.9 (±10.5); K = 19.8; n = 10	264.3, 76 (±7.3); K = 23.4; n = 9	176.7, 83.6 (±9.6); K = 21.6; n = 11
JR59	Pomeroy	152	59.951	-152.87	55, 18 (±4)	126, 80.9 (±6.9); K = 34; n = 7			377.2, 87.4 (±5.3); K = 94.9; n = 8
JR60	Pomeroy	152	59.95	-152.87	50, 25 (±3)	313.6, 81.7 (±5.5); K = 33; n = 11	202.7, 77 (±10); K = 18.1; n = 14	272.4, 82.3 (±7.4); K = 43; n = 11	
JR61	Talkeetna	190	59.975	-153.02	50, 34 (±2)	137.3, 83.8 (±9.1); K = 17.2; n = 8		279.5, 84.3 (±7.4); K = 38.7; n = 9	189.5, 87.6 (±14.7); K = 13.3; n = 8
JR62	Pomeroy	152	59.707	-153.04	45, 20 (±3)	150.8, 83.3 (±13); K = 11.1; n = 6	216.9, 74 (±12.3); K = 31.5; n = 5	272.8, 86.5 (±12.8); K = 8.8; n = 9	166.2, 89.3 (±7.5); K = 27.1; n = 14
JR63	Talkeetna	190	59.979	-153.03	35, 33 (±2)	305.5, 75.8 (±7.8); K = 14; n = 13	201.1, 88.6 (±7.4); K = 35.5; n = 11	76.8, 88.8 (±11.4); K = 17; n = 5	
JR64	Pomeroy	152	59.788	-153	17, 50 (±2)			243.6, 88.1 (±3.9); K = 42; n = 16	162.5, 88.7 (±6.8); K = 24.1; n = 20
JR65	Red Glacier	175	60.032	-152.96	24, 28 (±3)	120.1, 83.5 (±3.7); K = 58.3; n = 13		230.3, 74.9 (±7.9); K = 34.8; n = 11	170.9, 83.3 (±7.6); K = 37.2; n = 10
JR66	Paleogene	?	59.882	-152.9	27, 10 (±5)	135, 85 (±10.4); K = 15.7; n = 14	197, 77 (±15.4); K = 15.4; n = 5	260, 82 (±9.7); K = 9.2; n = 13	165, 79 (±5.2); K = 32.1; n = 25
JR67	Talkeetna	190	60.075	-152.92	15, 24 (±3)	105.9, 77 (±10.7); K = 21.2; n = 10		242.6, 45.3 (±7.4); K = 68.8; n = 6	356, 68.2 (±10.7); K = 89.4; n = 3
JR69	Paveloff	165	60.014	-152.78	37, 17 (±4)	300.8, 85 (±4.4); K = 22; n = 24			369.8, 86.1 (±9.1); K = 26.1; n = 10
JR70	Paveloff	165	60.014	-152.79	30, 20 (±3)	133.4, 88.3 (±5.3); K = 58; n = 14	215.8, 79 (±14.1); K = 19.6; n = 6		
JR72	Red Glacier	175	60.033	-152.95	55, 23 (±3)	148.7, 82.5 (±9.1); K = 28.9; n = 10	49.3, 89.8 (±7.8); K = 39.7; n = 9	280, 78 (±11.3); K = 21.9; n = 8	
JR73	Pomeroy	152	60.072	-152.65	25, 22 (±3)	299.6, 88.1 (±5); K = -; n = 4	208.9, 76.1 (±22.6); K = 20.5; n = 3	237.9, 87.3 (±7.9); K = 95.2; n = 6	167.2, 84.2 (±3.9); K = 107.3; n = 13
JR74	Saddle Mountain	72	59.945	-152.82	50, 33 (±2)	137, 79.5 (±7.3); K = 13.8; n = 30	233.5, 84.7 (±10.2); K = 26.5; n = 8		370.1, 87.5 (±7.5); K = 37.9; n = 10
JR75	Paleogene	?	59.93	-152.85	46, 23 (±3)	313, 86 (±5.8); K = 27.1; n = 24	044, 80 (±14.1); K = 12.7; n = 10	098, 86 (±13.7); K = 32.3; n = 5	178, 65 (±12.6); K = 96.5; n = 3
JR76	Paleogene	?	59.93	-152.85	37, 24 (±3)	135, 88.7 (±6.5); K = 38.3; n = 14	209.8, 85.7 (±8); K = 33.4; n = 10		
JR77	Pomeroy	152	59.64	-153.2	30, 25 (±3)	307.8, 83.4 (±5.1); K = 42.1; n = 20	217.9, 81 (±4.8); K = 102.1; n = 18		
JR79	Pomeroy	152	59.919	-152.93	34, 13 (±5)	306, 88.6 (±3.6); K = 88.3; n = 19	211.4, 81.2 (±5.7); K = 146; n = 5	65.3, 88.7 (±8.5); K = 37.4; n = 9	177.2, 83.5 (±11.3); K = 21.7; n = 8
JR80	Pomeroy	152	59.918	-152.94	46, 17 (±4)	139.7, 87.4 (±9.8); K = 18.9; n = 13	222.9, 86.3 (±5.6); K = 41.2; n = 17		
JR81	Bowser	167	59.816	-153.17	45, 64 (±2)	136.3, 84.1 (±10.6); K = 15.1; n = 14			365.1, 89.3 (±10.7); K = 12.9; n = 16
JR83	Cynthia Falls	170	60.163	-152.68	38, 12 (±5)	320.4, 79.9 (±10.8); K = 15.6; n = 13	226.9, 76.8 (±13.8); K = 9.9; n = 12		
JR84	Pomeroy	152	60.043	-152.58	32, 25 (±3)	137.8, 82.3 (±9.1); K = 20.2; n = 14		245.6, 73.3 (±7.9); K = 31; n = 11	361.5, 81.3 (±5.2); K = 52.3; n = 15
JR89	Lower SS	162	59.964	-152.87	40, 25 (±3)	299.2, 84.9 (±8.3); K = 25.7; n = 13	27, 81.3 (±4.8); K = 60.2; n = 15		
JR90	Paveloff	165	60.169	-152.58	30, 15 (±5)	129.4, 82.6 (±7.2); K = 25.7; n = 17	218.6, 82.2 (±7.6); K = 102.4; n = 5		

Table 1.1: Fracture Data for Each Station
Data for each station. Age is in millions of years and is approximated from stratigraphic ages. 95% confidence intervals shown in parentheses for bedding and fractures. K parameter, and n value for each fracture set are also presented.

K-Parameter Test

Fracture data at each station are rotated twice to restore fracture strike and dip to what would be pre folding orientations. The first rotation restores bedding to horizontal by rotating the fractures about a horizontal axis parallel to the mean strike of bedding at each station. Then, to restore the data to pre rotation strike, I rotated the data about a vertical axis to the mean strike of bedding in the study area (40°). I then identified individual fracture sets on the basis of orientation and relative orientations between fractures sets. These individually identified fracture sets were then grouped and plotted in Stereonet ^{tm} to evaluate dispersion of the data as a whole. I evaluate how much dispersion each fracture set experiences by calculating the Fischer mean vector for each fracture set at three stages, and comparing the K parameter. These three stages are (1) as measured, (2) backtilted, and (3) strike corrected. I make the assumption that if data is more neatly clustered after unfolding and strike correction, the fractures were pre or syn folding. I therefore assume that it is possible for fractures to be rotated on a local scale. If the data is more dispersed after unfolding and strike correction it is likely that the data are post folding. The stronger the decrease in dispersion (increase in the K-parameter) the earlier the fracture sets likely formed.

Geochronology

For $^{40}Ar/^{39}Ar$ analysis, one rock sample was analyzed at the Geochronology laboratory at the University of Alaska Fairbanks (UAF). It was crushed, sieved, washed and hand-picked for phenocryst free rock chips (500–1000 micron size fraction). The monitor mineral MMhb-1 (Samson and Alexander, 1987) with an age of 523.5 Ma (Renne et al., 1994) was used to monitor neutron flux and calculate the irradiation parameter, J. The samples and standards were wrapped in aluminum foil and loaded into aluminum cans of 2.5 cm diameter and 6 cm height. The sample was irradiated in position 5c of the uranium enriched research reactor at McMaster University in Hamilton, Ontario, Canada, for 20 megawatt-hours.

Upon its return from the reactor, the sample and monitors were loaded into 2 mm diameter holes in a copper tray that was then loaded in an ultra-high vacuum extraction line. The monitors were fused, and sample heated, using a 6-watt argon-ion laser following the technique described in York et al. (1981), Layer et al. (1987) and Benowitz et al., (2014). Argon purification was achieved using a liquid nitrogen cold trap and a SAES Zr-Al getter at 400 ˚C. The sample was analyzed in a VG-3600 mass spectrometer at UAF. The Ar isotopes measured were corrected for system blank and mass discrimination, as well as calcium, potassium and chlorine interference reactions, following procedures outlined in McDougall and

Harrison (1999). Typical full-system 8 min laser blank values (in moles) were generally 2×10^{-16} mol ^{40}Ar, 3 × 10218 mol ^{39}Ar, 9 × 10-18 mol ^{38}Ar and 2×10^{-18} mol ^{36}Ar, which are 10–50 times smaller than the sample/standard volume fractions. Correction factors for nucleogenic interferences during irradiation were determined from irradiated CaF_2 and K_2SO_4 as follows: $(^{39}Ar/^{37}Ar)Ca = 7.06 \times 10^{-4}$, $(_{36}Ar/_{37}Ar)Ca = 2.79 \times 10^{-4}$ and $(_{40}Ar/_{39}Ar)K = 0.0297$. Mass discrimination was monitored by running calibrated air shots. The mass discrimination during these experiments was 1.3% per mass unit. While doing the experiments, calibration measurements were made weekly to monthly to check for changes in mass discrimination. No significant variation was seen during these intervals.

Field Results

I identified four fracture sets with common orientations, opening modes, and relative ages across the study area. I visited 58 stations spanning 100 kilometers from the Iniskin Bay in the south to Tuxedni bay in the north (figure 1.4, 1.5, 1.6). I measured fractures in strata ranging in age from Oligo-Miocene (Seldiovian strata) – latest Triassic (Kamishak Formation) (figure 1.2, 1.6).

The field area is divided into two structural domains: 1) The Iniskin Peninsula, where an anticline–syncline pair is preserved and the predominant sense of slip on the southwest-striking Bruin Bay Fault is thrust; 2) the area north of Chinitna Bay where the Bruin Bay Fault strikes ~N–S and preserves primarily sinistral displacement (figure 1.4). Below I list the average strike of each fracture set for each domain, document their relative ages, and discuss the distribution of fracture sets for each domain.

Regional Overview of Fracture Character

There are four fracture sets in the study area (figure 1.6, 1.8). Commonly there are two dominant sets at each station (figure 1.6a; 1.6b). The first is the approximately regional structure-normal 310° fracture set, at 53/ 56 stations, with an average strike of 312° ±1.3° (95% 2σ confidence interval). The second is the approximately regional structure-parallel 210° fracture set, at 30/ 56 stations, with an average strike of 214° ±2.0˚ (95% 2σ confidence interval). Two subsets oblique to these main fracture sets are sparser (figure 1.6c, 1.6d). These are: 1) the 250° fracture set, at 28/56 stations, with an average strike of 252° ±2.5° (95% 2σ confidence interval); and 2) the 360° fracture set, at 28/56 stations, with an average strike of 357° ±2.2° (95% 2σ confidence interval).

The structure-normal fracture set (310°), when present, was easiest to identify at each outcrop. It is the most frequent, longest, and frequently cross cuts all other fracture sets (figure 1.9). The 310° fractures are commonly cemented with calcite (occasionally smectite and quartz). They are well developed and

regularly spaced. Frequently, the 310° fracture set shows evidence of mode II opening or shear because it displaces other fracture sets, and preserves fault kinematic indicators on exposed surfaces (figure 1.8; 1.10; 1.11). At several stations, this fracture set forms conjugates with the 360° fracture set (figure 1.10; 1.11).

The structure parallel fracture set (210°) is the second most frequent. The 210° set is commonly orthogonal to sub-orthogonal to the 310° set, well developed, and preserves calcite filled joints with minor quartz and smectite vein fill (figure 1.8; 1.12; 1.13). The 210° fracture set commonly occurs with the 310° fracture set, and they often cross cut one another suggesting a shared inception (figure 1.8).

The 250° fracture set commonly manifests as joints or veins that are variably filled with calcite and minor smectite and quartz. They are rarely well developed, have shorter average length, and typically only occur as a minor population of fractures at each outcrop (figure 1.8; 1.12; 1.13). Abutting and cross-cutting relationships for this fracture set are erratic; however, clear cross-cutting relationships at some stations suggest that at some outcrops this fracture set is older than the 310° and 360° fracture sets (figure 1.11). In contrast to this observation, at one station, this fracture set forms a conjugate pair with a fracture set oriented 310° (figure 1.10c).

The 360° fracture set is generally represented by poorly developed shear fractures or veins which are variably filled with calcite depending on outcrop preservation. Frequent conjugate geometries, and in some instances, antithetic shearing, between the 310° and 360° fracture sets at some stations suggests a similar origin and a conjugate relationship between the two fracture sets, wherein the 310° fracture set preserves dextral shear and the 360° fracture set preserves sinistral shear (figure 1.10, 1.1)

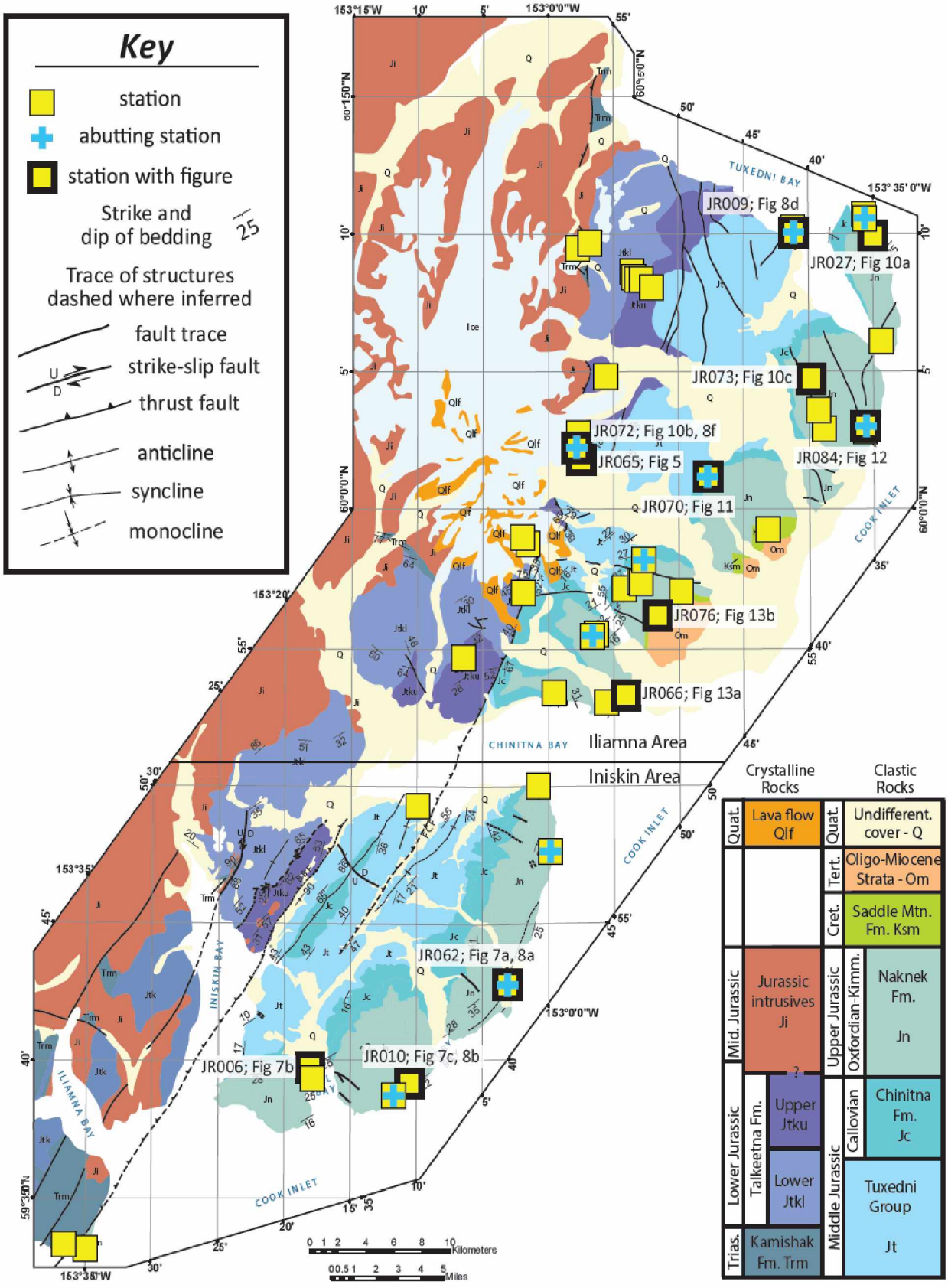
Key
station
abutting station
station with figure
Strike and dip of bedding
25
Trace of structures dashed where inferred
fault trace
strike-slip fault
thrust fault
anticline
syncline
monocline
JR009; Fig 8d
JR027; Fig 10a
JR073; Fig 10c
JR072; Fig 10b, 8f
JR065; Fig 5
JR084; Fig 12
JR070; Fig 11
JR076; Fig 13b
JR066; Fig 13a
JR062; Fig 7a, 8a
JR006; Fig 7b
JR010; Fig 7c, 8b
Iliamna Area
Iniskin Area
TUXEDNI BAY
CHINITNA BAY
INISKIN BAY
ILIAMNA BAY
COOK INLET
Ice
0 1 2 4 6 8 10 Kilometers
0 0.5 1 2 3 4 5 Miles
Crystalline Rocks
Clastic Rocks
Quat.
Lava flow Qlf
Undifferent. cover - Q
Tert.
Oligo-Miocene Strata - Om
Cret.
Saddle Mtn. Fm. Ksm
Mid. Jurassic
Jurassic intrusives Ji
Upper Jurassic
Oxfordian-Kimm.
Naknek Fm. Jn
Lower Jurassic
Talkeetna Fm.
Upper Jtku
Lower Jtkl
Middle Jurassic
Callovian
Chinitna Fm. Jc
Tuxedni Group Jt
Trias.
Kamishak Fm. Trm

Figure 1.4 Simplified Geologic Map with Stations
Simplified geologic map of the study area with stations where I measured orientations (yellow squares), where I measured orientations and made a figure (yellow square with thick black rim), and where I documented abutting relationships (blue cross). Map modified from Betka and Gillis (2015). A black line through Chinitna Bay separates domains. Figure numbers listed next to the black-rimmed yellow square that corresponds to that station.

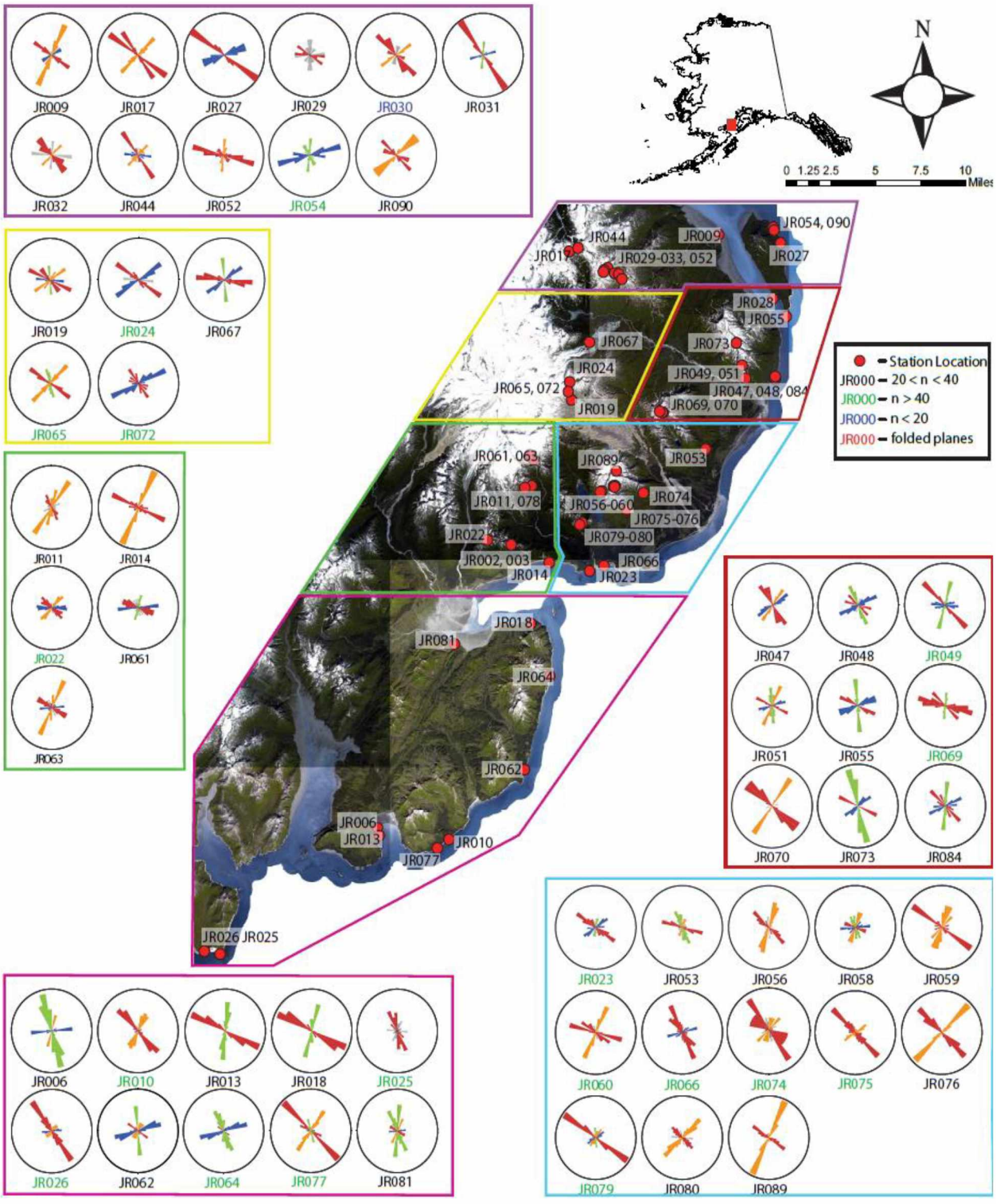
JR009
JR017
JR027
JR029
JR030
JR031
JR032
JR044
JR052
JR054
JR090
JR019
JR024
JR067
JR065
JR072
JR011
JR014
JR022
JR061
JR063
JR018
JR081
JR064
JR062
JR006
JR013
JR010
JR077
JR026
JR025
JR047
JR048
JR049
JR051
JR055
JR069
JR070
JR073
JR084
JR023
JR053
JR056
JR058
JR059
JR060
JR066
JR074
JR075
JR076
JR079
JR080
JR089
JR044
JR009
JR054, 090
JR017
JR029-033, 052
JR027
JR028
JR055
JR067
JR073
JR024
JR049, 051
JR065, 072
JR047, 048, 084
JR019
JR069, 070
JR061, 063
JR089
JR053
JR011, 078
JR056-060
JR074
JR075-076
JR022
JR079-080
JR002, 003
JR066
JR014
JR023
JR018
JR081
JR064
JR062
JR006
JR013
JR010
JR077
JR026 JR025
N
0 1.25 2.5 5 7.5 10
Miles
Station Location
JR000 – 20 < n < 40
JR000 – n > 40
JR000 – n < 20
JR000 – folded planes

Figure 1.5 Stations with Fracture Orientations Depicted By Color Coded Rose Diagrams
Stations with color-coded Rose diagrams representing the observed fracture sets. Red dots on the map denote the station locations, with their numbers shown in white boxes. The station names are listed above their corresponding Rose diagrams, which are grouped by geographic region in color-coded boxes along the sides of the figure. Fracture orientations shown in the Rose diagrams were modified by restoring local bedding to horizontal. In the Rose diagrams, the outer ring represents 30 percent of data, except at stations 31 and 89, which represent 40 percent. Red petals show the 310° fracture set, orange petals represent the 210° fracture set, green petals represent the 360° fracture set, and blue petals represent the 250° fracture set. Gray petals are fractures that had widely varying dips and did not cluster. These colors are used throughout to represent the same fracture sets in later figures. Total n value is 2054/2243. Fractures excluded from this figure include those measured in strata whose stratigraphic unit was unclear or lacking reliable bedding, however, the Rose diagrams shown here include "noise" measured at each station. "Noisy" fractures did not fall into clearly defined sets but generally represented a small proportion of the data collected at each station.

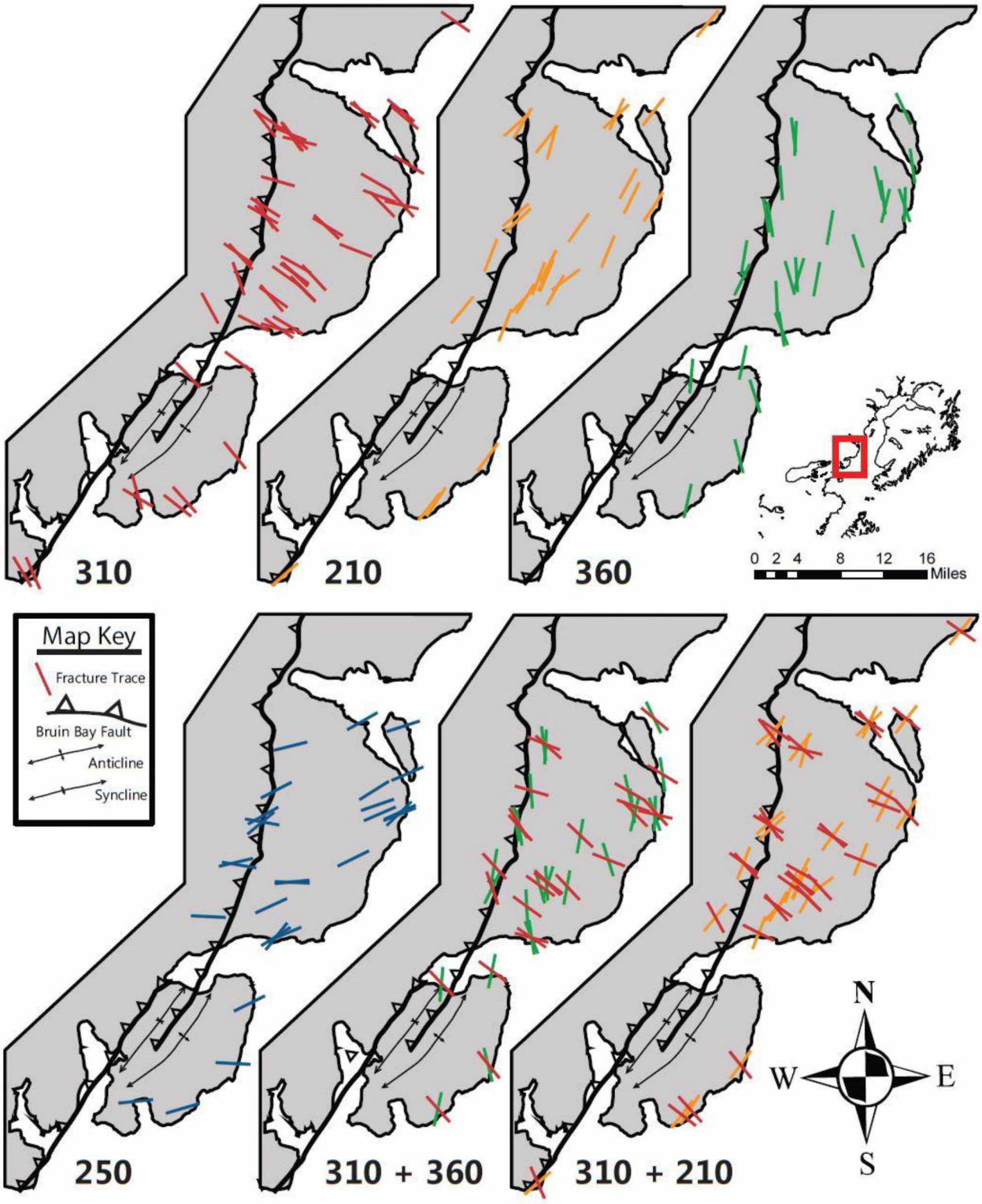

Figure 1.6 Spatially Referenced Fracture Traces
Fracture traces measured in the field and organized into sets as shown in Figure 1.5. These fractures have been rotated about a horizontal axis that restored bedding to horizontal. Fractures are color-coded and labeled by set. Potential conjugate and orthogonal pairs are shown as 310 + 360 and 310 + 210, respectively.

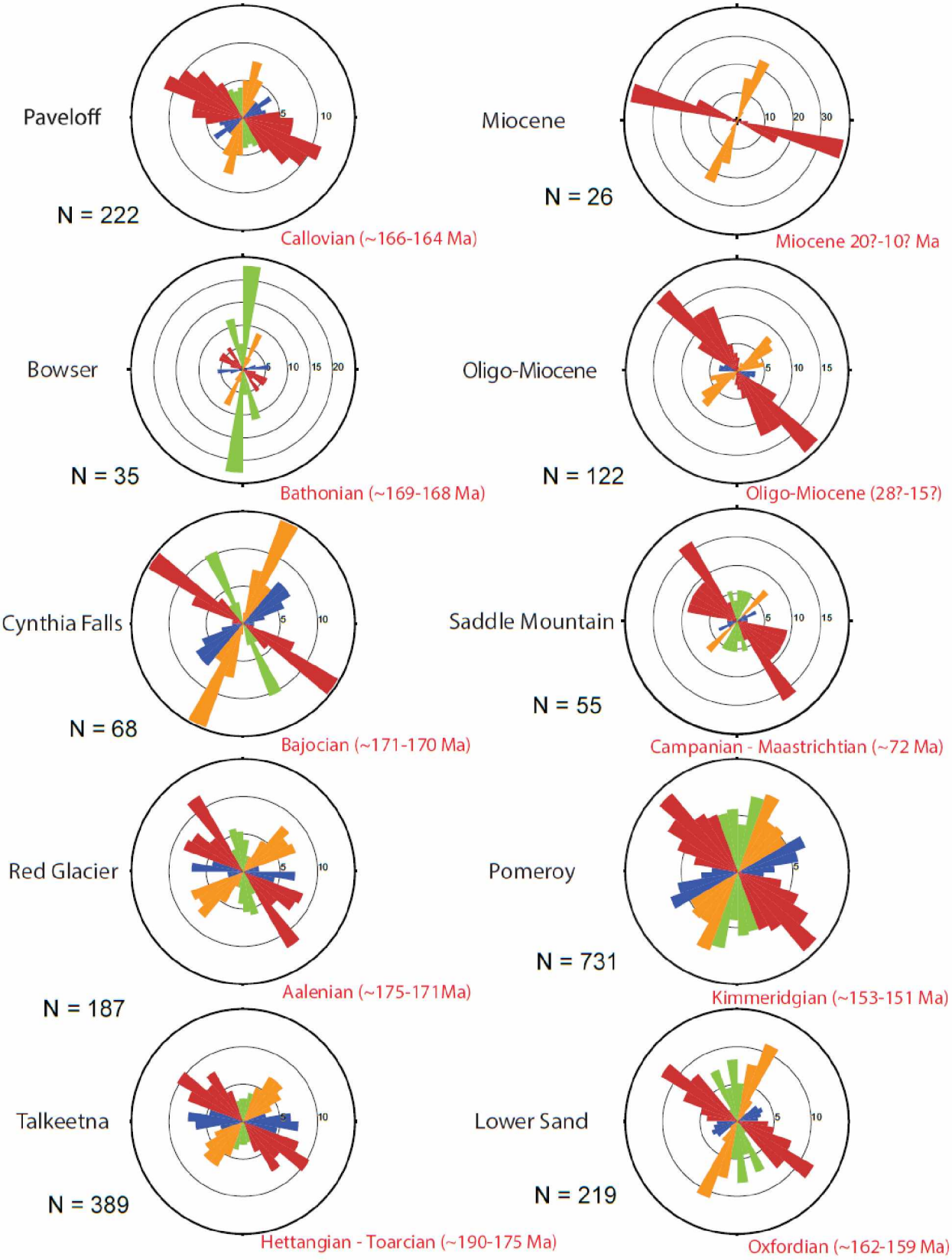
Paveloff
N = 222
Callovian (~166-164 Ma)
Miocene
N = 26
Miocene 20?-10? Ma
Bowser
N = 35
Bathonian (~169-168 Ma)
Oligo-Miocene
N = 122
Oligo-Miocene (28?-15?)
Cynthia Falls
N = 68
Bajocian (~171-170 Ma)
Saddle Mountain
N = 55
Campanian - Maastrichtian (~72 Ma)
Red Glacier
N = 187
Aalenian (~175-171Ma)
Pomeroy
N = 731
Kimmeridgian (~153-151 Ma)
Talkeetna
N = 389
Hettangian - Toarcian (~190-175 Ma)
Lower Sand
N = 219
Oxfordian (~162-159 Ma)

Figure 1.7 Stratigraphic Partitions of Fracture Sets
Rose diagrams of fracture sets organized in stratigraphic order, from oldest at the lower left to youngest at the upper right. See Figure 2 for station numbers used in the stratigraphic groupings. Rose diagrams are color-coded the same as previous figures. Rose diagrams represent orientations of fractures after bedding was restored to horizontal. N= 2054/2243. Fractures from stations where the stratigraphic unit was unclear or bedding orientation was indeterminable were excluded. These Rose diagrams include "noise" of non-conforming fractures measured at each station. Fracture stratigraphy and disappearance of older fracture sets up section is observed, for example, in the Oligo-Miocene and Miocene strata, where the 360° fracture set is absent.

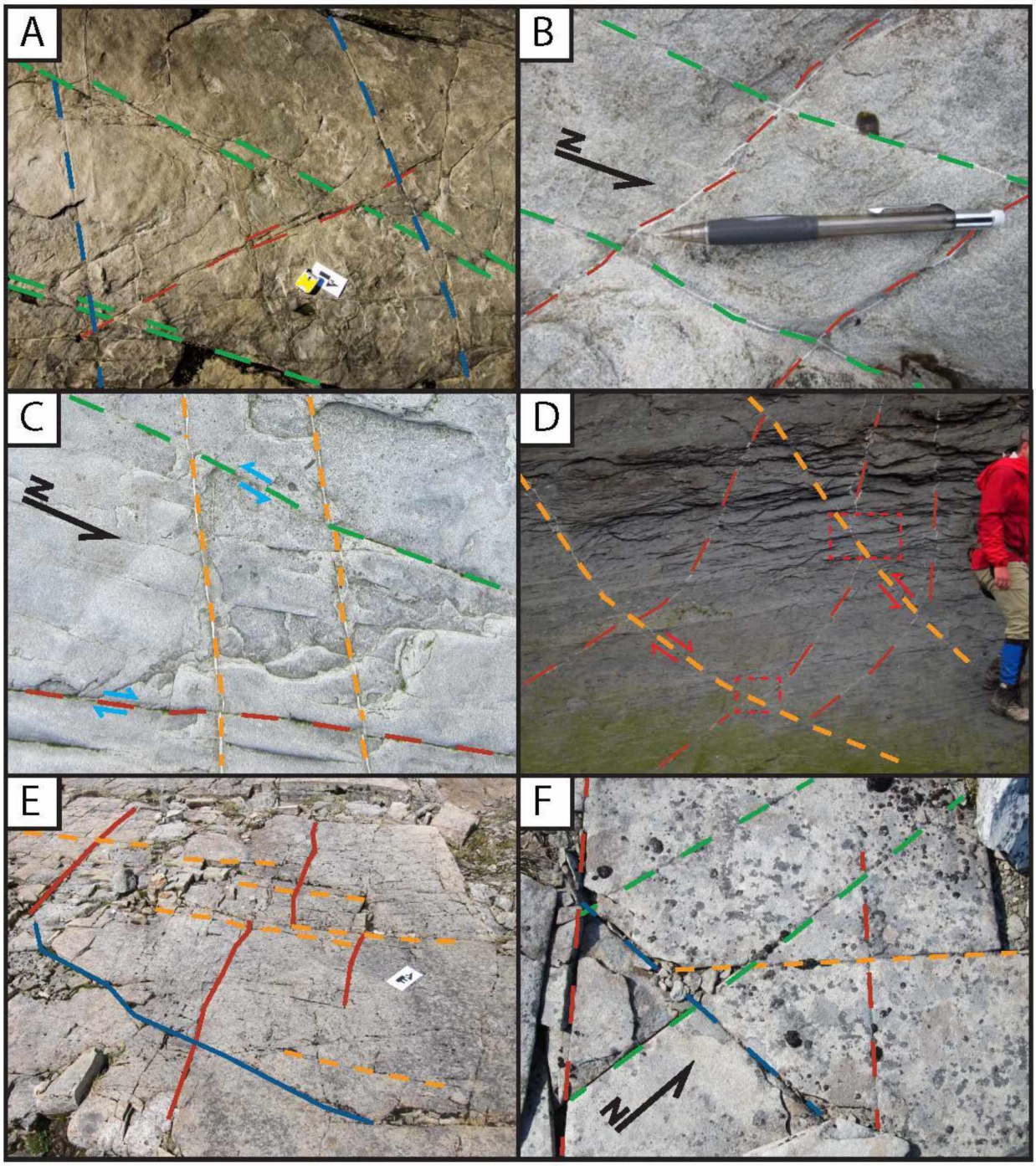

Figure 1.8 Annotated Field Photos Depicting Fracture Character
A) JR062 in the Pomeroy Formation. Fractures of the 310° (red) and 360° (green) sets form a conjugate pair and cross cut the 250° (blue) fracture set. B) JR010 in the Pomeroy Formation. Fractures of the 310° (red) and 360° (green) sets form a conjugate pair. C) JR062 in the Pomeroy Formation, with fractures of the 310° (red) and 360° (green) sets offsetting fractures of the 210° (yellow) set. D) JR009 in the Cynthia Falls Formation. Yellow fractures of the 210° set offset red fractures of the 310° set. E) JR072 in the Red Glacier Formation. See blue box in figure 9b for location of photo in outcrop context. Three of the four common fracture sets are shown (310° red, 210° yellow, and 250° blue). F) JR073 in the Pomeroy Formation, with the four fracture sets of the study area (the yellow line is ~0.5 m).

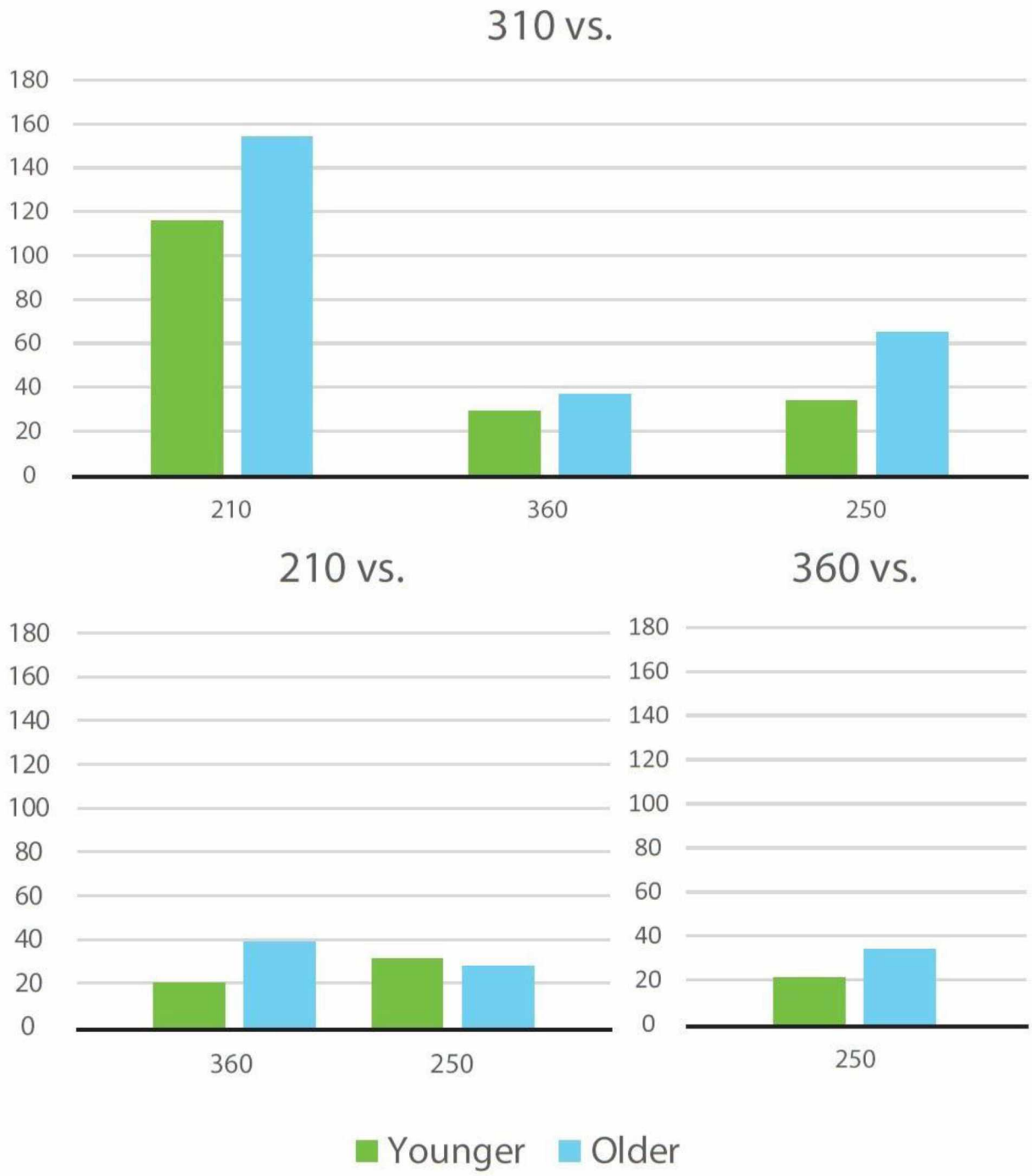

Figure 1.9 Abutting Relationships
Regional abutting relationships reflect ambiguous trends and patterns. If blue bar is larger, than the designated fracture set is older than the fracture set listed at the top of the graph. The reverse is true if the green bar is bigger. Results show frequent mutual cross cuttings between all four fracture sets and that clear trends do not emerge.

Field Results from Each Domain

Iniskin Peninsula

The Iniskin Peninsula is located south of Chinitna Bay and North of Iniskin Bay on the western side of the Cook Inlet (figure 1.2). I measured veins and fractures in ten sites selected primarily in well-exposed coastal pavements on the eastern flanks of the peninsula (n=6), but also in some well-exposed vertical outcrops (n=4). The sampling strategy focused on six stratigraphic intervals: one station was in the Kamishak Limestone, one in the Bowser Formation, one in the Paveloff Siltstone, one in the Lower Sandstone Member of the Naknek Formation, three in the Pomeroy Arkose Member of the Naknek Formation, and one in the undifferentiated part of the Naknek Formation (figure 1.4, 1.5). Seven stations (JR006, JR010, JR013, JR018, JR062, JR064, and JR077) are located in the eastern limb (forelimb) of the Fitz Creek anticline, and one (JR081) in the western limb (backlimb). Fracture patterns in the forelimb and backlimb were similar (figure 1.7), though a strong sampling bias exists in the forelimb. This was largely due to limited outcrop accessibility, dense bear habitat, thick vegetation, and poor exposures further inland on the peninsula. One station (JR026) is located in the hanging wall of the Bruin Bay Fault, and the final station (JR025) is in a footwall syncline of the Bruin Bay Fault. Abutting relationships were chronicled at three of the 11 stations.

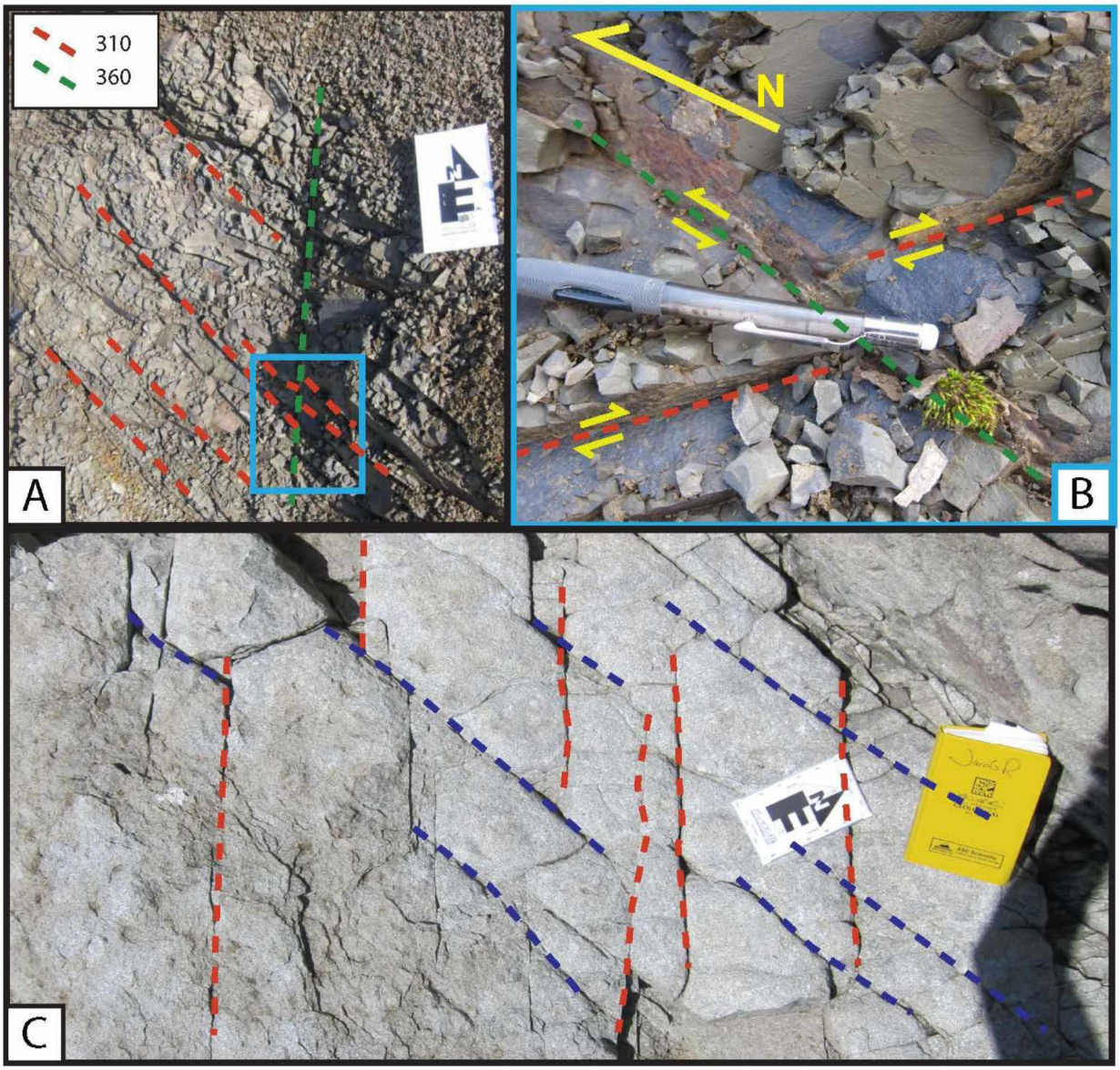

Figure 1.10 Conjugate Fractures at stations JR070 and JR027
A) View of the outcrop showing the two dominant fracture sets at this location. Note blue box for location of (B). B) Zoomed location of blue box in (A). Note conjugate angular relationship between the 310° and 360° fracture sets. Note slickenslides on fracture faces on the top right and top left with opposing senses of shear, further supporting a conjugate relationship in this location. C) Conjugate fractures of the 310° and 250° fracture sets at station JR027 in the Chisik Conglomerate.

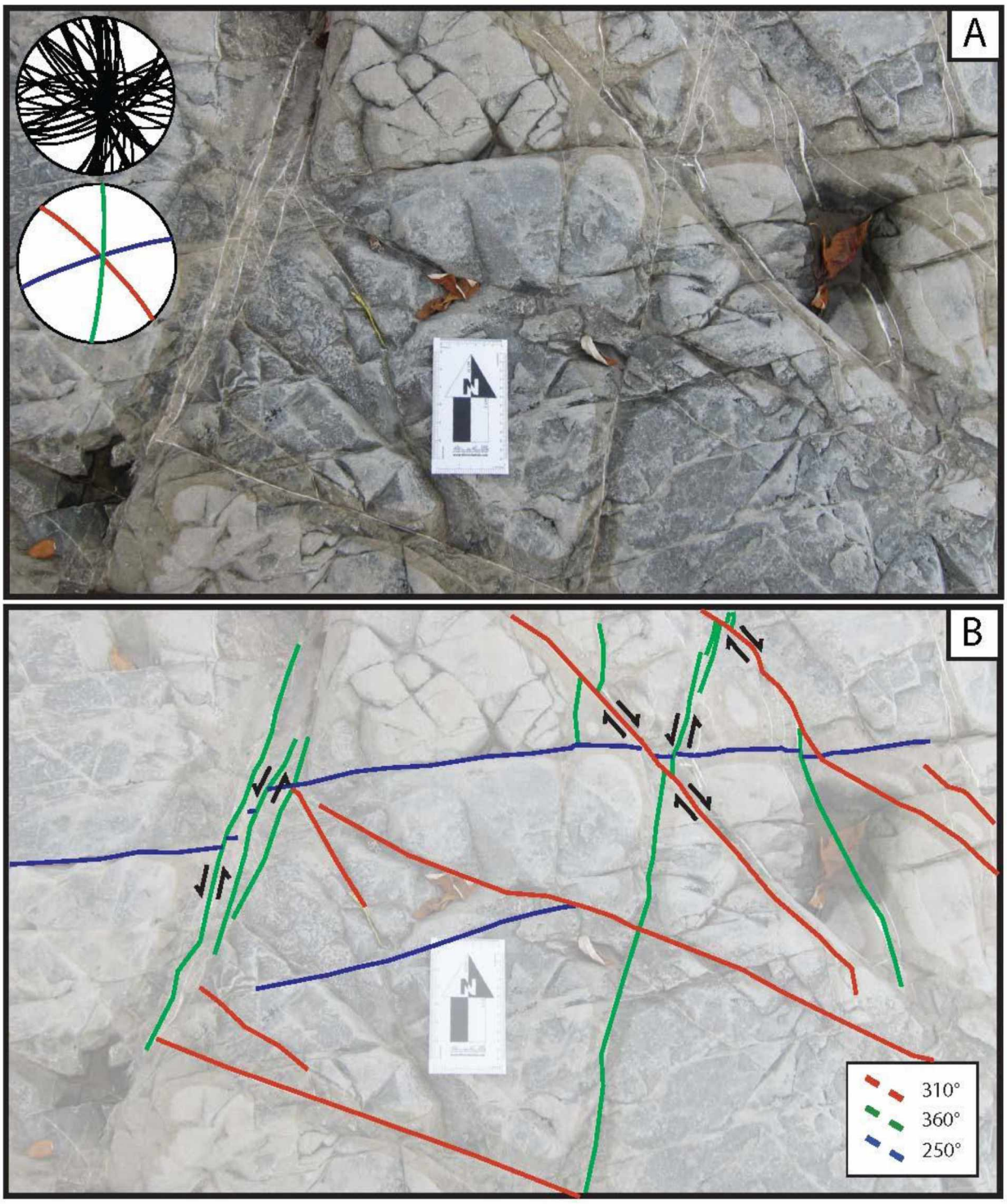

Figure 1.11 Conjugate Fractures at JR084
A) Field measurements shown on top stereonet are shown in the same colors as used in (B) to trace the fractures.. B) Interpreted photo from A showing three major sets and their cross-cutting relationships. Note opposing senses of shear and conjugate angular relationships between the 310° and 360° fracture sets.

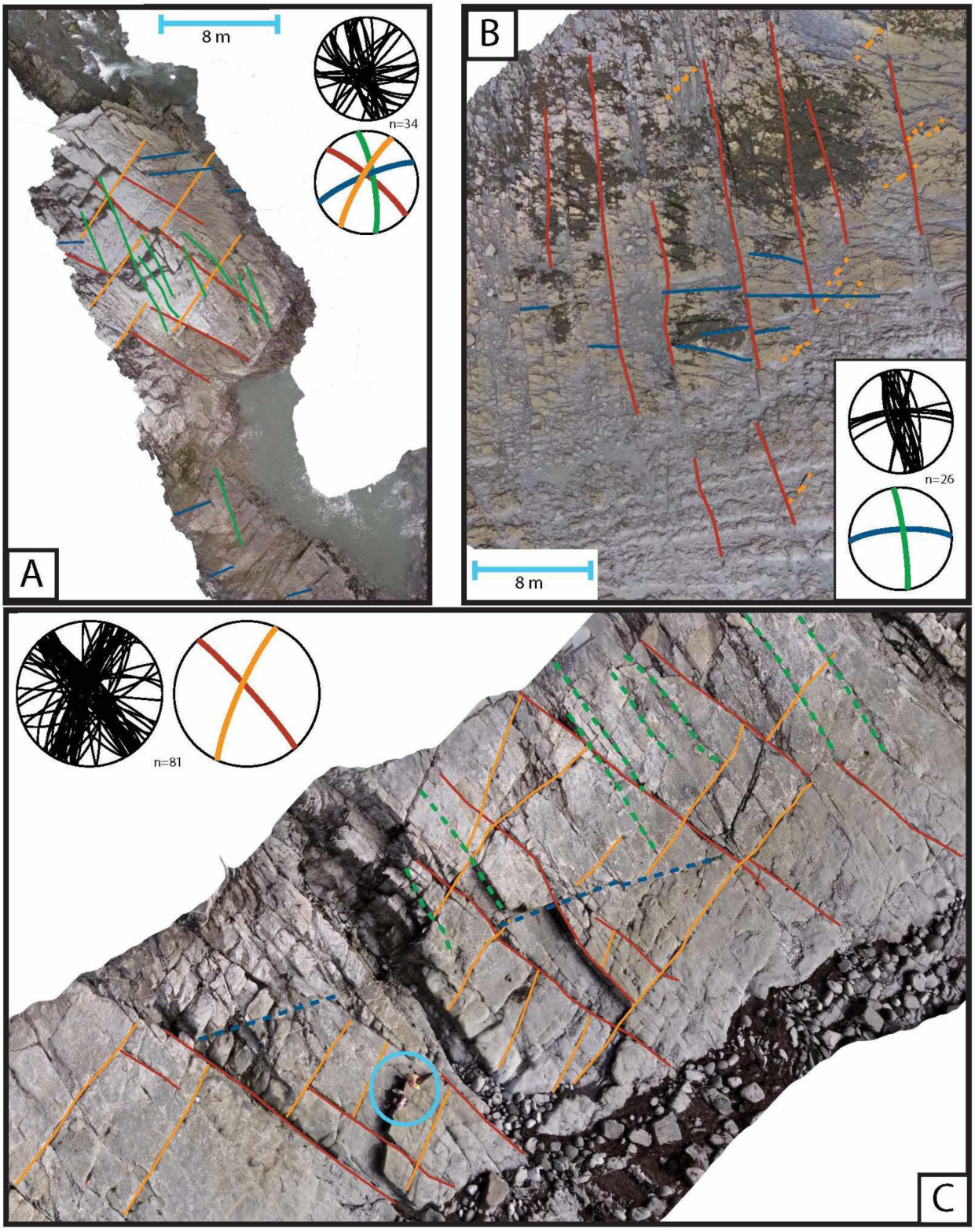
8 m
n=34
A
B
n=26
8 m
n=81
C

Figure 1.12 Aerial Photo Mosaics from the Iniskin Peninsula, with Measured Fractures
Lineaments drawn on the images are the identified fracture sets. The colors match the bottom stereonet. Black and white stereonets depict field measurements, with the n value given. Color-coded strereonets show the mean orientations for each fracture set traced on the aerial images. Fracture lineaments drawn on photo mosaics may not match the field measurements on the stereonets because field work sampled smaller areas. (Dashed lines are fractures observed in the aerial photos but not included in the stereonets.) A) Station JR062 in the Pomeroy Arkose Member of the Naknek Formation. This coastal exposure displays the four common fracture sets in the Iniskin Peninsula domain. Figure 8a shows a nearby outcrop. B) Station JR006 in the Paveloff Member. This coastal exposure shows the four common fracture sets on the Iniskin Peninsula in different relative densities than (A) and (C). C) Station JR010 in the Pomeroy Arkose Member of the Naknek Formation. This coastal exposure again shows the four common fracture sets on the Iniskin Peninsula in similar densities to (A). Figure 8b is a detailed view of conjugate fractures at this location. All photos are oriented with north at the top.

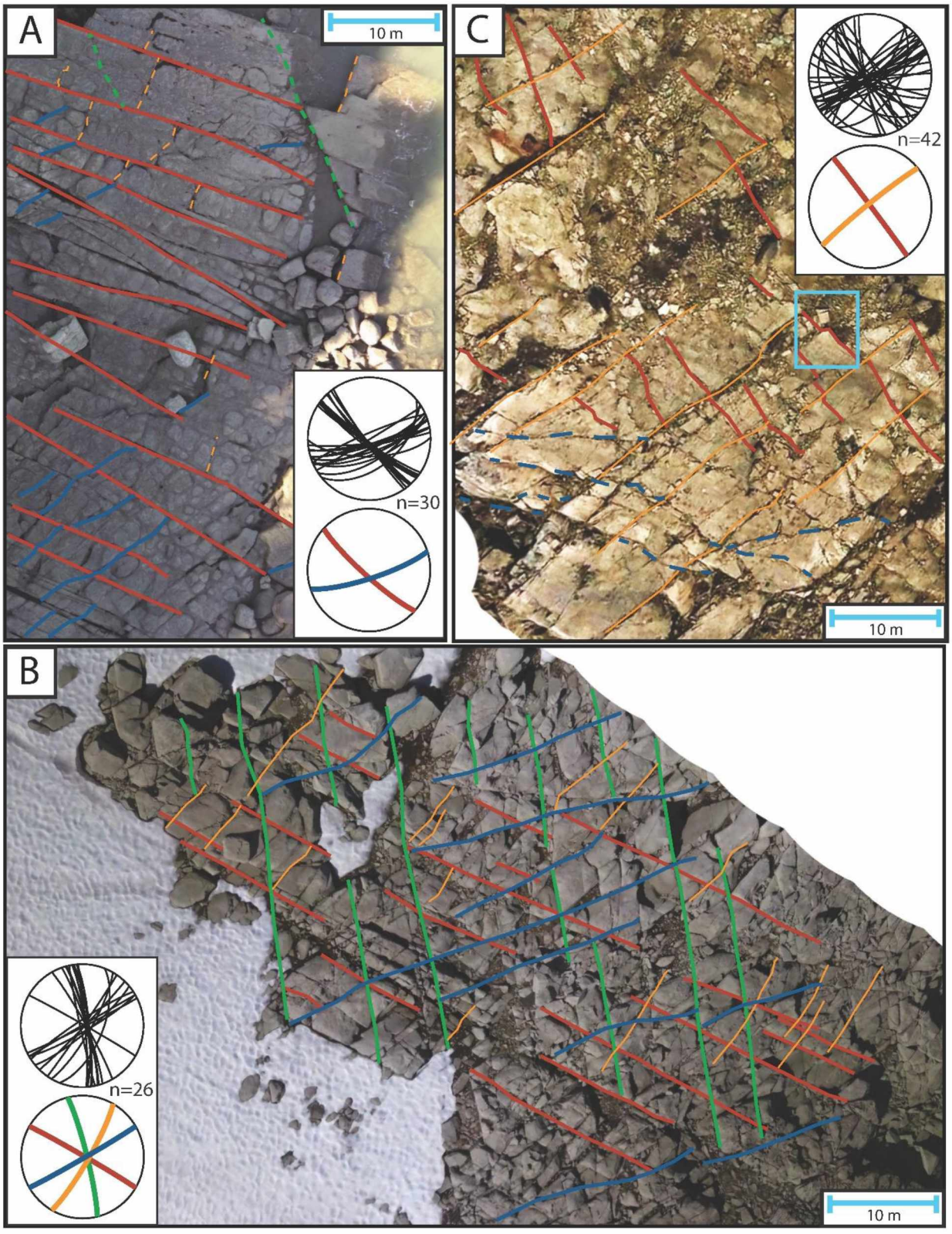
A
10 m
n=30
C
n=42
10 m
B
n=26
10 m

Figure 1.13 Aerial Photo Mosaics from the Iliamna Region
Lineaments drawn on the images are the identified fracture sets. The colors match the bottom stereonet. Black and white stereonets depict field measurements, with the n value given. Color-coded strereonets show the mean orientations for each fracture set traced on the aerial images. Fracture lineaments drawn on photo mosaics may not match the field measurements on the stereonets because field work sampled smaller areas. (Dashed lines are fractures observed in the aerial photos but not included in the stereonets.) . A) Station JR027 in the Chisik Conglomerate Member of the Naknek Formation on Chisik Island. Note dominance of 310° fracture set and minor presence of other fracture sets. B) Station JR072 in the Red Glacier formation. 310° and 210° fracture sets are dominant with a minor presence of the 250° fracture set. See figure 8e for detail. C) Station JR073 in the Pomeroy. Note presence of all four fracture sets in variable abundance. See figure 8f for detail.

All stations show similar fracture character with predominantly mode I fractures and veins filled with calcite. All fracture sets exhibited less frequent small shear displacements. Almost all observed fractures were perpendicular to bedding, becoming sub-vertical when bedding was restored to horizontal. On the basis of consistent orientations and relative ages, the fractures were divided into four sets: 1) the 310° fracture set, present at 9/10 stations; 2) the 210° fracture set, present at 4/10 stations; 3) the 250° fracture set, present at 4/10 stations; and 4) the 360° fracture set, present at 5/10 stations.

The 310° set is present at 9/10 stations and has average strike of 321° ± 2.7° (95% 2σ confidence interval) on the Iniskin Peninsula. This fracture set was commonly the most dominant, well developed, and typically had the longest lengths of fracture sets at each location (3-5m) (figure 1.12). The 310° fracture set was generally filled with calcite and minor quartz. These fractures are dominantly joints with mode I opening displacements as evidenced by abundant plumose structures and twist hackles. The 310° fracture set appears to have been sheared, or occasionally manifests as right lateral shear fractures as evidenced by principally right lateral displacements (JR010, JR062) (figure 1.8a, 1.8b). The 310° fracture set was present in all observed stratigraphic intervals. The 310° set mutually cross cuts with all present fracture sets, and therefore age is difficult to determine; however, on average this fracture set might be among the youngest because it cross cuts the other observed fracture sets with a slightly higher frequency than it is cross cut (slightly higher than 50 percent) (figure 1.9).

The 210° fracture set was present at 4/10 stations and has an average strike of 217° ± 5.6° (95% 2σ confidence interval). This fracture set was also well developed when present, regularly spaced, and was frequently in between 2-4 meters in length. This fracture set is dominantly filled with calcite, with minor quartz and smectite. The 210° fractures were predominantly mode I, though some exhibited small sinistral shear displacements. These fractures were frequently cross cut by fractures of the 310° set but in some instances the fractures appear to be mutually crosscutting (figure 1.8c, 1.8d). Because this fracture set frequently crosscuts other fracture sets, it could be among the youngest expressed on the Iniskin Peninsula. However, the trends are ambiguous (figure 1.9).

The 250° fracture set was present at 4/10 stations with an average strike of 245° ± 6.7° (95% 2σ confidence interval). This fracture set was typically poorly developed, and generally filled with calcite when fracture fill was preserved. The 250° fracture set had shorter fracture lengths on average than other fracture sets (1-2m), and was only dominant at one station (JR064). At this station, the 310° and 210° fracture sets were only in minor abundance, and typically abutted the 250° fracture set. Frequently, this fracture set in this area was among the older fracture sets (figure 1.9).

The 360° fracture set was present at 5/10 stations with an average strike of 358° ± 4.5° (95% 2σ confidence interval). This fracture set was often well developed. In some instances, the 360° fracture set appears to share a conjugate geometry with the 310° fracture set suggesting perhaps multiple openings of the 310° fracture set (figure 1.8a; 1.8b).

North of Chinitna Bay

I visited 46 outcrops in the area north of Chinitna Bay. Rugged high-country exposures are preserved in this area, limiting wildlife and vegetation concerns. Intertidal zones however, often buried or submerged coastal pavements, making the collection of quality abutting relationship data difficult. There are no major folds in this portion of the study area and most strata dip east, away from the orogen and the Bruin Bay Fault. Exposures in the Talkeetna Formation, often in the footwall of the Bruin Bay Fault, provide an opportunity to assess the possibility that fractures here are fault-related. 37 stations were visited at well-exposed vertical outcrops, and 9 stations (figure 1.4) were on pavement outcrops where I could establish relative ages. I visited nine stratigraphic intervals with ten stations in the Talkeetna Formation, six stations in the Red Glacier Formation, two stations in the Cynthia Falls Formation, five stations in the Paveloff Member of the Chinitna Formation, two stations in the Lower Sandstone Member of the Naknek Formation, one station in the Chisik Conglomerate Member of the Naknek Formation, fifteen stations in the Pomeroy Member of the Naknek Formation, one station in the Saddle Mountain succession, and four stations in Oligo-Miocene strata (figure 1.2; 1.4).

Fracture character was similar at the 46 stations, with predominantly mode I fractures and veins which were variably filled with calcite and minor quartz. Fractures commonly restore to vertical when bedding is restored to horizontal. Thus, I interpret the fracture sets after bedding dip has been removed. Because of similar orientations and relative ages in this portion of the study area I divide the fractures into the same sets as on the Iniskin Peninsula. The 310° fracture set is present at 44/46 stations; the 210° fracture set is present at 26/46 stations; the 250° fracture set is present at 24/46 stations; and the 360° fracture set is present at 23/46 stations (figure 1.5, 1.6).

The 310° fracture set had an average strike of 308° ± 1.7° (95% 2σ confidence interval). The results of the abutting relationship data are ambiguous, though this fracture set appears to be younger ~60% of the time (figure 1.9). In some cases cross-cutting relationships suggest that this fracture set is younger than the 250° fracture set and coeval with the 360° and 210° fracture sets (figure 1.8; 1.10; 1.11). This fracture set occasionally showed evidence of dextral shear, was commonly cemented with calcite and minor quartz, and was frequently dominant at stations where it was present (figure 1.8; 1.10; 1.11;

1.13). This fracture set was present in all nine stratigraphic units, including the youngest strata (figure 1.7). At JR066 in the Oligo-Miocene strata, shear veins preserved calcite fill (JR066) (figure 1.14a). Veins at one other station in the Oligo-Miocene strata were only filled with quartz, which potentially suggests that quartz vein precipitation is an Oligo-Miocene phenomenon (JR076) (figure 1.14b). There are several stations where the 310° and 360° fracture sets appeared to be mutually crosscutting (JR084, JR082, JR090) (figure 1.10; 1.11). The 310˚ fracture set was also documented in the youngest observed stratigraphic unit in Oligo – Miocene aged rocks north of Tuxedni Bay (figure 1.6; 1.7).

The 210° fracture had an average strike of 213° ± 2.1° (95% 2σ confidence interval). The 210° fractures are well developed when present and second longest. They typically form orthogonal to the 310° fracture set (figure 1.8e; 1.8f; 1.13). The results of abutting relationship analysis for this fracture set is ambiguous (figure 1.9). However, at several stations, this fracture set appears to be mutually cross cutting with the 360° and 310° fracture set suggesting similar ages (figure 1.8c; 1.8d). This fracture set is also present in the Oligo-Miocene strata and is therefore likely among the youngest fracture sets as some fracture sets were not sampled in these younger rocks (360°) (figure 1.7).

The 250° fracture set had an average strike of 251° ± 2.7° (95% 2σ confidence interval). This fracture set was generally poorly developed, occasionally filled with calcite, and was primarily composed of mode I joints and veins. Cross cutting relationships at several stations indicate that this fracture set is older, as it is frequently offset by younger fractures of the 210° and 310° fracture sets (figure 1.8a, 1.10, 1.11). This fracture set was sampled at one station in the Oligo-Miocene strata, so it must post date deposition of those rocks.

The 360° fracture set had an average trend of 357° ± 2.6° (95% 2σ confidence interval). This fracture set was generally well developed, occasionally filled with calcite, and manifested as shear fractures with small displacements (figure 1.10; 1.11; 1.13). The 360° set had apparent conjugate geometries with the 310° fracture set, and often antithetic shearing (figure 1.10; 1.11). The 360° set was mutually cross cutting with the 310° fracture set which suggests that these two fracture sets could have been active at the same time (figure 1.10; 1.11). This fracture set was not present in the sampled Oligo-Miocene strata.

Strike Test Results

Strike tests were performed using the refined weighted least squares method of Yonkee and Weil (2010a) for the 310°, 210°, 250°, and 360° fracture sets, and the results are shown in figure 1.15.

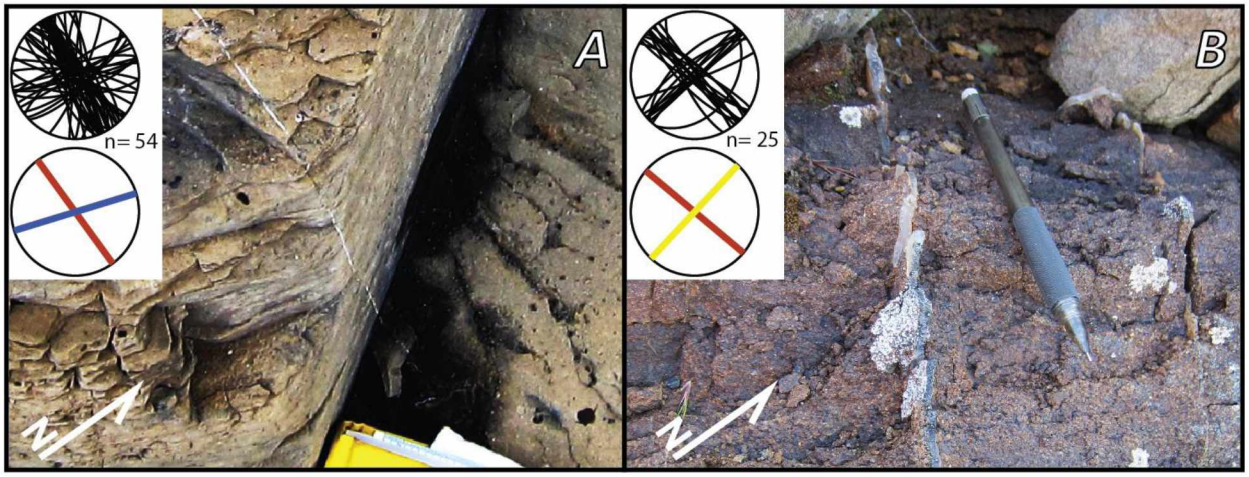

Figure 1.14 Filled Fractures in Oligo-Miocene Strata
Photos of stations JR066 and JR075. Top stereonet depicts field measurements with the n value below. The color coded bottom strereonet represents the mean fracture set orientations for each observed fracture set. A) Calcite filled vein of the 250° fracture set with the top of a field notebook for scale. B) Quartz filled veins of the 310° fracture set with pencil for scale.

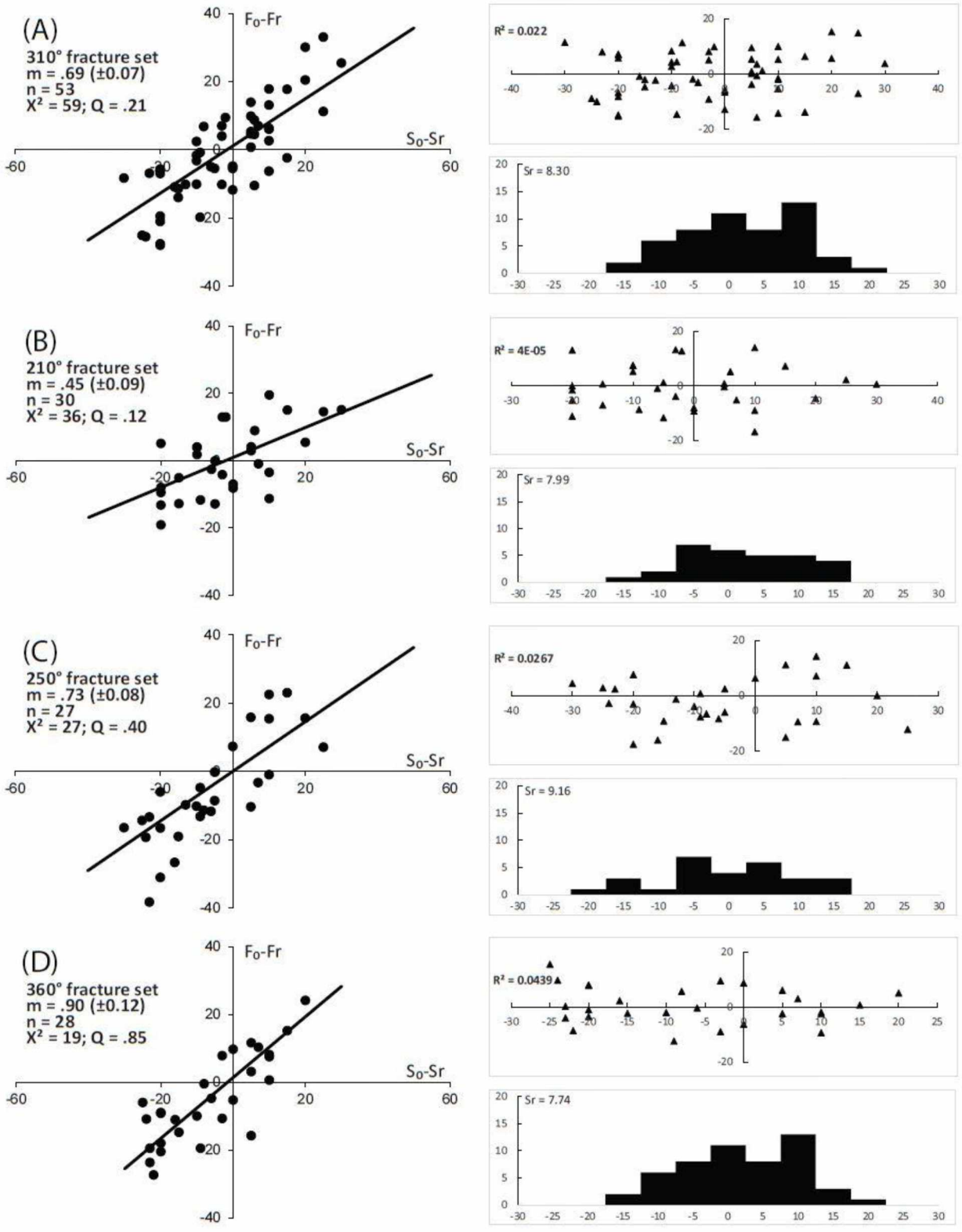
(A)
310° fracture set
m = .69 (±0.07)
n = 53
X² = 59; Q = .21
Fo-Fr
So-Sr
R² = 0.022
Sr = 8.30
(B)
210° fracture set
m = .45 (±0.09)
n = 30
X² = 36; Q = .12
Fo-Fr
So-Sr
R² = 4E-05
Sr = 7.99
(C)
250° fracture set
m = .73 (±0.08)
n = 27
X² = 27; Q = .40
Fo-Fr
So-Sr
R² = 0.0267
Sr = 9.16
(D)
360° fracture set
m = .90 (±0.12)
n = 28
X² = 19; Q = .85
Fo-Fr
So-Sr
R² = 0.0439
Sr = 7.74

Figure 1.15 Strike Test Results for the Four Regional Fracture Sets
Best fit slopes (m), 95 % confidence intervals, number of sites (n), total weighted misfit (X^2), and goodness of fit (Q) listed. X axis in left plot represents deviation from structural trend, and Y axis represents the expected orientation of a fracture set given a certain structural trend. In top right plot, residuals are plotted versus the X value of the strike test plot. In bottom right, distribution of residual size and frequency of size is shown with standard deviation (Sr) A) Orientations of fractures of the 310° fracture set. Reference orogen strike is 40° and reference fractures strike is 310°. These fractures and their strike test define a slope of 0.69 (±0.07). B) Orientations of fractures of the 210° fracture set. Reference orogen strike is 35° and reference fracture strike is 215°. These fractures and their strike test define a slope of 0.45 (±0.09). C) Orientations of fractures of the 250° fracture set. Reference orogen strike is 40° and reference fracture strike is 260°. These fractures and their strike test define a slope of 0.73 (±0.08). D) Orientations of fractures of the 360° fracture set. Reference orogen strike is 40° and reference fracture strike is 360°. These fractures and their strike test define a slope of 0.90 (±0.12).

The strike test slope for the 310° fracture set is .69 ±0.07 [n=53]; for the 210° fracture set 0.45 ±0.09 [n=30]; for the 250° fracture set 0.73 ±0.08 [n=28]; and for the 360° fracture set 0.9 ±0.12 [n=28] (figure 1.15). A goodness of fit (Q) > 0.1 indicates a successful fit to weighted linear regressions, and the results for these strike tests have Q ranging from 0.12 to 0.85, indicating acceptable to good fits for each. All strike test slopes for all fracture sets demonstrate moderate correlation between the strike of bedding and the orientation of local fracture strike indicating progressive arc slip (Yonkee and Weil, 2010a).

GIS Results Overview

I traced 8339 lineaments on 2.5m resolution SPOT Satellite images—2695 were drawn in the study area outlined above, 1022 to the south of the study area, and 4097 to the north (figure 1.16). All regions showed the 310° fracture set. Densities of subsidiary fracture sets in each domain varied. Fractures measured via GIS are of similar frequency and orientations as those measured in the field, and I classify them as the same sets (figure 1.17).

Domains

Katmai (Red)

In the Katmai domain I measured 1022 lineaments. The 310° and 360° fracture sets show the strongest signatures, with equal-sized peak frequencies occurring at strikes of 310° and 360° (figure 1.17). The 210° set is present as a small peak at 211°.

Iniskin Peninsula (Yellow)

In the Iniskin Peninsula, there are two clear fracture sets amongst 1297 lineaments, the 310° and the 210°. The 310° fractures peak at 305° and the 210° fractures peak at 212°. The 310° fracture set shows a significantly stronger signature than the other fracture sets present (figure 1.16).

Iliamna Area (Blue)

I measured 1396 lineaments north of Chinitna Bay and south of Tuxedni Bay. Three fracture sets were detectable in the satellite imagery, the 310°, 210°, and 250°sets. The 310° fractures peak at a strike of 300°, the 210° fractures peak at 218°, and the 250° fractures peak at 245°. The 310° fracture set is again the most prevalent, however, the 210° and 250° fracture sets show stronger signatures than in the southern area. Again, while other fracture sets were traced, they are not strongly present (figure 1.16).

Redoubt Area (Purple)

North of Tuxedni Bay in the Redoubt area I measured 2018 lineaments. There are four fracture sets present, the 310°, the 210°, the 250°, and a previously unsampled E–W-oriented fracture set that bisects the 310° and 250° fracture sets. The 310° fractures strike 295°, the 210° fractures strike 210°, the 250° fractures strike 240°, and the final set of fractures strikes 270°. While the 310° set is the most prevalent, the frequency of 210° fractures is diminished, and the E-W and 250° sets are almost equal to the 310° fracture set (figure 1.16).

North of Redoubt, (Green)

North of Redoubt and south of Mount Spurr, I measured the same four fracture sets as in the Redoubt area amongst 1531 lineaments. The four observed fracture sets strike 310°, 218°, 245°, and 270°. Relative proportions between the four fracture sets were different than in the Redoubt area. The E-W fracture set is clearly the most frequent, followed by equal proportions of the 310° and 210° fracture sets, and lastly the 250° fracture set with the lowest occurrence (figure 1.16).

South of Mount Spurr (Orange)

In the Mount Spurr area I measured 1075 lineaments and again detect the same four fracture sets as in the previous two domains. The four observed fracture sets strike 302°, 213°, 245°, and 269°. Again, the relative proportions are different. The 310° and 210° fracture sets have the highest frequencies, followed by the E-W and the 250° fracture sets (figure 1.16).

K-Parameter Test Results

I performed the K-parameter test on the four regionally prominent fracture sets (figure 1.18). Fractures from the 250°, 310°, and 360° fractures sets demonstrate decreased dispersion as they are first rotated to restore bedding to horizontal, and then rotated about a vertical axis to restore bedding strike to the regional structural trend. Fractures of the 210° fracture set first show decreased dispersion when restoring bedding to horizontal, and then reflect increased dispersion when rotated about a vertical axis to restore bedding to a common strike. The bedding strike measured in the field is used when choosing how far to rotate the fracture data about a vertical axis, because technically speaking, the data has no bedding strike after restoring the bedding dip to horizontal.

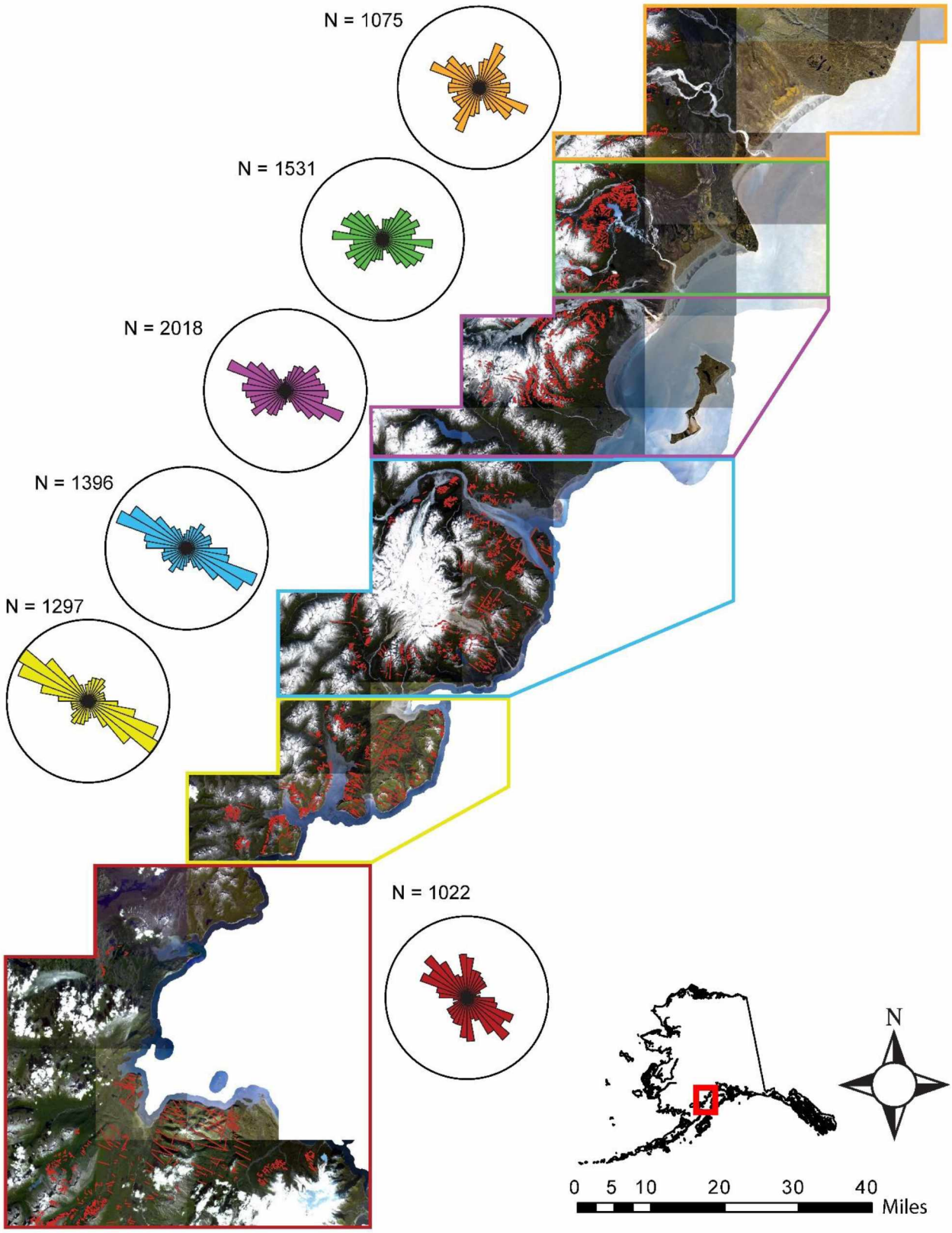

Figure 1.16 Spatial Distribution of Lineaments Drawn on Satellite Imagery
Rose diagrams are color coded to reflect their corresponding geographic location boxes. See text for discussion.

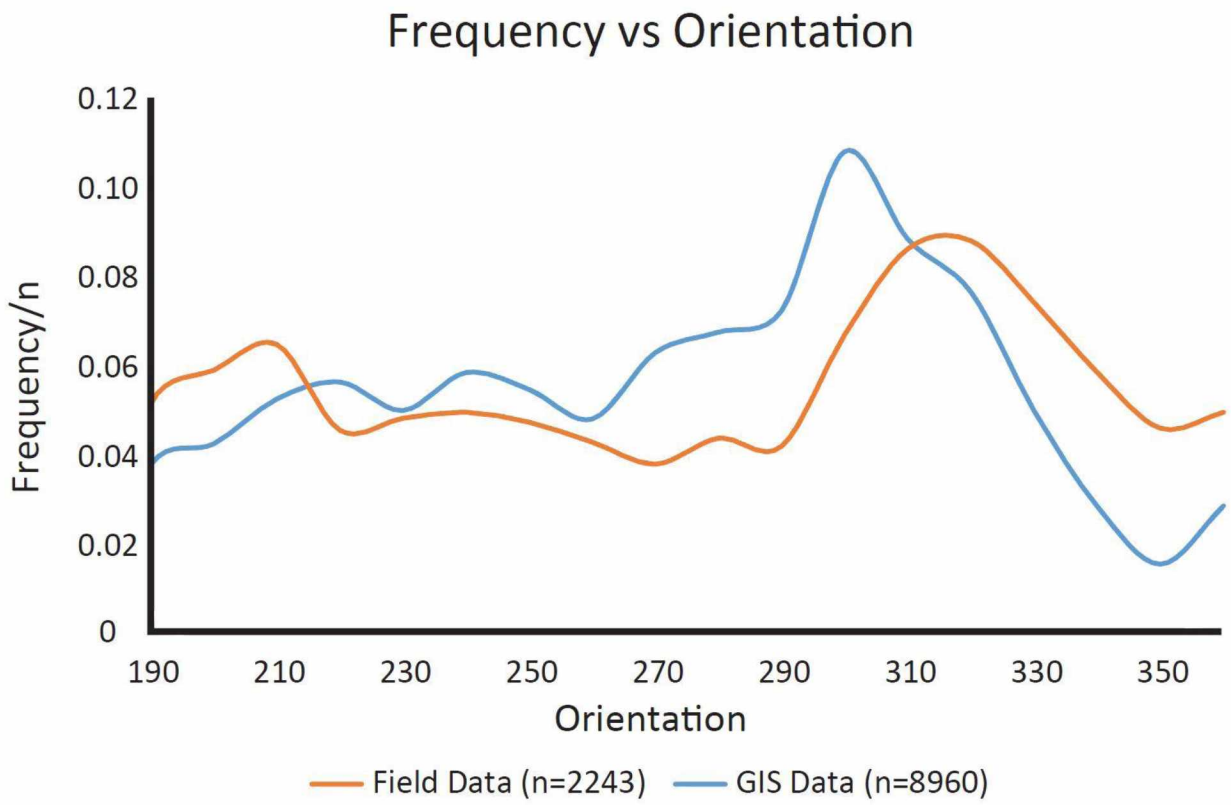

Figure 1.17 Orientations of Field vs. GIS Measurements
Frequency of fractures of a given orientation per n measurements. Orange line reflects measurements made with a Brunton compass in the field, while the blue curve reflects orientations garnered from satellite images. Note very similar profiles establishing the idea that the deformation reflected in the field area could reflect deformation for the majority of the Cook Inlet forearc basin margin and establishes the possibility that these observed fractures are regional features. Because lineaments drawn on satellite imagery do not account for bedding, or stratigraphic interval, the entire field data set was used (n=2243)

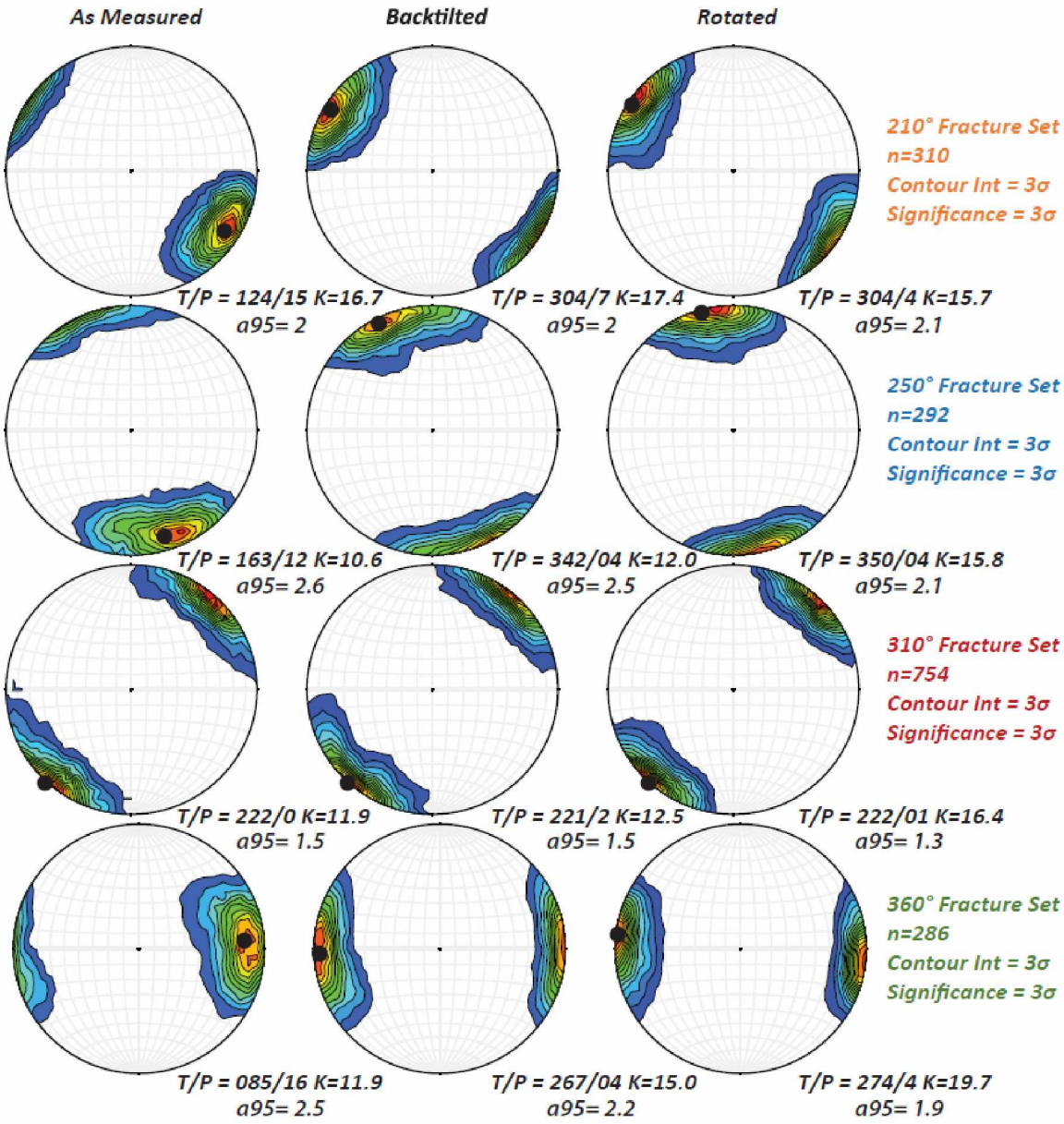
As Measured
Backtilted
Rotated
210° Fracture Set
n=310
Contour Int = 3σ
Significance = 3σ
T/P = 124/15 K=16.7
a95= 2
T/P = 304/7 K=17.4
a95= 2
T/P = 304/4 K=15.7
a95= 2.1
250° Fracture Set
n=292
Contour Int = 3σ
Significance = 3σ
T/P = 163/12 K=10.6
a95= 2.6
T/P = 342/04 K=12.0
a95= 2.5
T/P = 350/04 K=15.8
a95= 2.1
310° Fracture Set
n=754
Contour Int = 3σ
Significance = 3σ
T/P = 222/0 K=11.9
a95= 1.5
T/P = 221/2 K=12.5
a95= 1.5
T/P = 222/01 K=16.4
a95= 1.3
360° Fracture Set
n=286
Contour Int = 3σ
Significance = 3σ
T/P = 085/16 K=11.9
a95= 2.5
T/P = 267/04 K=15.0
a95= 2.2
T/P = 274/4 K=19.7
a95= 1.9

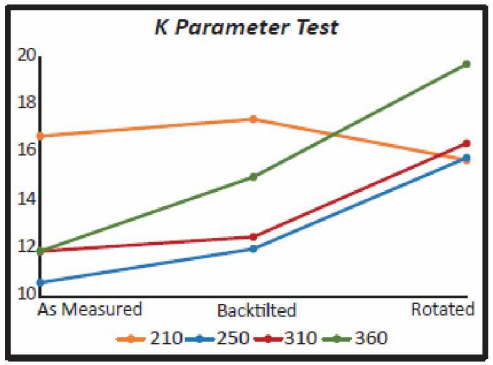
K Parameter Test
20
18
16
14
12
10
As Measured
Backtilted
Rotated
210
250
310
360

Figure 1.18 K-Parameter Test with Contoured Poles to Planes for Each Set
Pole-to-plane clusters for the four fracture sets at the three stages of restoration. Note tighter clustering for all three sets after restoring bedding to horizontal in the middle stereonets. Note tighter clustering for the 310°, 250°, and 360° fracture sets after vertical axis rotation in the right column of stereonets. A higher K value represents less dispersion. K-Parameter test at right shows decreased dispersion through unfolding and rotations for the 310°, 250°, and 360° fracture sets while the 210° fracture set shows increased dispersion after rotation. T/P – Trend and Plunge of Fischer mean vector, with K parameter, and a95 95% confidence interval. Total n value of 1642 (1642/2043) reflects the elimination of fractures that did not conform clearly to the defined fracture sets and were grouped as "noise". Within the "noise" no clearly defined fracture sets were identified. Typically, "noise fractures" had extremely variable dips, and orientations.

Geochronology

The phenocryst-free whole rock separate from the basaltic dike that intrudes a 310˚ fracture at station **JR006** yields a preferred plateau age of **52 ± 1 Ma.** Based on the isochron regression to initial $^{40}Ar/^{36}Ar$, there is no evidence this sample had any significant inherited ^{40}Ar. The integrated age of 51.7 ± 0.7 Ma is within 1σ error of the plateau age (52.0 ± 0.9 Ma) and the isochron age (49.1 ± 1.6 ma). The large error in the isochron age (figure 19) results from significantly lower ages in the last 2 steps, likely due to high Cl/K ratios indicating fluid inclusion release (Harrison et al., 1994). The first three heating steps were not used in the isochron or the plateau age determinations, as they showed significant atmospheric contents suggesting alteration. These steps constitute less than 15% of the total gas released. Ignoring the last three steps in the plateau age yields an age of **52.6± 1.0 Ma**, and discounting the first three and last two steps in the isochron yields an age of **51.4± 3.9 Ma.** These correspond with each other and with the integrated age, indicating the dike filled a 310˚ fracture ca. **52 Ma**.

Discussion

Analysis of Results

The field data cluster into four distinct fracture sets on the basis of common orientations and opening modes (figure 1.20). GIS results establish that these fracture sets are regionally present, which I suggest indicates they arose from a regional deformational event(s) or stress field(s) (figure 1.16; 1.17).

The strike test demonstrates that the four fracture sets from the field area show positive correlation between change in fracture strike orientation and change in bedding strike with respect to locally folded and tilted strata. The slopes of the weighted linear regressions, which correlate the strike of bedding with the strike of fractures, indicates that the 360°, 250°, 310° and 210° sets were all locally rotated during regional deformation and folding. The 360° fracture set slope (0.90 ± 0.12) shows the strongest correlation with bedding strike. A slope of near 1 has been interpreted as indicating either early progressive arc slip or secondary arc rotation (Yonkee and Weil, 2010a). Either scenario implies that this fracture set predates most regional folding and tilting. Slopes are 0.73 (± 0.08), 0.69 (± 0.07), and 0.45 (± 0.09) for the 250°, 310° and 210° fracture sets, respectively. These slopes are consistent with the progressive arc slip interpretation of Yonkee and Weil (2010a). I interpret the progression in slope

averages to indicate progression in fracture formation: lower slopes indicate fractures that opened later in the progressive growth of the folds, yielding a lower correlation with bedding after strike corrections.

The K-parameter test shows that the 310°, 250°, and 360° fracture sets have decreased dispersion after unfolding and vertical-axis rotation. The 210° fracture sets have increased dispersion after vertical-axis rotation but decreased dispersion after backtilting, suggesting that these fractures were tilted but not

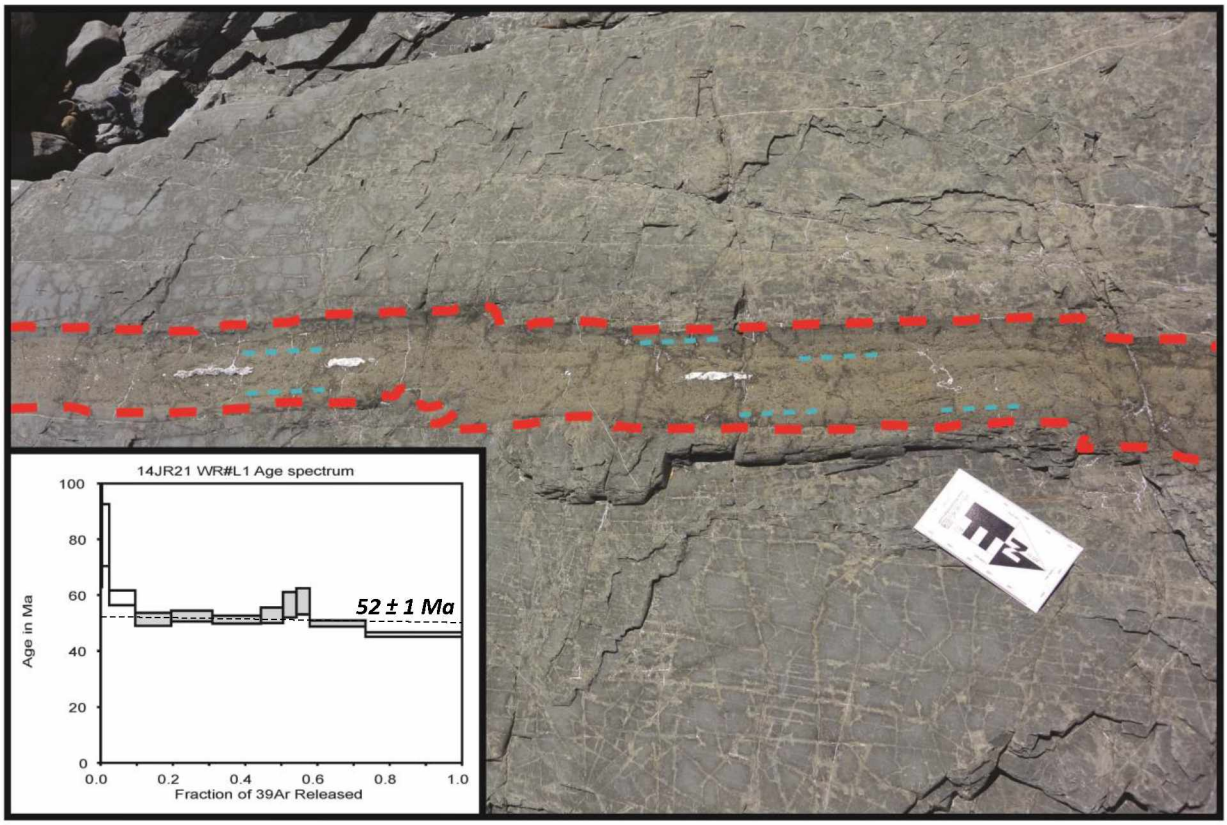

Figure 1.19 Basaltic Dike at Station JR006
$^{40}Ar/^{39}Ar$ age from a basaltic dike that intrudes a fracture of the 310° fracture set. Dashed blue lines indicate chilled margins. The inset is the plateau age.

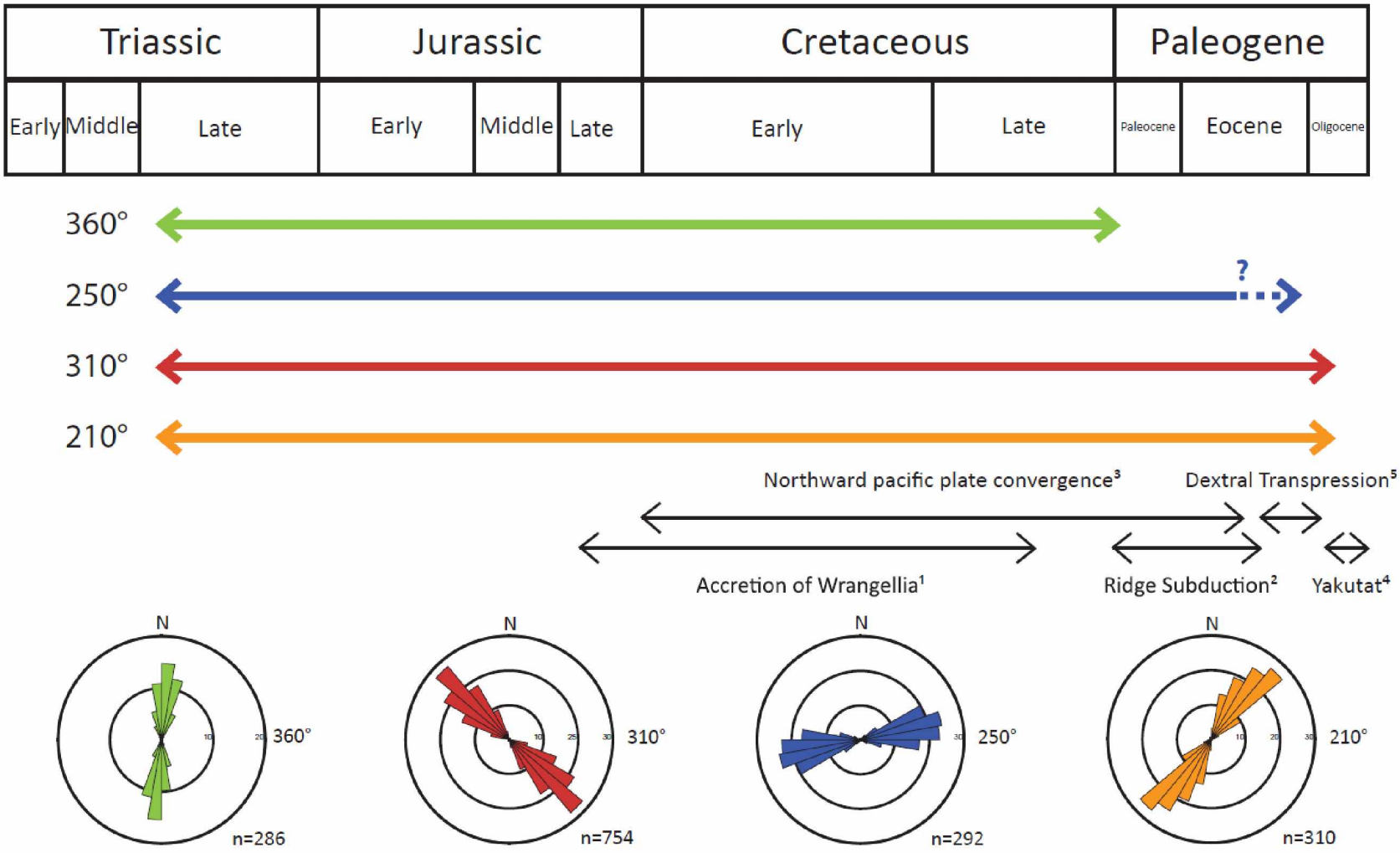

Figure 1.20 Separation of the Four Fracture Sets and their Stratigraphic Presence
Four fracture sets from the study area in strike corrected orientations to reduce spread. All rose diagrams are represented by 30% of the data set at the outer ring accept the 360° fracture set rose diagram which is represented by 20%. Color coded arrows reflect possible active ranges for the four fracture sets. Dashed where uncertain. Total n value of 1642 (1642/2043) reflects the elimination of fractures that did not conform clearly to the defined fracture sets and were grouped as "noise". Within the "noise" no clearly defined fracture sets were identified. Typically, "noise fractures" had extremely variable dips, and orientations.

rotated significantly. This lack of significant change in dispersion of the 210° fracture set suggests that this fracture set did not experience significant vertical-axis rotation, which is also consistent with the low slope from the strike test.

The K-parameter test demonstrates that all four fracture sets formed before tilting because the sets all cluster better after unfolding. Three sets likely formed in the early stages of regional deformation before or at the initiation of folding (the 310°, 250°, and 360° sets) because these three sets show strong correlations between the strike of bedding and the strike of fractures (figure 1.15, 1.18). The 210˚ fracture set likely opened during the culmination of folding because it shows the weakest correlation between strike of bedding and strike of fractures and shows a decrease in clustering after strike restoration (figure 1.15, 1.18).

Summary of Age Constraints on Fracture Development

The age for the youngest unit in the study area (previously mapped as West Foreland Formation by Fisher and Magoon, 1978) is uncertain. 150 km north of the study area, potentially correlative units range in age from ~47 to ~38 Ma (Gillis et al., 2016). Oligo-Miocene fossils were found at one study area location with fractures nearby belonging to the 310° and 210° fracture sets (JR066) (Wolfe et al., 1966; Kirschner and Lyon, 1973) (figure 1.7). Thus, I infer that fractures from the 310° and 210° sets formed younger than Oligo-Miocene age. The strike and dip of bedding is nearly the same in Cenozoic Oligo-Miocene strata as in Mesozoic Naknek Formation, suggesting that tilting and rotation occurred in the same deformational event (table 1.1).

Cross cutting relationships do not clearly indicate relative ages of fractures. I interpret this as supporting my interpretation of progressive deformation, during which preexisting fractures were sheared (figure 1.9) as the result of reactivation. Conjugate fractures of the 310° and 360° sets are common (figure 1.8; 1.10; and 1.11). I interpret this conjugate angular relationship as reflecting SSE shortening, consistent with interpretations from Betka and Gillis (2014a; 2014b). The basalt dike that intrudes a 310° fracture shows significant zoning, which I interpret as multiple pulses of intrusion. This dike yields an age of ca. 52 Ma (figure 1.20), suggesting the 310˚ fracture set was active during Eocene time. The 250° and 210° fracture sets cross cut this dike, suggesting they were active after Eocene time. Given this general chronology, I developed the following model to depict my proposed relative chronologic development of the fracture sets (figure 1.21).

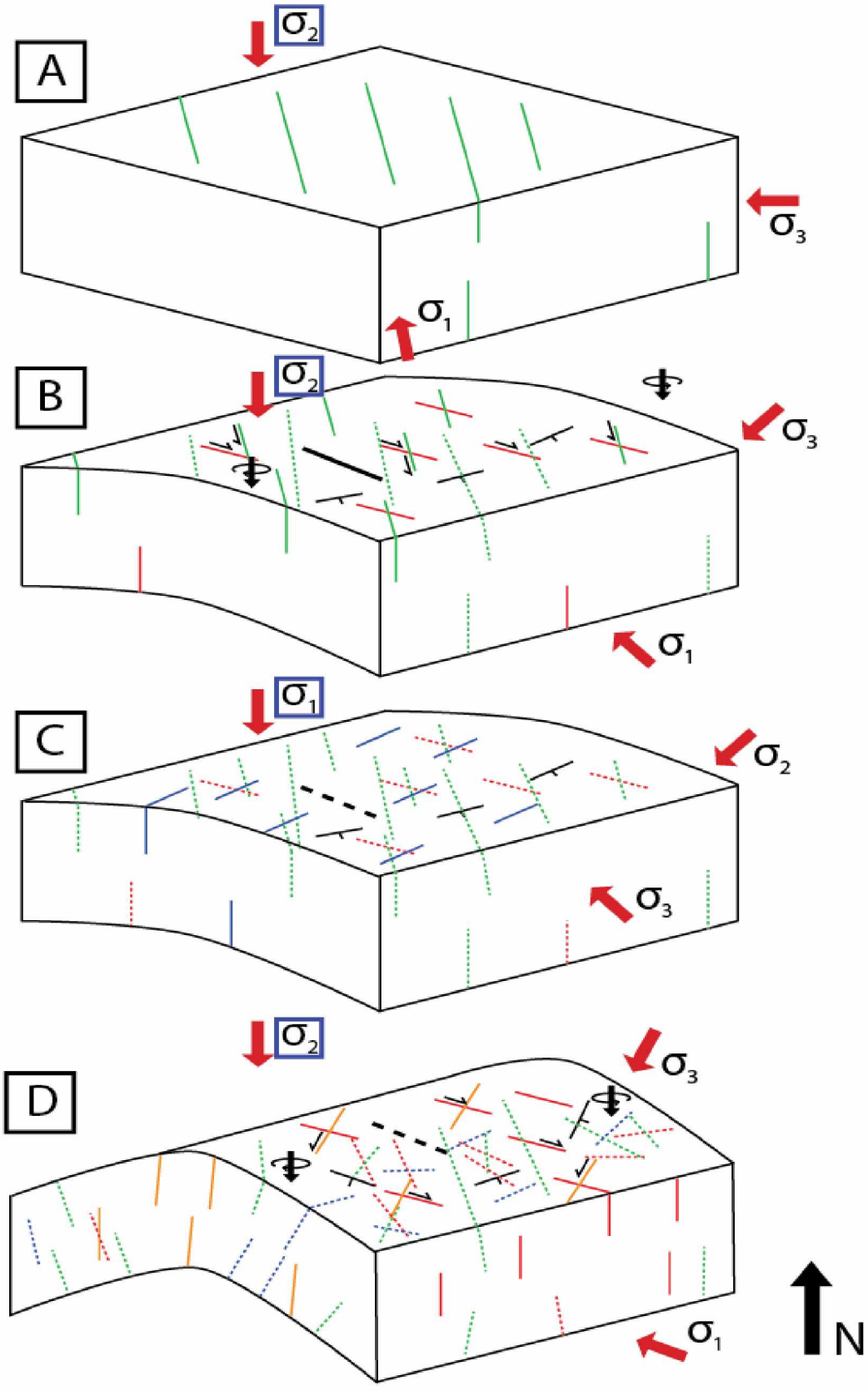
A
σ2
σ3
σ1
B
σ2
σ3
σ1
C
σ1
σ2
σ3
D
σ2
σ3
σ1
N

Figure 1.21 Block diagram interpretation of fracture development during folding
Fractures are color coded as follows (red = 310°, green = 360°, blue = 250°, orange = 210°). Thick black line represents igneous intrusive dike. Dotted lines indicate previously opened fractures or emplaced dike. sigma 1 represents principal compressive stress, sigma 2 represents intermediate compressional stress, and sigma 3 represents minimum compressive stress. Stress outline with blue box represents vertical stress. Vertical black arrows with spiral represent possible local vertical axis rotation of bedding. See figure 1.22 for tectonic associations as the letter designations (A,B,C,D) correspond.. A) Opening of the first 360° fractures. B) Opening of the 310° and 360° conjugate pair. Likely emplacement of the dated intrusive igneous dike. Possible early folding. C) Opening of the 250° fracture set during removal of compressive stress responsible for early folding. D) Folding of all strata, opening of more 310° fractures and initiation of opening of the 210° fracture set.

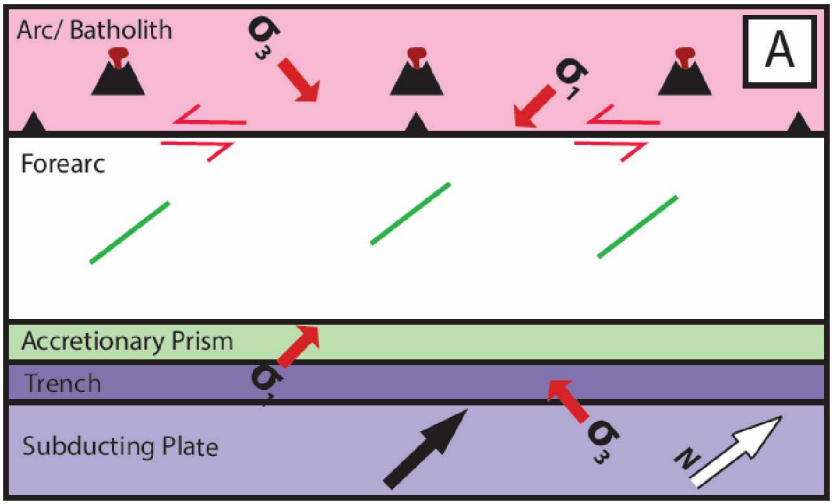
Arc/ Batholith
σ3
σ1
A
Forearc
Accretionary Prism
Trench
σ1
Subducting Plate
σ3
N

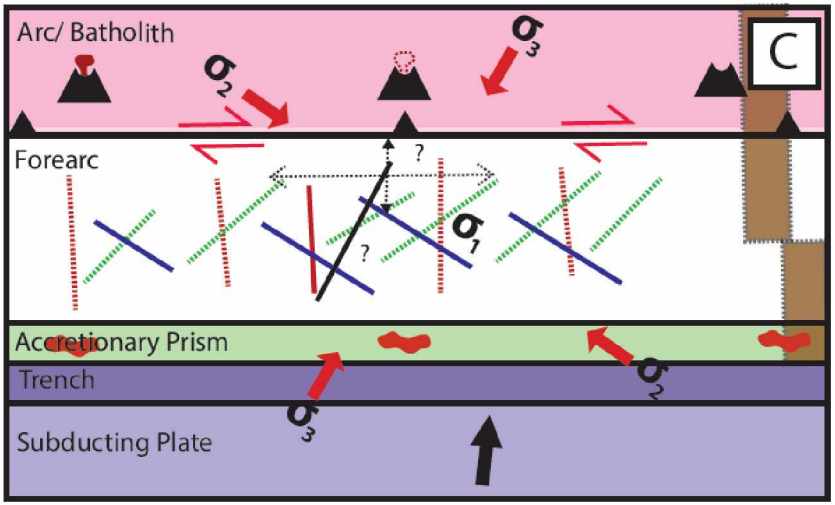
Arc/ Batholith
σ2
σ3
C
Forearc
?
?
σ1
Accretionary Prism
Trench
σ3
σ2
Subducting Plate

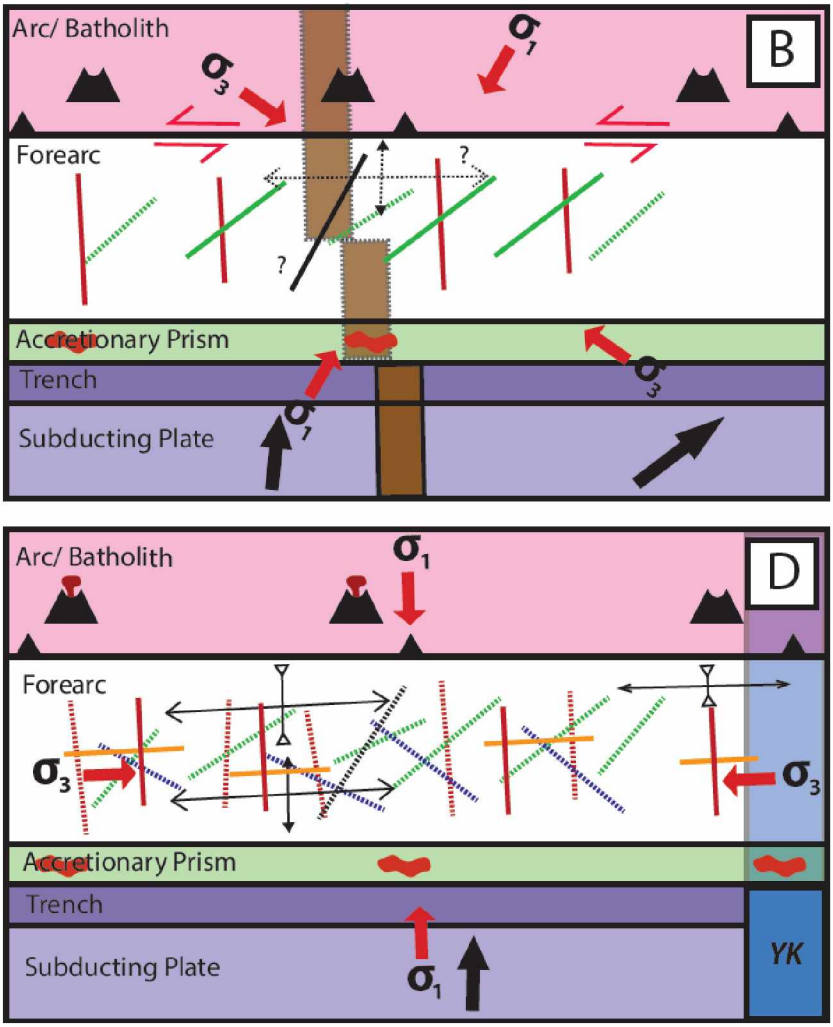
Arc/ Batholith
σ3
σ1
B
Forearc
?
?
Accretionary Prism
Trench
σ1
σ3
Subducting Plate
Arc/ Batholith
σ1
D
Forearc
σ3
σ3
Accretionary Prism
Trench
Subducting Plate
σ1
YK

Figure 1.22 Tectonic Interpretation of Fracture Acquisition
Fracture sets are color coded to the corresponding fracture sets in the text. Dotted fractures represent inactive or older fractures. Note small angular rotations of each fracture during the deformation process indicating small scale local rotations of fractures. Solid black line represents emplacement of the sampled igneous intrusive rock with "?" for uncertain emplacement age. Dotted black line means inactive dike emplacement. Volcano symbols with red plume indicate active arc activity. Dotted plums indicate resumption of arc activity. No plume indicates inactive arc. Brown represents the Kula- Resurrection ridge. Lighter brown represents subducted ridge. Blue with "YK" indicates Yakutat terrane. Transparent blue represents subducted Yakutat Terrane. Dotted anticline/syncline symbols represent speculative folding. Black Arrows represent convergence direction of depicted oceanic crust. White arrow is north arrow. Red oblong shapes in accretionary prism represent near trench intrusive plutons. Sigma 1 is inferred principal compressive stress. Sigma 3 is inferred minimal compressive stress. Sigma 2 is assumed to be vertical except where noted in C. Red arrows indicate inferred slip on the Bruin Bay Fault under the indicated stress regime. Older fractures could be active at any subsequent stress state. A) Northward convergent subduction initiates opening of the 360° fracture set in late Cretaceous time. Possibility for sinistral slip on the Bruin Bay Fault. Arc is active. B) Spreading ridge subduction in Paleocene - Eocene time results in arc extinction, and opening of the 310° and 360° conjugate fracture pair. Possibility for sinistral transpression on the Bruin Bay Fault. C) 250° fracture set initiates as extension occurs in the forearc. Possible mechanisms are initiation of arc activity from slab roll back post ridge subduction, or removal of compressive stresses from ridge subduction. Possible switches in sigma 1 and 2 could lead to E-W shortening and the opening of the 310° 250° conjugate pair. Possibility for dextral slip on the Bruin Bay Fault. D) Latest deformation opens the 210° fracture set during folding and last members of the 310° fracture set as a result of either SE-NW convergence of the Pacific Plate or initiation of the Yakutat Collision. Folding was active at this time, likely rotating all three older fracture sets locally, and tilting all stratigraphic units.

Summary of Proposed Fracture Development

360° fracture set

This fracture set is likely the oldest in the field area. It is absent from strata younger than Cretaceous (last seen in the Maastrichtian Saddle Mountain succession) (figure 1.7). This suggests that this fracture set formed after Maastrichtian time, but before Oligo-Miocene (?) time, as evidenced by its absence in Oligo-Miocene strata. The strike test for this fracture set demonstrates the strongest correlation between strike of bedding and deviation from a reference strike. Thus it is likely this fracture set experienced the most local vertical-axis rotation. The K-parameter test indicates that this fracture set shows the greatest decrease in data dispersion after strike correcting, again suggesting it arose before rotation (figure 1.15; 1.18). While figures 8, 10, and 11 document a conjugate relationship between the 310° and 360° fracture sets, I still interpret *some* of the 360° fractures to be older. Fracturing is a multi-stage process, and thus, it is possible for fractures of a given set to open throughout deformation (Hancock, 1985; Branellec et al., 2015).

250° fracture set

This fracture set is measured in strata ranging from Jurassic to Oligo-Miocene (?). While composite abutting relationships indicate that this fracture set is one of the oldest, its presence in Oligo-Miocene strata indicates it was among the youngest active (figure 1.7; 1.9; 1.20). Its strike test slope of 0.73 (± 0.08) indicates that this fracture set likely formed during or after the onset of regional deformation, likely after the 360° fracture set as indicated by its slightly lower slope. This fracture set, too, occasionally forms conjugates with the 310° fracture set, suggesting a genetic relationship (figure 1.10c). The K-parameter test for this fracture set shows a slightly lower decrease in dispersion than the 360° fracture set, again suggesting that this fracture set developed later. Its dispersion clearly decreases after back tilting, however, suggesting that this fracture set also formed early in the folding and tilting process.

The strike test slope of 0.73 (± 0.08) indicates that this fracture set likely formed progressively during regional deformation, and its similar slope to the 310° fracture set (0.69; discussed below) indicates that they are of similar age. The 250˚ fracture set also occasionally forms conjugate pairs with the 310° fracture set (figure 1.10c), suggesting a strong overlap or similar genesis for the 310˚ and 250˚ sets.

310° fracture set

This fracture set is present in Jurassic to Oligo-Miocene (?) aged strata. It is one of the youngest fracture sets as evidenced by its presence in younger strata and its prominence throughout the field area (53/56 stations). However, this fracture set appears to have formed conjugate pairs at some stations with both the 360° and 250° fracture sets (figure 1.10), suggesting that it has been forming for a significant period of time (ranging from latest Cretaceous to Miocene), and shares a genetic relationship with both of these sets. The shortening directions for conjugate pairs of the 310° with the 360° and 250° fracture sets would suggest SSE and E-W shortening respectively. These shortening directions are consistent with previously studied fault kinematics in the region (Betka and Gillis, 2014a; 2014b).

As indicated by the strike test, the 310° fracture set appears to have been subject to lesser vertical axis rotation during folding than the 360° and 250° fracture sets (0.69 ± 0.07 vs 0.73 ± 0.08 and 0.90 ± 0.12). In the K-parameter test, dispersion of the 310° set decreases after vertical-axis rotation, again suggesting these fractures were folded and rotated. Because this fracture set appears to form conjugates with both the 360° and 250° sets, it has likely had multiple openings, and has been active for a prolonged period of time. A dated dike that intrudes a 310˚ fracture suggests that the fracture set was active by 52 Ma, with multiple chilled margins in the dike further indicating protracted opening of the 310˚ set (see Delaney et al., 1986 for discussion of dikes and brittle deformation) (figure 1.19). Fracture stratigraphy (figure 1.7) further suggests that this set was active until at least Miocene time. Thus the formation of fractures in the 310° set has likely persisted throughout the growth of folds and development of all other sets.

210° Fracture set

The 210° fracture set is present in Jurassic to Oligocene aged strata, and cross cuts the 52 Ma dike. The K-parameter test indicates that this fracture set is more dispersed after strike correction, but less dispersed after back tilting. The small changes in dispersion suggest that this fracture set formed latest during the folding process. This suggests that this fracture set is likely related to folding, and likely opened late during the folding and tilting process. The strike test results indicate that this fracture set has the lowest correlation with the strike of bedding of all the fracture sets (0.45 ± 0.09 versus 0.69 ± 0.07, 0.73 ± .08, and 0.90 ± 0.12), again suggesting it formed later than the other sets. Its presence in Miocene strata (figure 1.7) further supports the interpretation that the 210˚ set is one of the youngest fracture sets. I interpret these fractures as having formed in the latest stages of folding in response to flexure in the limbs of folds.

Fracture Development in a Tectonic Context

Modeling and field-based measurements of fractures have been used by numerous authors to interpret the timing and orientations of fractures within folded and tilted strata. Conceptual models predict that four fracture sets will occur during folding: a tensile set perpendicular to the fold axis, a conjugate set that shares the same shortening direction as the first tensile set, and a final tensile set that opens parallel to the fold axis as a result of flexure in the outer layers (e.g., Price, 1966; Friedman, 1969; Hancock, 1985). However, such models cannot account for the orientations or opening modes of all fracture sets measured in the field (e.g., Bergbauer and Pollard, 2004; Bellahsen et al., 2006; Amrouch et al., 2010; Lacombe et al., 2011; Branellec et al., 2015). More recent field-based interpretations suggest that most fractures in folded strata originate during burial or layer-parallel shortening before folding commences (e.g., Ahmadhadi et al., 2008; Branellec et al., 2015). Essentially, fractures that predate folding create significant discontinuities that propagate during continued deformation while inhibiting development of new fractures (Bergbauer and Pollard, 2004). Thus, fractures record progressive deformation, and tectonic events and regional deformation will reactivate and proliferate old fractures in the process of creating new ones.

In the field area presented here, several important tectonic events that affected southern Alaska could have influenced regional brittle deformation in the Cook Inlet. These seven events are: 1) The accretion of the Wrangellia Composite Terrane with the southern margin of Alaska ending in latest Cretaceous time (Wallace and Engebretson, 1984; Plafker et al., 1989; Moll-Stalcup, 1994; Nokleberg et al., 2001; Trop and Ridgway, 2007); 2) Cretaceous subduction of a spreading ridge (Pavlis and Roeske, 2007); 3) The subduction of the Kula – Resurrection spreading ridge from 61 - 50 Ma (Bradley et al., 2003; Haeussler et al., 2003); 4) The subduction of the younger more buoyant Resurrection plate prior to the arrival of the Kula-Ressurrection ridge (Haeussler et al., 2003) 5) The convergence direction change of the Pacific plate ca. 42 Ma (Engebretson et al., 1985; Lonsdale, 1988; Doubrovine and Tarduno, 2008); 6) Paleocene oroclinal bending (Coe et al., 1985; Glen, 2004); and 7) The arrival of the Yakutat microplate and its subsequent subduction as early as 40 Ma (Finzel et al., 2011; 2015; 2016) or as late as 24 Ma (Plafker, 1987; Eberhart-Phillips et al., 2006; Benowitz et al., 2014).

Triassic – Maastrichtian

Composed of a series of amalgamated terranes, Alaska was in a state of assembly for much of the Mesozoic (Nokleberg et al., 1994; Plafker and Berg, 1994; Trop and Ridgway, 2007). The Wrangellia composite terrane collided with the North American margin during latest Jurassic–Early Cretaceous time

(Trop and Ridgway, 2007). Suturing of the Wrangellia composite terrane to southern Alaska was complete by latest Cretaceous (80–60 Ma) as shown by late Cretaceous continental margin arc rocks that stitch the accreted terranes with the former continental margin (Plafker et al., 1989; Moll-Stalcup, 1994, Trop and Ridgway, 2007).

Throughout Jurassic time, forearc sediments record the creation, erosion, and exposure of the roots of the Talkeetna arc which was either accreting on to the margin or was built upon the margin of the Wrangellia composite terrane. In the field area, the Naknek Formation records the exposure of the Talkeetna arc roots (Wartes et al., 2013; Herriot et al., 2016). A significant unconformity separates these Oxfordian strata from the Maastrichtian Saddle Mountain formation (figure 1.2) (Magoon et al., 1980; Detterman and Hartsock, 1966). In the study area the unconformity is likely older than Maastrichtian (on the basis of the Saddle Mountain succession appearing after the unconformity) but younger than Neocomian on the basis of foraminifera, nanoplankton, and palynomorphs in strata that precede the unconformity (Magoon, 1986). The cause of this unconformity is uncertain, however rapid low angle subduction of oceanic crust and wide spread regional dextral transpression have been proposed mechanisms (Plafker and Berg, 1994; Roeske et al., 2003; Trop and Ridgway, 2007) as well as the subduction of a Cretaceous ridge (Pavlis and Roeske, 2007). The deformation associated with the subduction of a Cretaceous ridge is poorly understood, and further work in the much thicker, better preserved Cretaceous section south of the Iniskin Peninsula could shed more light on the regions deformational history during the Cretaceous.

The 360° fracture set does not occur in any strata younger than the Maastrichtian (figure 1.8, 1.20). Thus, the two oldest tectonic events that could deform Maastrichtian rocks in the forearc but not Oligo-Miocene rocks are Kula–Resurrection ridge subduction (Haeussler et al., 2003; Bradley et al., 2000; Bradley et al., 2003) and northward convergence of the Resurrection Plate before the arrival of the actively spreading Kula–Resurrection ridge (Haeussler et al., 2003). Differentiating between the two without well-constrained ages of fracturing is difficult, and either event involves young, buoyant crust that resists subduction and induces shear stress between the subducting crust and overriding plate, which could manifest in shortening and deformation in the upper crust (e.g., Cloos, 1993). Northward convergence of the Resurrection plate would have created a principal shortening direction oriented N–S, which could create tensile mode one fractures oriented at 360° (figure 1.21a; 22a). Oblique convergence of the Kula-Resurrection ridge could also have created early members of the 360° fracture set. A third but not favored possibility is that oroclinal bending could have deformed the forearc during this time

(e.g., Coe et al., 1985; Glen, 2004). Formation and bending of the southern Alaska orocline is thought to have resulted in shortening that could have been accommodated by basin bounding thrust faults and regional fracture systems. Oroclinal bending would imply that all fractures after bending would have been rotated roughly 40°, however, I do not see evidence of systemic regional 40° rotations in the observed fracture populations. A more thorough regional field sampling of fracture character, and perhaps paleomagnetic signatures, would be necessary to further investigate the oroclinal bending hypothesis in this region (see Yonkee and Weil, 2010a; 2010b). In conclusion, I prefer the interpretation where the opening of the 360° fracture set is the result of either early ridge subduction, or northward convergence of the Resurrection plate.

Paleocene - Eocene

Following the opening of the 360° fracture set, the arrival and subduction of the Kula-Resurrection spreading ridge was the likely driver for a significant portion of the pre-Oligocene (Paleogene) deformation observed in the Cook Inlet (Bruhn and Haeussler, 2006). Evidence of Kula-Resurrection ridge subduction in Alaska is recorded in the form of near-trench intrusive plutons first at Sanak Island in southwest Alaska ca. 61 Ma and last at Baranof Island in southeast Alaska ca. 49 Ma (Bradley et al., 2003; Haeussler et al., 2003). The ridge would have been obliquely subducted beneath the Cook Inlet forearc from ca. 57–54 Ma (Bradley et al., 2000; Bradley et al., 2003). While U-Pb ages of the near-trench intrusives from Bradley et al. (2003) suggest that the Kula-Resurrection ridge was passing beneath modern-day Yakutat by 54 Ma, Ar/Ar ages are consistently younger, closer to 53 Ma on the Kenai Peninsula (see Bradley et al. (2003), figure 4). In the Cook Inlet study area, this matches the whole-rock 52.0 ± 0.7 Ma Ar/Ar age from a basalt dike intruding a fracture of the 310° set (figure 1.19). The dike age shows similar cooling ages to biotite and hornblende phenocryst cooling ages in near trench intrusive plutons opposite our study area in the accretionary prism. Furthermore, this dike could be related to other tertiary dikes reported to the north of the study area that have been previously tied to ridge subduction (e.g., Madsen et al., 2006; Benowitz et al., 2012). This suggests a possible connection between tectonic processes acting in the accretionary prism or margin of southern Alaska, and the forearc basin.

While the complete deformation mechanisms for aseismic and actively spreading ridges will be different, I make the assumption that since both aseismic and actively spreading ridges represent significant topographic highs, the brittle deformation in the forearc associated with the collision of actively spreading ridges will be at least as great as asesismic ridges. Active spreading centers will likely

exhibit stronger deformation signatures, because the crust being subducted is younger, more buoyant, and thus more likely to resist subduction.

Where the aseismic Cocos Ridge is being subducted off the coast of Costa Rica, structural evidence of Neogene deformation is widespread; including 20 km long fault strands with up to 2500 meters of throw, macroscopic 5 – 10 km subhorizontal margin parallel folds, and mesoscopic conjugate fractures recording shortening normal to the Central American margin (Corrigan et al., 1990). These patterns of deformation are similar to patterns seen in the southern Cook Inlet. Thus it is possible that margin-normal shortening, the opening of the 310° and 360° conjugate fractures, sinistral transpressional slip on the Bruin Bay Fault, and folding of Mesozoic strata could have resulted from the subduction of a spreading ridge underneath the southern Alaska margin (Detterman and Hartsock, 1966; Betka and Gillis, 2014a; 2014b; 2015; 2016). Given that the Kula-Resurrection ridge was spreading, it would be associated with hotter, more buoyant lithosphere that is more resistant to subduction, and therefore likely to cause increased strain in the upper crust relative to an aseismic ridge. Additionally, sand box experiments focusing on the subduction of a topographic high seem to indicate similar patterns of brittle deformation observed in the Cook Inlet (Dominguez et al., 1998).

Since it is possible for a range of shortening directions to result from the subduction of an active ridge due to different plate vectors between the two subducting slabs (Yamakazi and Yukinobu, 1989; Cloos, 1993; Dominguez et al., 1998; Laursen et al., 2002; Zeumann and Hampel, 2015), SE oriented shortening is well within the realm of possibility of the presumably obliquely subducting Kula-Resurrection ridge. Given the presumed actively spreading nature of the Kula – Resurrection spreading center, and the possible obliquity of its subduction (Sisson and Pavlis, 1993; Pavlis and Sisson, 2003; Haeussler et al., 2003), SSE shortening and the creation of the widespread 310° - 360° conjugate fracture system are reasonable outcomes from the subduction of the Kula – Resurrection spreading ridge. The absence of the 360° fracture set in rocks younger than the tectonic event supports the model for a separate tectonic event, however, it's possible that the absence of this fracture set is due to a sampling bias of only visiting a few stations. Our interpretation that this fracture set is older could be strengthened by visiting more stations in Oligo-Miocene aged strata, and measuring more fracture sets. If the 360° fracture set were ultimately documented in Oligo-Miocene and younger aged strata, then it would suggest that the majority of the deformation in question is related to post Oligo-Miocene tectonic events.

I therefore call on Kula-Resurrection ridge subduction as the tectonic driver of SSE oriented shortening and the creation of the 310° and 360° conjugate fracture pair (which fracture rocks from Hettangian to Mastrichtian age). This event was probably a significant driver of slip on the Bruin Bay Fault, and likely initiated some folding in the lower Cook Inlet. The 52 Ma ± 0.7 basalt dike that intrudes a fracture of the 310° fracture set was possibly the result of subduction of young hot lithosphere beneath the forearc, although, its slightly younger age could suggest a slightly different mechanism for emplacement. The shortening direction inferred from the 310° and 360° conjugate pair coincides well with documented SSE shortening and sinistral slip on the nearby Bruin Bay Fault (Detterman and Hartsock, 1966; Betka and Gillis, 2014; 2015; 2016) (figure 1.21b; 22b). I interpret that *some* folding of the stratigraphic section was likely initiated during this event, but recognize that in some locations in the field area, Mesozoic and Cenozoic strata are tilted uniformly (Gillis et al., 2016), which suggests that folding and tilting occurred after this event.

Eocene – Oligo-Miocene

A driver for E-W oriented shortening (and thus, a driver for the opening of the 250° fracture set) could be a switching of principal shortening directions after the subduction of the Kula – Resurrection ridge (figure 1.22c). One recent model demonstrates after a ridge reaches a sufficient depth beneath the continental margin during subduction, the compressional stresses are dampened or removed (e.g., Dominguez et al., 1998; Zeumann and Hampel, 2015). This new lack of compression reverses the stress regime from contractional to extensional within the forearc (Zeumann and Hampel, 2015), and thus reverses the dominant shortening direction simply by removing compressional stresses. An additional possible mechanism for the opening of this fracture set is the local change in bending stresses during the progressive growth of folds. We prefer the prior interpretation, as we find these fractures in strata that were not significantly folded, and these fractures are slightly oblique to the regional fold axis.

Therefore, a mechanism for WSW shortening could simply be the removal of SSE compressional stress from the arrival of the Kula-Resurrection Ridge. This could initiate the opening of the 250° fracture set. WSW shortening could have also created the infrequent conjugate pairs observed between 310° and 250° fractures while also simply opening tensile fractures oriented roughly 260° (figure 1.21c; 1.22c).

Oligo-Miocene – Present

It must be noted again, that the age constraints for the Oligo-Miocene strata are questionable. However, for the purposes of this thesis and our interpretations, neither the age of this unit nor the formation name are spectacularly important; so long as the unit postdates the arrival of the Kula –

Resurrection ridge (which either the Eocene or Oligo-Miocene age would seem to support). I will not speculate on the formation name call, as it is not relevant to this discussion. If these rocks prove to be older than Oligo-Miocene or Eocene (ca. 52 Ma), the interpretations of this manuscript would suggest that all of the observed brittle deformation in the lower Cook Inlet was related to the subduction the Kula – Resurrection ridge; as the 310° and 210° fracture sets occur in strata that would be older than the tectonic event in question. This would imply that conjugate fracture formation, folding, tilting, and all other associated brittle deformation in the region reached its climax of activity during the arrival of the Kula – Resurrection ridge. If the rocks prove to be younger than ca. 52 Ma, then the following interpretations will remain the same given the data presented.

Oligo-Miocene strata host members of the 310° and 210° fracture sets. These are the youngest strata sampled, and therefore fractures the strata host represent the youngest deformational event. Thus, it is important to understand potential drivers for deformation of this unit.

It's likely that the Oligo-Miocene strata was initially deposited in the forearc after the passing of the ridge during Eocene time (e.g., Trop and Ridgway, 2007; Lepain et al., 2013; Gillis et al., 2016). Thus any fracture sets present in the lower Cenozoic strata had to be active after Oligo-Miocene time. Furthermore, because the entire stratigraphic section spanning Mesozoic to Oligo-Miocene (?) time is tilted, and in some locations tilted uniformly (Gillis et al., 2016), it's likely that significant folding and tilting likely happened after Oligo-Miocene time.

Deformation in the Oligocene was possibly driven by the 25 Ma arrival of the Yakutat terrane to the southeast (Plafker, 1987; Ridgway et al., 1986; Eberhart-Phillips et al., 2006; Fuis et al., 2008; Benowitz et al., 2014). Within the upper Cook Inlet, deformation related to the arrival of the Yakutat Block has manifested in a series of transpressional fault-cored anticlines and significant uplift and exposure of Cenozoic and perhaps Mesozoic forearc sedimentary rocks (Bruhn and Haeussler, 2006; Haeussler et al., 2000; Trop and Ridgway, 2007).

The anticline-syncline pair of the Iniskin Peninsula shares similar strikes to folds in other portions of the Cook Inlet that have been widely recognized as Cenozoic because they deform Cenozoic strata (e.g., Haeussler et al., 2000; Bruhn and Haeussler, 2006). I interpret that folding and tilting of strata on the Iniskin Peninsula and in Lake Clark National Park was Cenozoic, because strata of Cenozoic age are deformed to similar dip angles as underlying strata (Gillis et al., 2016; see table 1.1). The tectonic driver of young fault cored anticlines with similar strikes in the upper Cook Inlet has been widely attributed to

the arrival of Yakutat (Haeussler et al., 2000). Thus, it is possible that folding and tilting in the lower Cook Inlet is related to the arrival of Yakutat, however, a definitive signature of this event is not clear in the fracture stratigraphy. One possible issue with this interpretation is that the location of lower Cook Inlet folds are roughly 300 km to the SW, however deformation related to the subduction of Yakutat has been documented roughly 300 km to the SE of where Yakutat is actively deforming the margin of southern Alaska (Meigs et al., 2008). Furthermore, modern convergence directions of the Pacific plate and the southern Alaska margin would be consistent with SE oriented shortening which is concordant with the opening of the 310° fracture set and the opening of the 210° fracture set during folding. Thus, it is also possible that typical subduction processes led to the deformation of the exposed strata of the western Cook Inlet. Either event could plausibly create SE oriented shortening. Because forearc deformation in the upper Cook Inlet is likely driven by the ongoing collision of Yakutat, we prefer to interpret lower Cook Inlet folds as having a similar driver, though possibly slightly different mechanisms.

Folding and tilting of strata would have been created by SSE shortening for a second time, opening additional 310° fractures, shearing the 360° fracture set, offsetting the 250° fractures, and finally opening the 210° fractures (figure 1.21d; 1.22d). Furthermore, the modern stress regime for the study area confirms SSE shortening, and further favors the model that the deformation was driven by flat slab subduction of Yakutat (Ruppert, 2008).

Conclusions

This study presents an analysis of four regionally present fracture sets in the sedimentary strata of the western Cook Inlet. These four fracture sets, oriented 360°, 310°, 250° and 210°, are explained by major regional tectonic events. These four sets opened during a progressive deformation sequence spanning late Cretaceous – Oligo-Miocene Cenozoic time. The 360° set opened as a result of subduction of the Resurrection (Farallon) plate. More 360° fractures and some 310° fractures formed as a conjugate pair during ridge subduction ca. 52Ma. The 250° and 310° fracture sets proliferated during the progressive growth of the folds and are interpreted to reflect stress relaxation of the forearc region after the passage of the Kula-Resurrection ridge. Continued deformation through the Miocene formed fractures of the 310° and 210° sets in Miocene rocks. I conclude that late Cenozoic deformation in the lower CIB could reflect far field stresses from the arrival and subduction of the Yakutat terrane in southern Alaska

2. Fracture Intensity of the Mesozoic Sedimentary Forearc Strata of the Lower Cook Inlet, Alaska

Introduction[2]

Natural fractures aid the migration of basinal fluids in rocks with low primary porosity and permeability (e.g., Engelder et al., 2009; Lianbo and Xiang-Yang, 2009; Ortega et al., 2010). Thus, quantifying lithologic controls (for example, grain size) on the size and density of regionally mapped fracture sets is important for the development of tight sandstones in unconventional hydrocarbon plays. Large, open fractures (≥ 0.5 mm aperture) are especially important for fluid migration (for example, Laubach, 1997). Helmold and others (2013) demonstrated that Jurassic sandstones in lower Cook Inlet exhibit diminished primary porosity and permeability as a result of diagenesis. However, several oil shows and seeps that occur in the region are spatially associated with regional fracture networks that likely controlled the migration of hydrocarbons in the basin (Detterman and Hartsock, 1966; LePain et al., 2013; Wartes and Herriot, 2014; AOGCC, 2015). Furthermore, marine shale that comprises part of the Mesozoic section in the Cook Inlet Basin are thought to be the source rocks for Cenozoic hydrocarbon reservoirs (e.g., Magoon, 1994). Understanding which parameters correlate with fracture size and density could aid in the recovery of hydrocarbons, and thus increase the economic potential of low permeability and porosity reservoirs in Jurassic strata of Cook Inlet. Examination of the Jurassic section of the Cook Inlet will allow me to 1) evaluate the potential for fractured reservoirs in rocks that have poor reservoir potential due to diagenetic alteration (Helmold et al., 2013) and 2) quantify fracture intensity of source rocks in the CIB to evaluate the importance of secondary porosity and permeability caused by natural fractures.

Marrett and others (1999) show that fractures follow power law scaling relationships when normalized for size, with macro fractures being less abundant than micro fractures. Using size normalized cumulative frequency to measure fracture intensity, they demonstrated that fractures in a uniform rock type will follow power law scaling relationships across five orders of magnitude of fracture size with excellent correlation. Thus, by measuring micro fractures in thin section, one could estimate the densities of macro fractures at reservoir scale. Therefore, normalized fracture intensity (the number of fractures of a specified size or larger per unit length) is a useful quantity for describing the density of natural fractures in various rock types. Numerous authors have showed power law scaling relationships

[2] This Chapter will potentially be revised for submission with co-author P. Betka as a Report of Investigations through the Alaska Division of Natural Resources Division of Geological and Geophysical Surveys

occur in various rock types (quartz sandstones and limestones) (e.g., Ortega et al., 2010; Hooker et al., 2009; Gomez and Laubach, 2006; Hooker et al., 2014). I provide some of the first size normalized fracture intensity data for arkosic and lithic arenites (see also, Lianbo and Xiang-Yang, 2009), and the first data of its kind for the Cook Inlet Basin.

Quantifying macro fractures (fractures greater than 1mm) in the sub-surface has proven difficult because vertical wells commonly do not intersect many fractures (Narr, 1991) and large fractures are commonly open making complete recovery of the fracture in core difficult (Laubach, 2003). Furthermore, large fractures control the migration of basinal fluids making their characterization critical for understanding fluid flow in reservoirs (Laubach, 1997; Laubach, 2003). Because macro fracture sampling in the sub-surface is difficult, abundant micro fracture populations (fracture aperture < 1mm) have been used to provide estimates of macro fracture orientations, abundance, and size (Laubach, 1997; Marrett et al., 1999; Ortega and Marrettt, 2000; Ortega et al., 2006; Hooker et al., 2009; Hooker et al., 2014).

In this study, I quantify the fracture intensity of four regional fracture sets (defined in Chapter 1) that are hosted in deformed forearc basin strata of Jurassic age in the Iniskin–Tuxedni region of the lower Cook Inlet, Alaska (cf. Rosenthal et al., 2015a, b; figure 2.1). My results document the range of fracture intensities of the four previously outlined regional fracture sets: a 310° trending fracture set, a 210° fracture set, a 250° trending fracture set, and a 360° trending fracture set (sets A,B,C, and D respectively) (see Chapter 1). I document how fracture intensity changes by formation and with grain size. I also test the feasibility of using micro fracture intensity determined in thin sections as a proxy for estimating macro fracture intensity by comparing outcrop and thin section based scan line analyses. My results are discussed in the context of exploiting natural fractures as fluid migration pathways that could enhance sub-surface permeability for the lower Cook Inlet hydrocarbon province; and serve as hydrocarbon migration pathways in the upper Cook Inlet petroleum system.

Background

The Cook Inlet basin is a northeast-trending collisional forearc basin (Nokleberg et al., 1994) located between the Jurassic Talkeetna Arc and modern Aleutian Arc to the northwest and the Aleutian trench and Chugach accretionary prism to the southeast (figure 2.1). This study focuses on the Iniskin-Tuxedni region of Cook Inlet basin (figure 2.1). Outcrops in the study area expose ~35,000 feet of Mesozoic sedimentary strata (figure 1.2) (Detterman and Hartsock, 1966; Kirschner and Lyon, 1973). Immature

arkosic, lithic, and volcaniclastic arc-derived sandstones, siltstones, and shales comprise the Mesozoic section in the study area and reflect exhumation and denudation of the Mesozoic arc located to the northwest of the basin (e.g., Plafker et al., 1989; Nokleberg et al., 1994; Trop and Ridgway, 2007). Mesozoic clastic sedimentary rocks in this NE-trending basin record forearc subsidence and sedimentation at a convergent margin for most of Mesozoic time and include the oil source rocks for Cenozoic reservoirs of the petroliferous upper Cook Inlet petroleum system (e.g., Kirschner and Lyon, 1973; Nokleberg et al., 1994; Trop and Ridgway, 2007; Magoon, 1994; Lillis and Stanley, 2011).

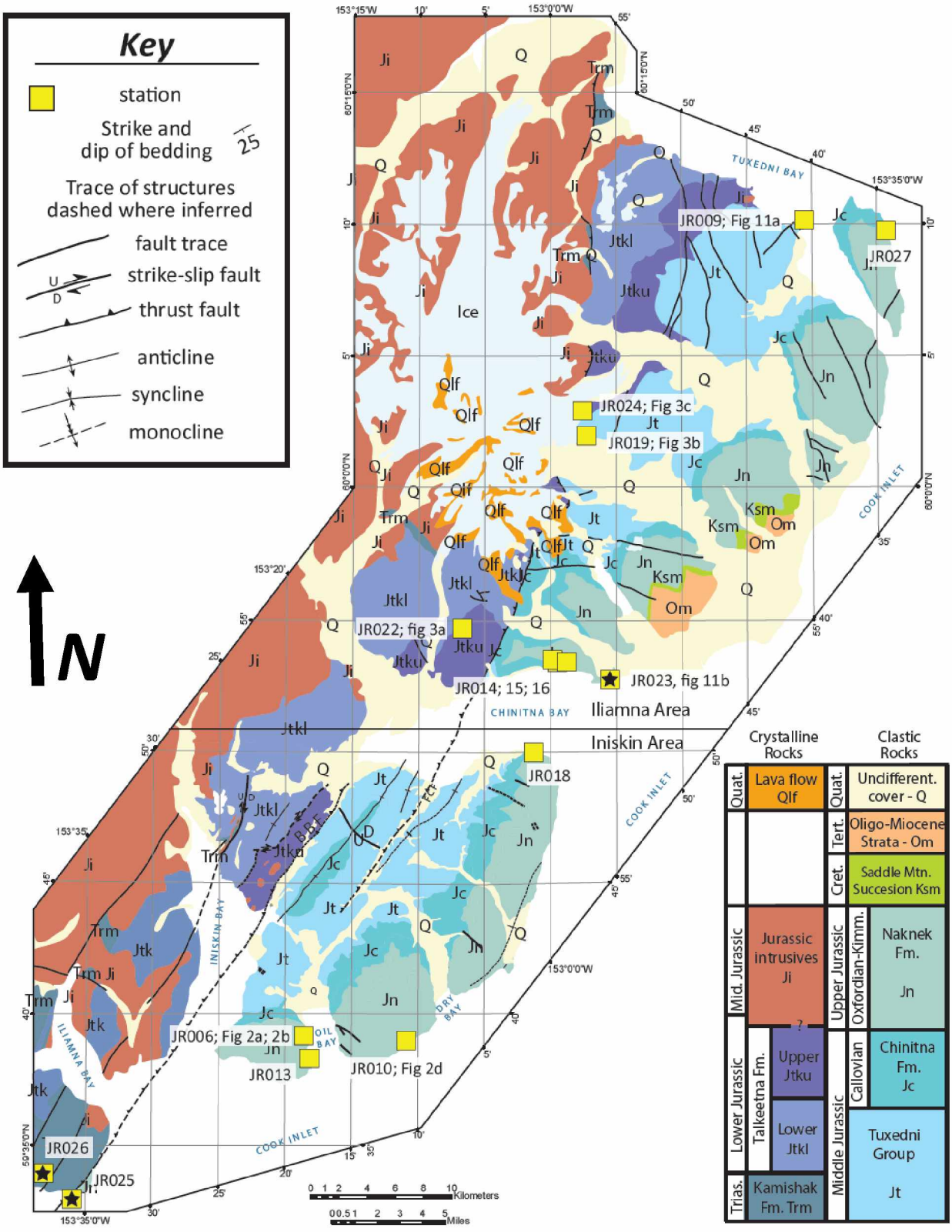
Key
station
Strike and dip of bedding
25
Trace of structures dashed where inferred
fault trace
strike-slip fault
thrust fault
anticline
syncline
monocline
N
JR009; Fig 11a
JR027
JR024; Fig 3c
JR019; Fig 3b
JR022; fig 3a
JR014; 15; 16
JR023, fig 11b
Iliamna Area
Iniskin Area
JR018
JR006; Fig 2a; 2b
JR013
JR010; Fig 2d
JR026
JR025
TUXEDNI BAY
CHINITNA BAY
COOK INLET
INISKIN BAY
ILIAMNA BAY
OIL BAY
DRY BAY
Ice
Ji
Q
Trm
Jtkl
Jtku
Jt
Jc
Jn
Ksm
Om
Qlf
Jtk
BBF
FTF
0 1 2 4 6 8 10 Kilometers
0 0.5 1 2 3 4 5 Miles
Crystalline Rocks
Clastic Rocks
Quat.
Lava flow Qlf
Undifferent. cover - Q
Tert.
Oligo-Miocene Strata - Om
Cret.
Saddle Mtn. Succesion Ksm
Mid. Jurassic
Jurassic intrusives Ji
Upper Jurassic
Oxfordian-Kimm.
Naknek Fm. Jn
Lower Jurassic
Talkeetna Fm.
Upper Jtku
Callovian
Chinitna Fm. Jc
Lower Jtkl
Middle Jurassic
Tuxedni Group Jt
Trias.
Kamishak Fm. Trm

Figure 2.1 Simplıfied Geologic Map of the Study Area with Stations
Simplıfied geologic map of the study area with stations where I measured fracture intensity (yellow squares) Modıfied from Betka and Gillis (2015). Domains separated by thin black line that transects Chinitna Bay. Figure references and station names are shown spatially next to their corresponding yellow square. Black stars denote locations of black stars in fig. 2.12

Conventional reservoir potential of the Mesozoic strata is poor because their primary porosity has been reduced by diagenetic alteration (Helmold et al., 2013). However, the Mesozoic strata are pervasively fractured and oil seeps that occur along faults and fractures were first drilled on the Iniskin Peninsula from 1900–1906 (Blasko, 1976). The last well drilled on the Iniskin Peninsula was in 1959 and economical production was never realized (Blasko, 1976). One offshore well successfully produced 180,000 barrels of oil from a fractured Jurassic reservoir in the upper Cook Inlet (Lepain et al., 2013 and references therein). Understanding the density of regional fracture sets can inform the placement of well bores that can better produce a fractured reservoir (e.g., Engelder et al., 2009) and could bring economic potential to the low-porosity and permeability Mesozoic strata.

Methods

Macroscopic Fractures

Fracture apertures (widths) were measured along 31 scan lines in 9 formations following methods of Ortega and others (2006). The method involves identifying fracture sets in several geologic formations at outcrop scale, and placing a scan line perpendicular to each fracture set (figure 2.2; 2.3). Fracture apertures were only measured for cement filled fractures because they are likely to preserve the opening aperture and less likely to be widened by post-fracturing processes such as erosion (figure 2.2).

This study employs the size-normalized fracture intensity (number of fractures of a given size or larger) measurement scheme of Ortega and others (2006). I identified fracture sets at the 20 localities on the basis of fracture orientations. I set scan lines perpendicular to each observed set and then measured the position and aperture (width) of every cement-filled fracture encountered along each scan line with a tape measure and logarithmically graduated fracture aperture comparator (figure 2.2; Ortega et al., 2006). In some instances, outcrops only permitted the measuring of one fracture set due to the orientation of the outcrop and the fracture set so in some instances I only report the fracture intensity of one set even though there could have been multiple sets present. The method of Ortega and others (2006) is a scale-independent approach to quantify fracture aperture distributions because it normalizes the cumulative number of fractures by the length of observation.

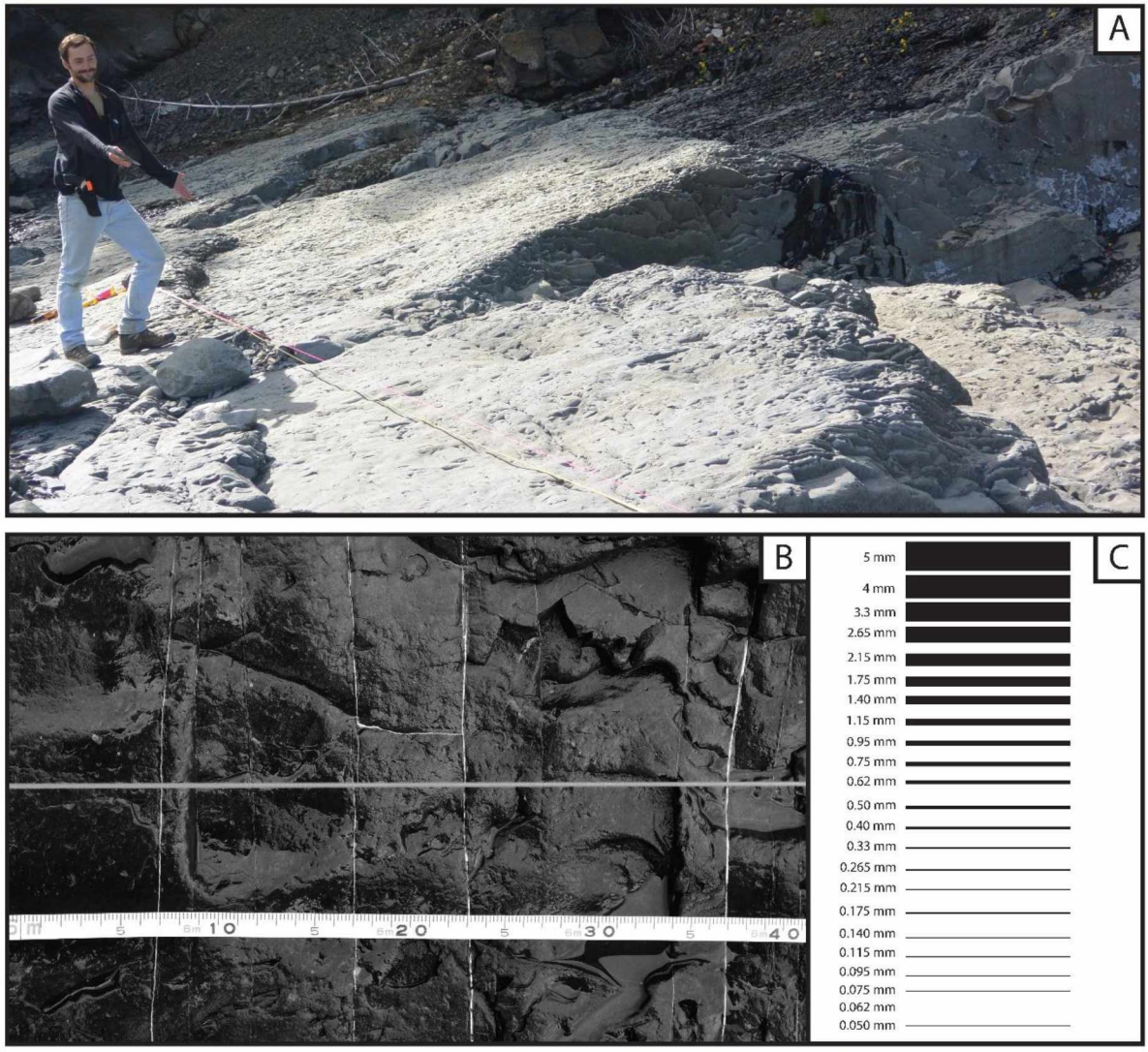
A
B
C
5 mm
4 mm
3.3 mm
2.65 mm
2.15 mm
1.75 mm
1.40 mm
1.15 mm
0.95 mm
0.75 mm
0.62 mm
0.50 mm
0.40 mm
0.33 mm
0.265 mm
0.215 mm
0.175 mm
0.140 mm
0.115 mm
0.095 mm
0.075 mm
0.062 mm
0.050 mm
D

Figure 2.2 Sample Scan Lines from the Field
A) Scan line at station JR006 strike normal to the 310° Set A. Set A fractures at this location strike roughly 344°. B) Detailed view of scan line in A showing several calcite filled fractures striking normal to scan line. C) I used a logarithmically gauged fracture comparator to quickly and accurately measure fracture width while progressing along a scan line. Typically, these are microscopically calibrated, but in the figure the comparator is not to scale. D) Scan line strikes normal to the 310° Set A at station JR010. Fractures of this set in this location strike 318°. Enhanced contrast and slight discoloration of the photos highlights the fractures.

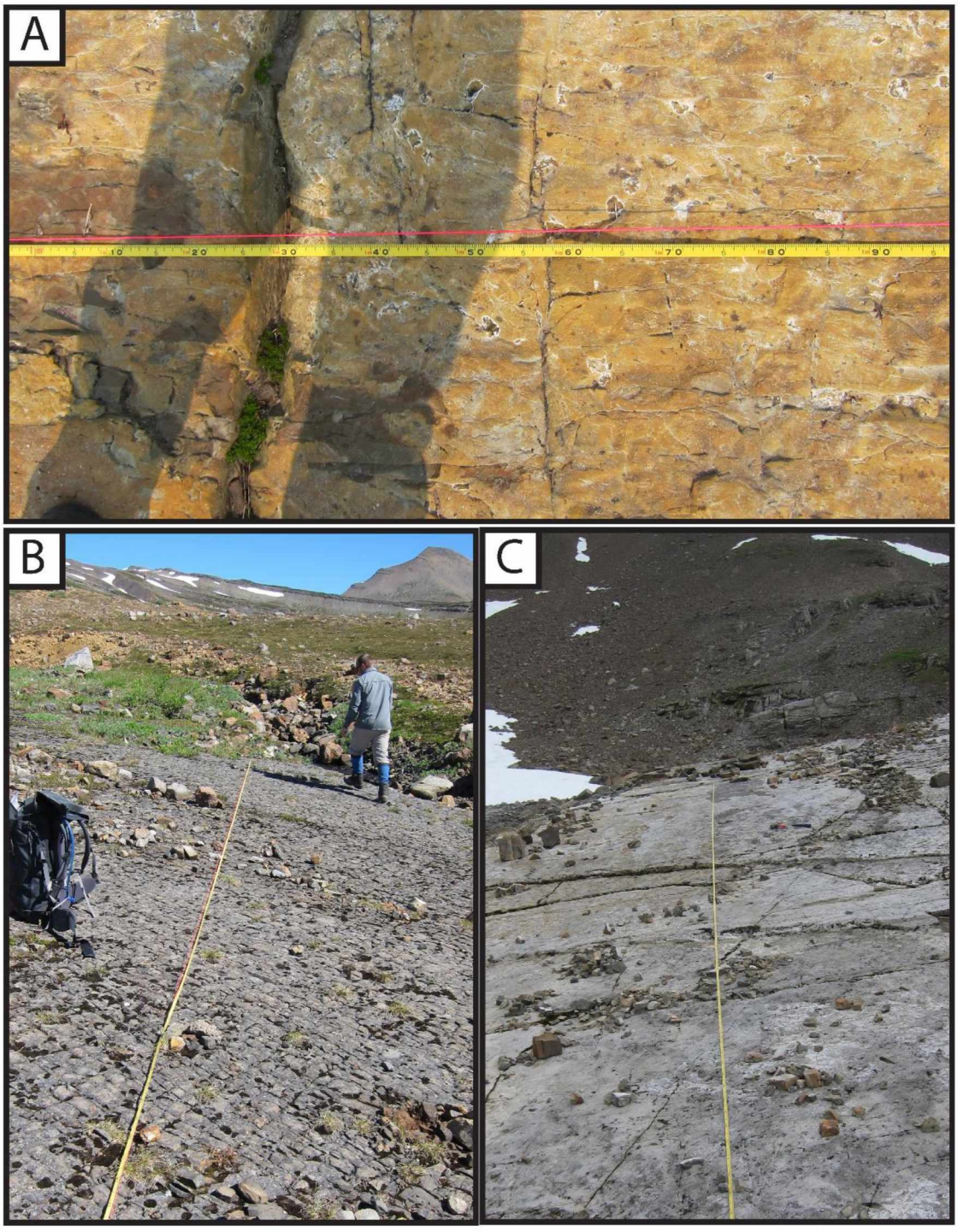

Figure 2.3 Sample Scan Lines from the Field
A) Scan line at station JR022 strike normal to the 310° Set A. Fractures of this set in this location on average strike 331°. B) Setting up a scan line normal to Set B at station JR019. Set B fractures in this location strike 226°. C) Scan line at station JR024 strike normal to the 310° Set A. Fractures in this locations strike on average 302°.

The cumulative number of fractures within each interval of measure (gradations on the comparator) are counted and normalized by the length of the scan line to determine the cumulative frequency per meter. Cumulative frequency versus aperture distributions fit power-law scaling relationships across five orders of magnitude (for example, Marrett and others, 1999). The coefficient and exponent of the power-law are determined by a least-squares regression; the coefficient represents the predicted number of fractures 1mm or larger per unit length and the exponent is the slope of the regression line in log-log space and thus is dependent on the abundance and range of fracture sizes (Ortega et al., 2006). Often, these regressions exhibit truncation and sampling biases. A sampling bias reflects the absence of large fractures encountered along the scan line because these fractures are less frequent. The truncation bias reflects a tendency to under sample fractures near the lower limit of detection. Data affected by truncation and sampling biases both plot below the regression line. In this study, data that reflected biases were excluded when calculating the least squares regression following methods after Ortega et al. (2006). I use the regression equation to compare fracture intensities from fracture sets at the 20 sampling locations to determine how fracture intensity correlates with formation and grain size.

Micro fractures

Fracture intensity was also determined by thin-section analysis of micro fractures from 3 locations along 3 microscopic scan lines. Samples were collected along macroscopic scan lines so that the fracture intensity data from micro- and macroscopic scan lines can be compared. Samples were oriented parallel with the scan line (normal to the observed fracture set) and several thin sections were cut from one sample so that a continuous sample of the scan line was preserved. [See Gomez and Laubach, (2006) for a description of the sampling methods employed in this study (figure 2.4).]

The thin sections were polished and carbon coated for use with the JEOL JXA-8530F scanning electron microscope at the University of Alaska Fairbanks Advanced Instrument Laboratory. I imaged these sections via backscattered electron microscopy, and constructed photo mosaics of micro-fractured samples to create scan lines across several thin sections.

Backscattered electron microscopy images were collected using a 10 nA beam current and 15 Kev accelerating voltage and a magnification of 500x. Using the microprobe imaging software *Thermo Scientific NSS* I chose an intermediate resolution of 1024 x 768. This resolution created a quality image without sacrificing processing time, roughly 300 images can be mosaicked at 1024 x 768 resolution.

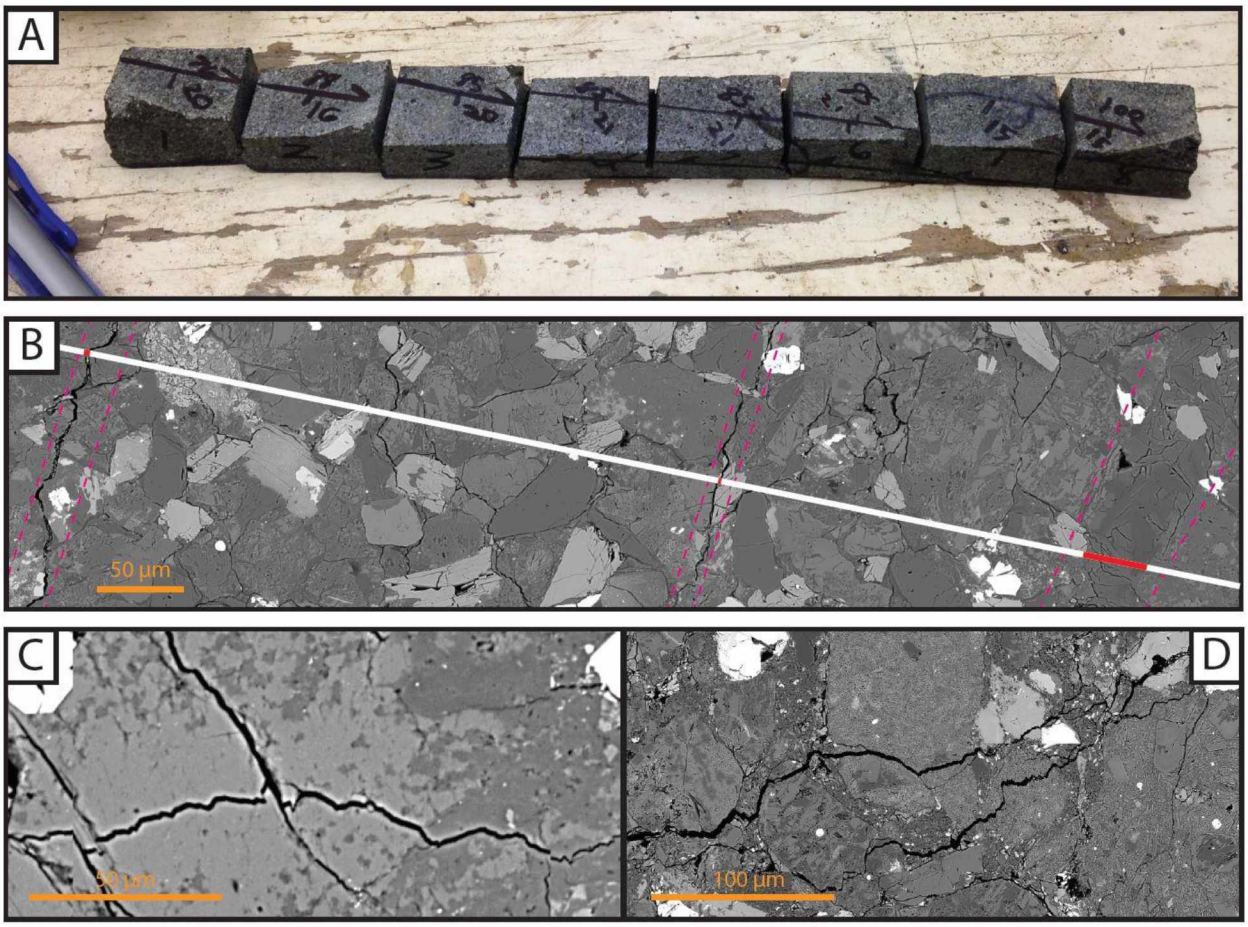

Figure 2.4 Microscopic Scan Line
A) Segmented thin section blocks to be made into a composite microscopic scan line (For more detailed explanation see figure 2 and 3 from Gomez and Laubach, 2006). Microscopic scan line from JR014. Scan line shown as white line, with fracture apertures highlighted in red. Filled macro fracture aperture shown at far right. C) Microscopic conjugate fracture from JR010. Suggests that macroscopic features scale microscopically. D) Microscopic fractures from JR018. Again suggests macroscopic features scale microscopically.

Using the "Grid" function under "Electron Imaging", a narrow grid (1-2 millimeters) of images was collected along the length of the sample (roughly 30 millimeters). This results in a grid of roughly 2 x 150 images. The images were merged into a single photo mosaic with the "Create Montage function under batch processing.

I subsequently used ImageJ image analysis software to measure fracture apertures in the photo mosaics. The process is as follows:

1. Set scale of image from a known measured length from Thermo Scientific NSS (this step assigns a length to a pixel size; i.e., 1 pixel equals 1 micron)

2. Draw a scan line normal to the fracture set of interest
3. Draw individual lines spanning each fracture aperture along the scan line
4. Use the measure function to measure each line spanning the fracture apertures
5. Export data

Microscopic fractures were plotted on cumulative frequency diagrams using the same methods described above. Microscopic fracture data were plotted with macroscopic data to evaluate the validity of extrapolating power law regressions of micro fractures to estimate macroscopic fracture intensity. The power law equation quantifies the fracture intensity over the range of fracture sizes and the coefficients and slopes can be used to compare fracture intensity with various lithologic parameters (i.e., grain size, cement percentage) (e.g., Ortega et al., 2010). I compare fracture intensity with grain size, formation, and fracture set.

Results

Field Results

Macro fractures were quantified at 20 stations in 9 formations using 31 scan lines. All data sets are best fit by power law regressions. 31 scan lines measured in the field area range from 1.835 to 35.48 m in length and were on average 9.684 m long. Macroscopic fracture apertures across the 31 scan lines ranged in size from 0.05 mm to 10 mm. The results are summarized in tables 2.1 and 2.2. Grain size values and rock type for each station are listed in table 2.2. The results are organized by formation and stratigraphic age. At some stations, scan lines were measured on vertical outcrops only, allowing the collection of a scan line against one fracture set. At other stations, time constraints due to weather, tides, or lateral constraints of outcrop size limited collection to one or two scan lines. Only on well exposed horizontal pavement outcrops with significant lateral extent and fracture fill was I able to measure scan lines of multiple sets.

Kamishak Formation

JR026

One scan line was used to document the fracture intensity of the 310° set at JR026 (figure 2.5a). The scan line length was 3.85 m and I measured 106 apertures (table 2.1). The mean strike of the 310° set at this location was 330°. Fracture apertures ranged in size from 0.05 – 8mm. The fracture intensity

coefficient and slope for the power law regression at this location are 2.248 and -0.834, respectively (table 2.2). The rock type was a micritic limestone, and the grain size was very fine lower (0.062 mm).

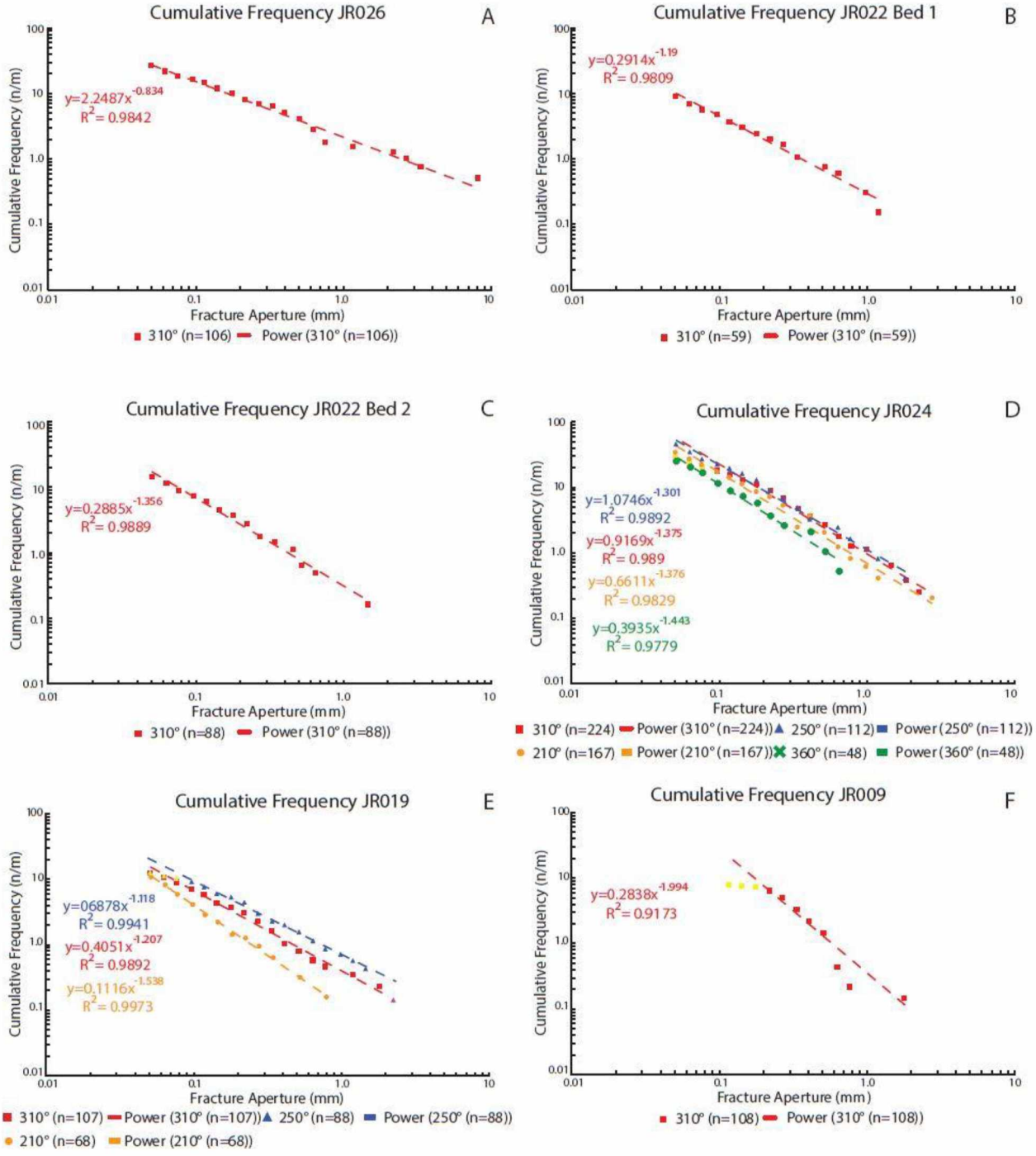

Figure 2.5 Cumulative Frequency Diagrams for Fracture Sets at each Station

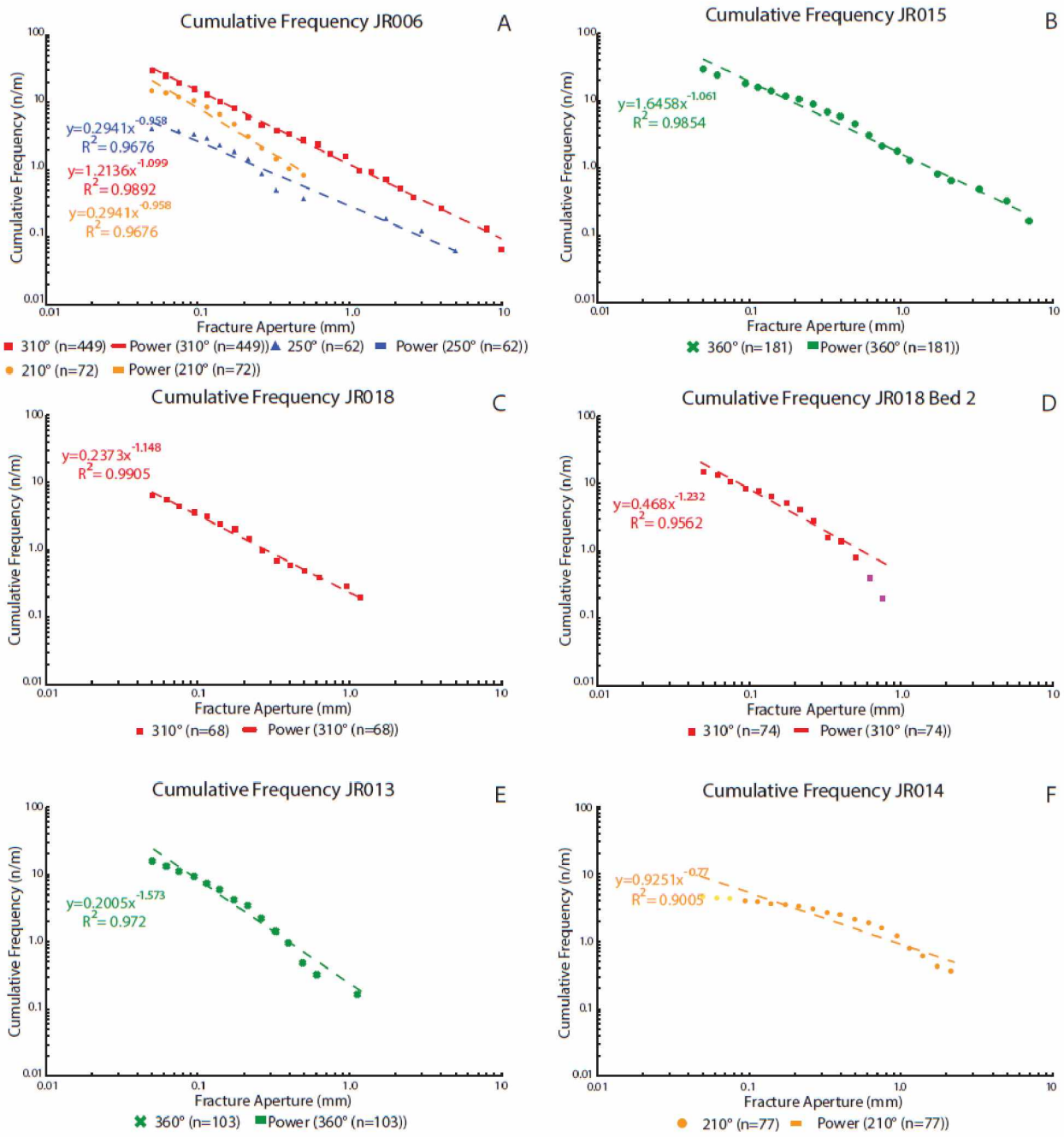

Figure 2.6 Cumulative Frequency Diagrams for Fracture Sets at each Station

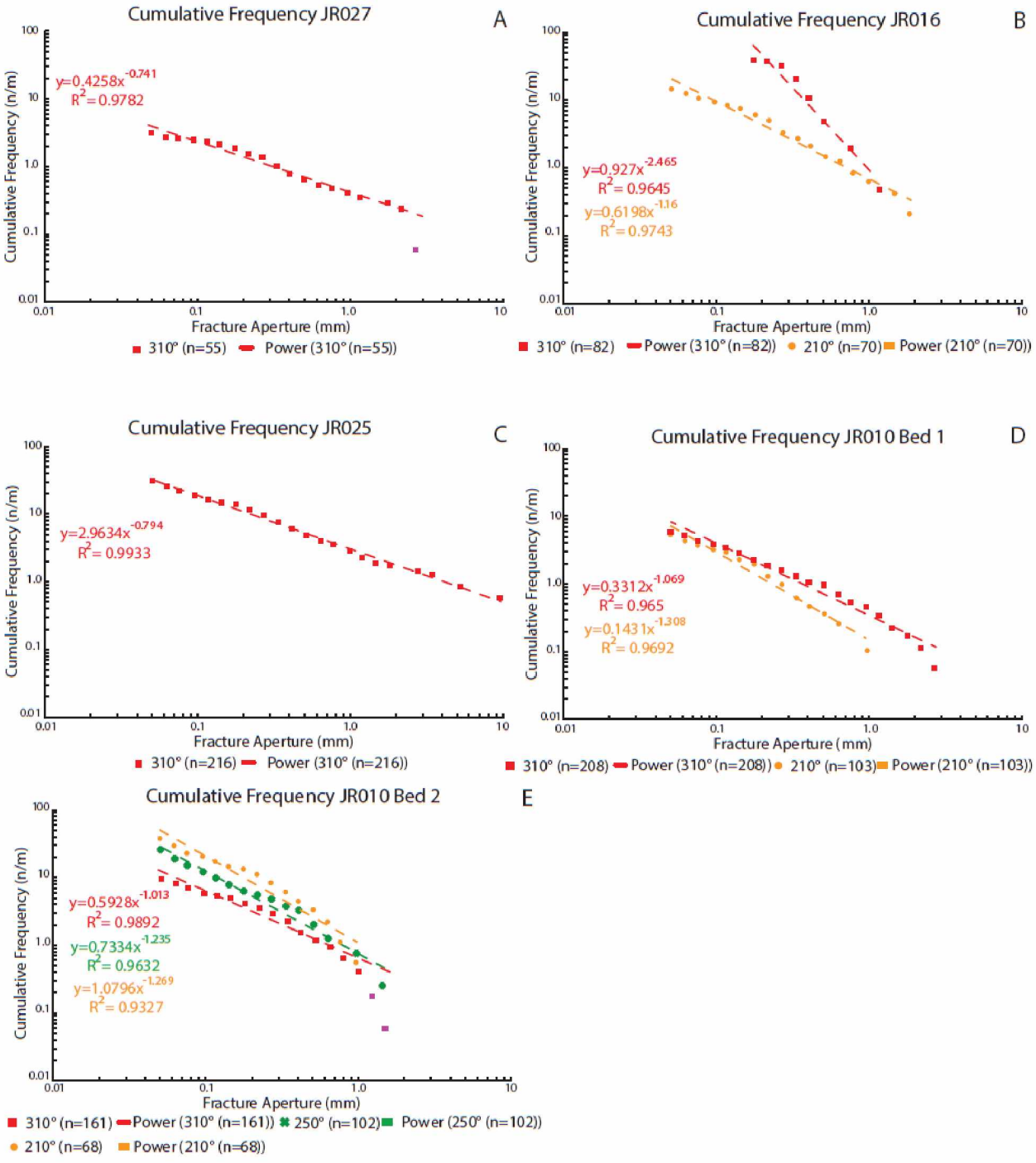

Figure 2.7 Cumulative Frequency Diagrams for Fracture Sets at each Station

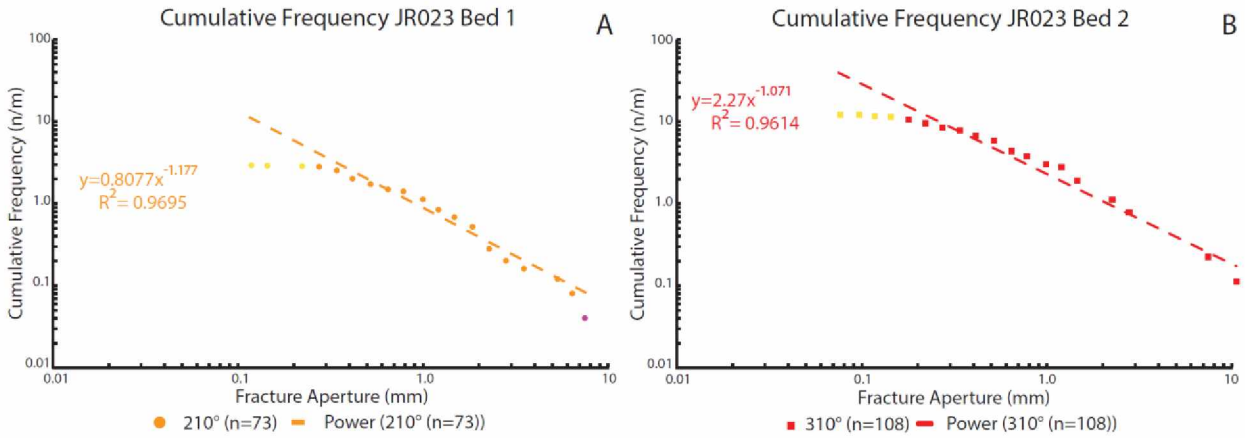

Figure 2.8 Cumulative Frequency Diagrams for Fracture Sets at each Station

Figures 2.6-2.9: Cumulative frequency diagrams for fracture sets measured at each station. Plots are logarithmic on the x and y axis with the x axis representing fracture aperture and the y axis representing cumulative frequency per meter. 310° Set A denoted with red. 210° Set B denoted with orange. 250° Set C denoted with blue. 360° Set D denoted with green. Power law regressions for each set are shown corresponding color to symbols with dashed lines. Power law regression equation shown as red text. Station number shown in graph title. See text for discussion.

Table 2.1: Station locations, orientations of stations, number of apertures measured, and scan line length

31 Scanlines															
20 Beds				Orientation of Fracture Set				Apertures Measured				Scanline Length (mm)			
Formation	Locality	Latitude	Longitude	310°	210°	250°	360°	310°	210°	250°	360°	310°	210°	250°	360°
Paveloff															
	JR006	59.65871	-153.30769	344°	200°	264°		448	72	65		14980	4750	15810	
	JR015	59.88626	-152.99414				365°				181				6300
	JR018-1	59.83365	-153.02826	335°				66				10040			
	JR018-2	59.83365	-153.02826	310°				74				5100			
Pomeroy															
	JR010-1 C	59.64826	-153.1805	318°	213°			208	103			35480	19440		
	JR010-2 D	59.64826	-153.1805	315°	220°		350°	161	68		102	16660	1835		3880
	JR023-1	59.87831	-152.9213		230°				73				24360		
	JR023-2	59.87831	-152.9213	295°				108				8730			
Red Glacier															
	JR019	60.02625	-152.94902	313°	226°	275°		107	68	88		8448	6192	6870	
Lower Sand															
	JR013	59.65213	-153.30525				360°				103				6800
	JR014	59.88463	-152.98842		201°				77				16800		
Cynthia Falls															
	JR009	60.16679	-152.67772	304°				108				13500			
Chisik Cng															
	JR027	60.15865	-152.56577	310°				54				16730			
Kamishak															
	JR026-1	59.55103	-153.59027	340°				106				3850			
	*JR026-2	59.55103	-153.59027				365°				115				860
Snugg Harbor															
	JR016	59.88459	-152.97722	300°	197°			87	70			2028	4880		
	JR025	59.55103	-153.59027	307°				216				6990			
Talkeetna															
	JR022-1	59.9065	-153.10472	331°				59				6400			
	JR022-2	59.9065	-153.10472	310°				88				6320			
	JR024	60.04193	-152.95216	325°	231°	275°	360°	224	167	112	48	7950	5042	2480	1900

Table 2.2: Power Law Coefficient, Power Law Exponent, Rock Type, Grain Size, Sample, and Thin Sections

31 Scanlines				Cumulative Frequency 1-D Coefficient				Cumulative Frequency 1-D Exponent							
20 Beds															
Formation	Locality	Latitude	Longitude	310°	210°	250°	360°	310°	210°	250°	360°	Rock Type	GS mm HS	Sample	Thin Section
Paveloff															
	JR006	59.65871	-153.308	1.213	0.2558	0.2941		-1.099	-1.364	-0.958		Siltstone	0.062	Y	Y 3
	JR015	59.88626	-152.994				1.6388				-1.049	Lithic Sandstone	0.25	N	N
	JR018	59.83365	-153.028	0.2373				-1.148				Lithic Sandstone	0.375	Y	Y 5
	JR018-2	59.83365	-153.028	0.468				-1.232				Lithic Sandstone	0.85	Y	Y 8
Pomeroy															
	JR010-1 C	59.64826	-153.181	0.3312	0.1431			-1.069	-1.308			Arkosic Sandstone	0.65	Y	Y 4
	JR010-2 D	59.64826	-153.181	0.5928	1.0796		0.7334	-1.013	-1.269		-1.235	Arkosic Sandstone	0.5	Y	Y 3
	JR023-1	59.87831	-152.921		0.8077				-1.177			Conglomerate	2	N	N
	JR023-2	59.87831	-152.921	2.27				-1.071				Lithic Sandstone	0.2	N	N
Red Glacier															
	JR019	60.02625	-152.949	0.4051	0.1116	0.6878		-1.207	-1.538	-1.118		Siltstone	0.05	Y	Y 4
Lower Sand															
	JR013	59.65213	-153.305				0.2005				-1.573	Lithic Sandstone	0.33	Y	N
	JR014	59.88463	-152.988		0.9251				-0.77			Lithic Sandstone	1	Y	Y 2
Cynthia Falls															
	JR009	60.16679	-152.678	0.2838				-1.994				Siltstone	0.062	Y	Y 4
Chisik Cng															
	JR027	60.15865	-152.566	0.4258				-0.741				Arkosic Sandstone	1.5	Y	Y 3
Kamishak															
	JR026-1	59.55103	-153.59	2.248				-0.834				Micritic Limestone	0.062	N	N
	*JR026-2	59.55103	-153.59				16.121				-0.707	Micritic Limestone	0.062		N
Snugg Harbor															
	JR016	59.88459	-152.977	0.927	0.6198			-2.465	-1.16			Siltstone	0.05	Y	Y 4
	JR025	59.55103	-153.59	2.7772				-0.844				Siltstone	0.05	Y	N
Talkeetna															
	JR022-1	59.9065	-153.105	0.2914				-1.19				Volcaniclastic Sandstone	0.5	N	N
	JR022-2	59.9065	-153.105	0.2885				-1.356				Volcaniclastic Sandstone	0.5	Y	Y 4
	JR024	60.04193	-152.952	0.9169	0.6611	1.0746	0.3935	-1.375	-1.376	-1.301	-1.443	Volcaniclastic Siltstone	0.062	Y	N

Talkeetna Formation

JR022 Bed 1

One scan line was used to document the fracture intensity of the 310° set at JR022 Bed 1 (figure 2.3; 2.5b). The scan line length was 6.40 m and I measured 59 apertures at the outcrop (table 2.1). The mean strike of the 310° set at this location was 331° and fracture apertures ranged in size from 0.05 – 1.15 mm. The fracture intensity coefficient and slope for the power law regression at this location are 0.2914 and -1.19, respectively (table 2.2). The rock type was a volcanoclastic sandstone, and the grain size was medium upper (0.5 mm).

JR022 Bed 2

Again, only one scan line was used to document the fracture intensity of the 310° fracture set at JR022 Bed 2 (figure 2.5c). The scan line length was 6.320 m and I measured 88 apertures (table 2.1). The mean strike for the 310° set at this location was 310°. Fracture apertures ranged in size from 0.05 – 1.40 mm. The power law regression coefficient and slope at this location are 0.2885 and -1.356, respectively (table 2.2). The rock type sampled was a volcanoclastic sandstone, and the grain size was medium upper (0.5 mm).

Red Glacier Formation

JR024

I measured four scan lines in 4 fracture sets at station JR024 Bed 2 (the 310°, 210°, 250°, and 360°) in the Red Glacier Formation (figure 2.3; 2.5d). Scan line lengths were 7.95 m (n=224), 5.042 m (n=167), 2.480 m (n=112), and 1.9 m (n=48) for the 310°, 210°, 250°, and 360° sets respectively (table 2.1). The mean strike for each set is 325° (310°), 231° (210°), 275° (250°), and 360° (360°) (table 2.1). Fracture apertures ranged from 0.05–2.65 mm across at this station. The fracture intensity coefficients for the 310°, 210°, 250°, and 360° sets are 0.9169, 0.6611, 1.0746, and .3935 respectively (table 2.2). The 250° fracture set had the highest coefficient by a small margin, followed by fracture set the 310°, 210° and 360° respectively. Power law regression slopes for the 310°, 210°, 250°, and 360° fracture sets are -1.375, -1.376, -1.304, and-1.443, respectively. The rock type was a volcaniclastic siltstone, and the grain size was very fine lower (0.062 mm).

JR019

Three scan lines at JR019 were used to document the fracture intensity of three fracture sets (310°, 210°, and 250°) in the Red Glacier Formation (figure 2.3; 2.5e). Scan line lengths were 8.448 m (n =107), 6.192 m (n=68), and 6.870 m (n=88) for the 310°, 210°, and 250° sets respectively (table 2.1). The mean strike for each set is 313° (310°), 226° (210°), and 275° (250°) (table 2.1). Fracture apertures ranged from 0.05–2.15 mm across all three sets. The fracture intensity coefficients for the 310°, 210°, and 250° sets are 0.4051, .1116, and 0.6878, respectively (table 2.2). The 250° is the most intense at this location, followed by the 310° and 210° fracture sets. Power law regression slopes for the 310°, 210°, and 250° fracture sets are -1.207, -1.538, and -1.118, respectively. The rock type was a siltstone, and the grain size was silt – very fine lower (0.05 mm).

Cynthia Falls Formation

JR009

I measured one scan line on the 310° set at station JR009 (figure 2.5f). The scan line was 13.5 m long and I measured 108 apertures at this pavement outcrop (table 2.1). The mean strike for the 310° set at this location was 304°. Fracture apertures ranged in size from 0.75 – 1.75 mm. The fracture intensity coefficient and slope for the power law regression at this location are 0.2838 and -1.994, respectively (table 2.2). The rock type was siltstone, and the grain size was very fine lower (0.062 mm).

Paveloff Siltstone Member (Chinitna Formation)

JR006

Three scan lines at JR006 were used to document the fracture intensity of three fracture sets (310°, 210°, and 250°) in the Paveloff Siltstone Member (figure 2; 2.6a). Scan line lengths were 14.98 m (number of fractures (n) =449), 4.75 m (n=72), and 15.81 m (n=62) for the 310°, 210°, and 250° sets, respectively (table 1). The mean strike for each set is 344° (310°), 200° (210°), and 264° (250°) (figure 2.2e). Fracture apertures ranged from 0.05–10 mm across all three sets. The fracture intensity coefficients the 310°, 210°, and 250° sets are 1.21, 0.36, and 0.29, respectively (table 2.2). The 310° set is the most intense at this location, followed by fracture by the 210° and then 250° sets. Power law regression slopes for the 310°, 210°, and 250° sets are -1.099, -1.364, and -0.958, respectively. The rock type was a siltstone, and the grain size was silt to very fine lower sand (0.062 mm).

JR015

One scan line was used to document the fracture intensity of the 360° fracture set at JR015 (figure 2.6b). The scan line length was 6.3 m and I measured 181 apertures (table 2.1). The mean strike for the 360° set at this location was 365°. Fracture apertures ranged in size from 0.05 – 7 mm. The fracture intensity coefficient and slope for the power law regression at this location are 1.6458 and -1.061, respectively (table 2.2). The rock type was a lithic sandstone, and the grain size was fine – medium lower (0.25 mm).

JR018 Bed 1

I measured the fracture intensity of fracture 310° at JR018 Bed 1 using a single scan line (figure 2.6c). The scan line was 10.04 m long and 71 apertures were measured at this station (table 2.1). The mean strike for the 310° set at this location was 325°. Fracture apertures ranged in size from 0.05 – 1.15 mm. The fracture intensity coefficient and slope for the power law regression at this location are 0.2373 and -1.232, respectively (table 2.2). The rock type was a lithic sandstone, and the grain size was medium upper to medium lower (0.375 mm).

JR018 Bed 2

One scan line was used to document the fracture intensity of the 310° set at JR018 in a finer grained bed (figure 6d). The scan line length was 5.1 m and I measured 74 apertures (table 2.1). The mean strike for the 310° set at this location was 310°. Fracture apertures ranged in size from 0.05 – 0.75 mm. The fracture intensity coefficient and slope for the power law regression at this location are 0.4684 and -1.148, respectively (table 2.2). The rock type was a lithic sandstone, and the grain size was medium upper (0.85 mm).

Lower Sandstone Member (Naknek Formation)

JR013

Using a single scan line at JR013, I documented the fracture intensity of the 360° set (figure 2.6e). The scan line length was 6.8 m and I measured 103 apertures (table 2.1). The average strike for the 360° set at this location was 360°. Fracture apertures ranged in size from 0.05 – 1.15 mm. The fracture intensity coefficient and slope for the power law regression at this location are 0.2005 and -1.573, respectively (table 2.2). The sampled outcrop was composed of lithic sandstone and the grain size of the rocks was medium lower (0.33 mm).

JR014

I document the fracture intensity of the 210° fracture set at station JR014 using one scan line (figure 2.6f). The scan line was 16.8 m long and I measured 77 apertures (table 2.1). The mean strike for the 210° set at this location was 200°. Fracture apertures ranged in size from 0.05 – 2.65 mm. The fracture intensity coefficient and slope for the power law regression at this location are 0.9251 and -0.77, respectively (table 2.2). The rock type was a lithic sandstone, and the grain size was medium upper to very coarse lower (1 mm).

Chisik Conglomerate Member (Naknek Formation)

JR027

One scan line was used to document the fracture intensity of the 310° at JR027 (figure 2.7a). The scan line length was 16.73 m and I sampled 54 apertures along its length (table 2.1). The mean strike for the 310° at this location was 310°. Fracture apertures ranged in size from 0.05 – 2.65 mm. The fracture intensity coefficient and slope for the power law regression at this location are 0.4258 and -0.741 respectively (table 2.2). The rock type was an arkosic sandstone, and the grain size was very coarse upper (1.5 mm).

Snug Harbor Siltstone Member (Naknek Formation)

JR016

Two scan lines at JR016 document the fracture intensity of two fracture sets (310° and 210°) in the Snug Harbor Siltstone Member (figure 2.7b). Scan line lengths were 2.028 m (n=208) and 4.88 m (n=103) for the 310° and 210° sets, respectively. The mean strike for each set is 300° (310°) and 197° (210°) (table 2.1). Fracture apertures ranged from 0.05–1.75 mm across both sets. The fracture intensity coefficients for the 310° and 210° sets are 0.927 and 0.6198, respectively (table 2.2). The 310° set has the highest intensity of fracture sets at this location. Power law regression slopes for the 310° and 210° sets are -2.465 and -1.16, respectively. The rock type was a siltstone, and the grain size was silt to very fine lower (0.05 mm).

JR025

One scan line on a vertical outcrop was used to document the fracture intensity of the 310° set at JR025 (figure 2.7c). The scan line was 6.99 m long and I measured 216 apertures along the face of the outcrop

(table 2.1). The mean strike for the 310° set at this location was 307°. Fracture apertures ranged in size from 0.05 – 10 mm. The power law regression fracture intensity and slope at this location are 2.9634 and -0.794, respectively (table 2.2). The rock type was a very fine siltstone (0.05 mm).

Pomeroy Arkose Member (Naknek Formation)

JR010 Bed 1

I measured two scan lines at JR010 Bed One document the fracture intensity of the 310° and 210° fracture sets at this station in the Pomeroy Arkose Member (figure 2.2, 2.7d); the 250° set was present but was not measured at this locality. Scan line lengths were 35.48 m (n=208) and 19.44 m (n=103) for the 310° and 210° sets, respectively. The mean strike for each set is 318° (310°) and 215° (210°) (table 2.1). Fracture apertures ranged from 0.05–2.65 mm across both sets. The fracture intensity coefficients for sets A and B are 0.33 and 0.14, respectively (table 2.2). The 310° set has the highest intensity of fracture sets at this location. Power law regression slopes for fractures of the 310° and 210° sets are -1.069 and -1.308, respectively. The rock type was arkosic sandstone, and the grain size was medium upper (0.65 mm).

JR010 Bed 2

In this finer grained bed at station JR010 in the Pomeroy Arkose, I measured three scan lines to document the fracture intensity of three fracture sets (310°, 210°, and 360°) (figure 2.7e). Scan line lengths were 16.60 m (n =161), 1.835 m (n=68), and 3.880 m (n=102) for sets the 310°, 210°, and 360°, respectively (table 2.1). The mean strike for each set is 315° (310°), 220° (210°), and 350° (360°) (table 2.1). Fracture apertures ranged from 0.05–1.4 mm across all three sets. The fracture intensity coefficients for the 310°, 210°, and 360° sets are 0.5928, 1.0796, and 0.7334, respectively (table 2.2). The 210° set has the highest fracture intensity in this particular bed, followed by the 360° and 310° sets respectively. Power law regression slopes for fractures the 310°, 210°, and 360° sets are -1.013, -1.269, and -1.235, respectively. The rock type was an arkosic sandstone, and the grain size was medium lower (0.5 mm).

JR023 Bed 1

One scan line was used to document the fracture intensity of fracture 210° at JR023 in a coarse grained bed (figure 8a). The scan line length was 24.36 m and I measured 73 apertures (table 2.1). The mean strike for the 210° set at this location was 230°. Fracture apertures ranged in size from 0.05 – 7 mm. The

fracture intensity coefficient and slope for the power law regression at this location are 0.8077 and -1.177, respectively (table 2.2). The rock type was a matrix-supported conglomerate, and the matrix grain size was very coarse upper (2 mm).

JR023 Bed 2

I measured a single scan line in the second fine-grained bed at Station JR023 normal to the 310° set (figure 8b). This scan line was 8.73 m long and I was able to measure 108 apertures along its length (table 2.1). The mean strike for the 310° set at this location was 295°. Fracture apertures ranged in size from 0.05 – 10 mm. The fracture intensity coefficient and slope for the power law regression at this location are 2.27 and -1.071, respectively (table 2.2). The rock type was lithic sandstone, and the grain size was medium lower to fine sand (0.2 mm).

Micro fractures

Micro fractures were quantified on thin sections from the Paveloff Member of the Chinitna Formation (JR018), and the Pomeroy and lower sandstone members of the Naknek Formation (JR010 and JR014, respectively). Micro fracture measurements were compared with the macro fracture data in each location. Microscopic scan lines from the three thin sections range from 18 to 28 mm in length and were on average 24 mm long. Fracture fill was generally absent; thus I measured unfilled fracture apertures. Microscopic fracture apertures across the three thin sections ranged in size from 0.0003 mm to 0.036 mm. Macroscopic fracture apertures from the corresponding three field sites range from .05 mm to 2.65 mm. Altogether, the fracture apertures span five orders of magnitude.

Paveloff Siltstone Member (Chinitna Fomation)

One scan line was used to document the microscopic fracture intensity of the 310° set in a thin section from bed 1 from JR018 (figure 2.9a). The scan line length was 28 mm and I measured 74 apertures. The mean strike for the 310° fracture set was 295° at this location. Fracture apertures ranged in size from 4.5 x 10^{-4} – 4.5 x 10^{-2} mm. The fracture intensity coefficient and slope for the power law regression at this location are 0.2179 and -1.435, respectively.

Lower Sandstone Member (Naknek Formation)

One scan line was used to document the microscopic fracture intensity of the 210° set in a thin section from bed 1 from JR014 (figure 2.9b). The scan line length was 18 mm and I measured 112 apertures. The mean strike for the 210° set at this location was 201°. Fracture apertures ranged in size from 2.5 x 10^{-4} –

8.9 x 10^{-2} mm. The fracture intensity coefficient and slope for the power law regression at this location are 0.3005 and -1.384, respectively.

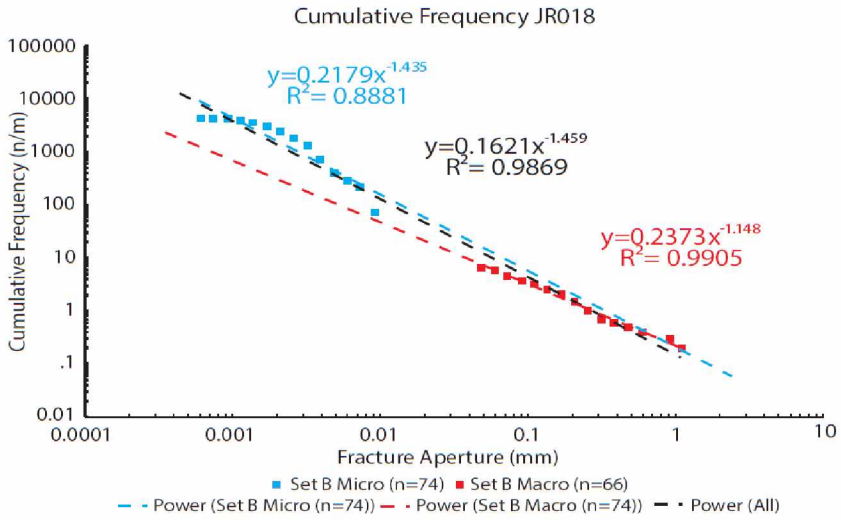

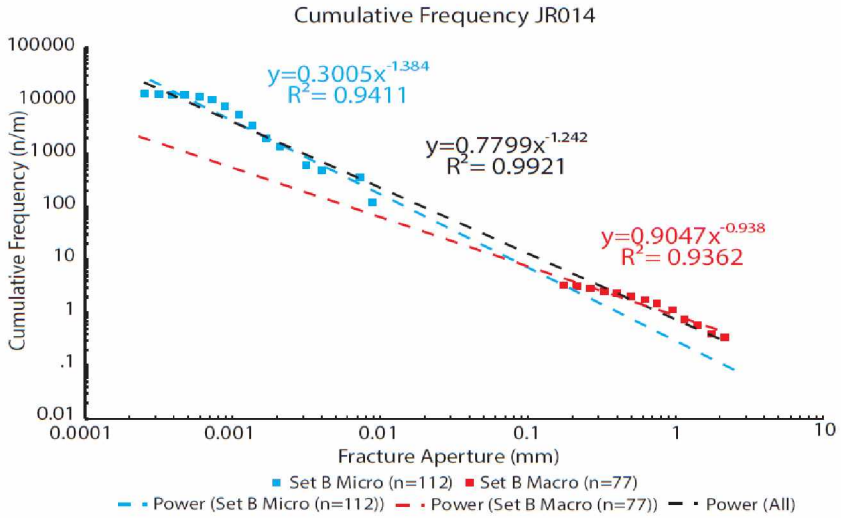

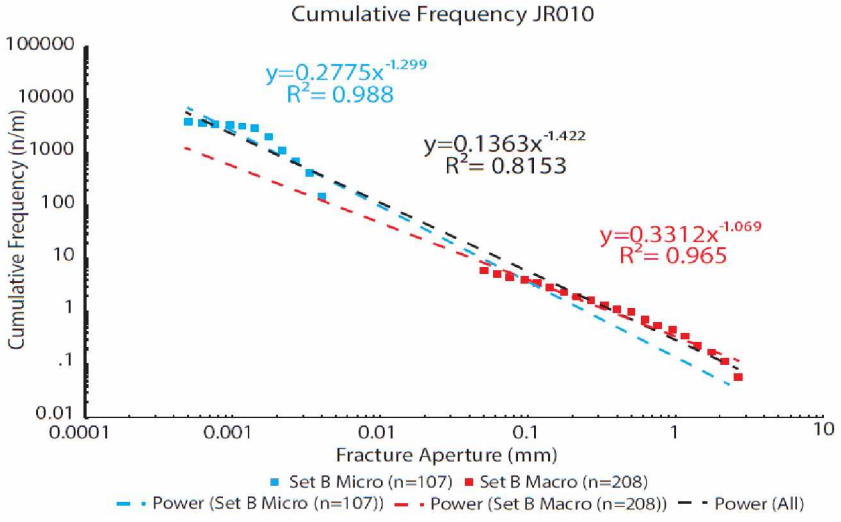

Figure 2.9 Cumulative Frequency Diagrams for Microscopic and Macroscopic Fractures
Cumulative frequency diagrams for microscopic and macroscopic fractures for station JR018, JR014, and JR010, respectively. Plots are logarithmic on the x and y axis with the x axis representing fracture aperture and the y axis representing cumulative frequency per meter. JR010 (top) and JR018 (bottom) show fractures from the 310°, and JR014 shows fractures from the 210° set (middle). Microscopic fractures shown with blue and macroscopic fractures shown with red. Regression lines are color coded to match with the microscopic or macroscopic data and extrapolated to show differences in predicted and actual estimations. Black regression line is regression line for the microscopic and macroscopic fractures combined.

Pomeroy Arkose Member Naknek Formation

One scan line was used to document the microscopic fracture intensity of the 310° set in a thin section from bed 1 from JR010 Bed One (figure 2.9c). The scan line length was 27.7 mm and I measured 107 apertures. The mean strike for the 310° set at this location was 318°. Fracture apertures ranged in size from $5 \times 10^{-4} - 4 \times 10^{-3}$ mm. The fracture intensity coefficient and slope for the power law regression at this location are 0.2775 and -1.299 respectively.

Analysis of Results

In this section, I statistically analyze the distribution of fracture intensity (of fractures ≥ 0.2 mm) and least-squares regression coefficients and exponents (slopes). I test for a relationship between grain size and fracture intensity (of fractures ≥ 0.2 mm) and I evaluate how fracture intensity changes across different formations in the field area. Lastly, I qualitatively evaluate how fractures of larger or smaller size cluster along four example scan lines.

Testing for a correlation between Fracture Intensity (≥ 0.2 mm) and grain size.

To test for a relationship between fracture intensity (fractures ≥ 0.2 mm) and grain size I plotted grain size vs. fracture intensity for all four fracture sets (figure 2.10). The 310° set shows a poor negative correlation between fracture intensity and grain size ($R^2 = 0.334$; fig. 10a). The three remaining fracture sets show no correlation between fracture intensity and grain size ($R^2 < 0.1$ in each case). When all of the data are plotted together, there is no correlation ($R^2 = 0.089$; Fig. 10e). Therefore, I conclude that fracture intensity is not influenced by grain size in the beds and formations in which I sampled.

Testing for a correlation between fracture intensity, rock formation, and fracture set.

To evaluate how fracture intensity varies by formation and fracture set I plotted histograms that show the fracture intensity (F>0.2mm) and exponents of the least-squares regression equations for each fracture set and formation in the field area (figure 2.11). Figure 2.11a shows the distribution of fracture intensity (F>0.2mm). The 310° set has generally higher fracture intensities than the other fracture sets, followed by the 210°, 360°, and 250° sets. The 250° fracture set has the highest fracture intensity at two of the three stations where it was sampled. There is no apparent trend between fracture intensity and formation. Fracture intensities vary within all studied formations. Individual formations contain both relatively high and low fracture intensities in similar strata. Three stations with highest fracture intensities are

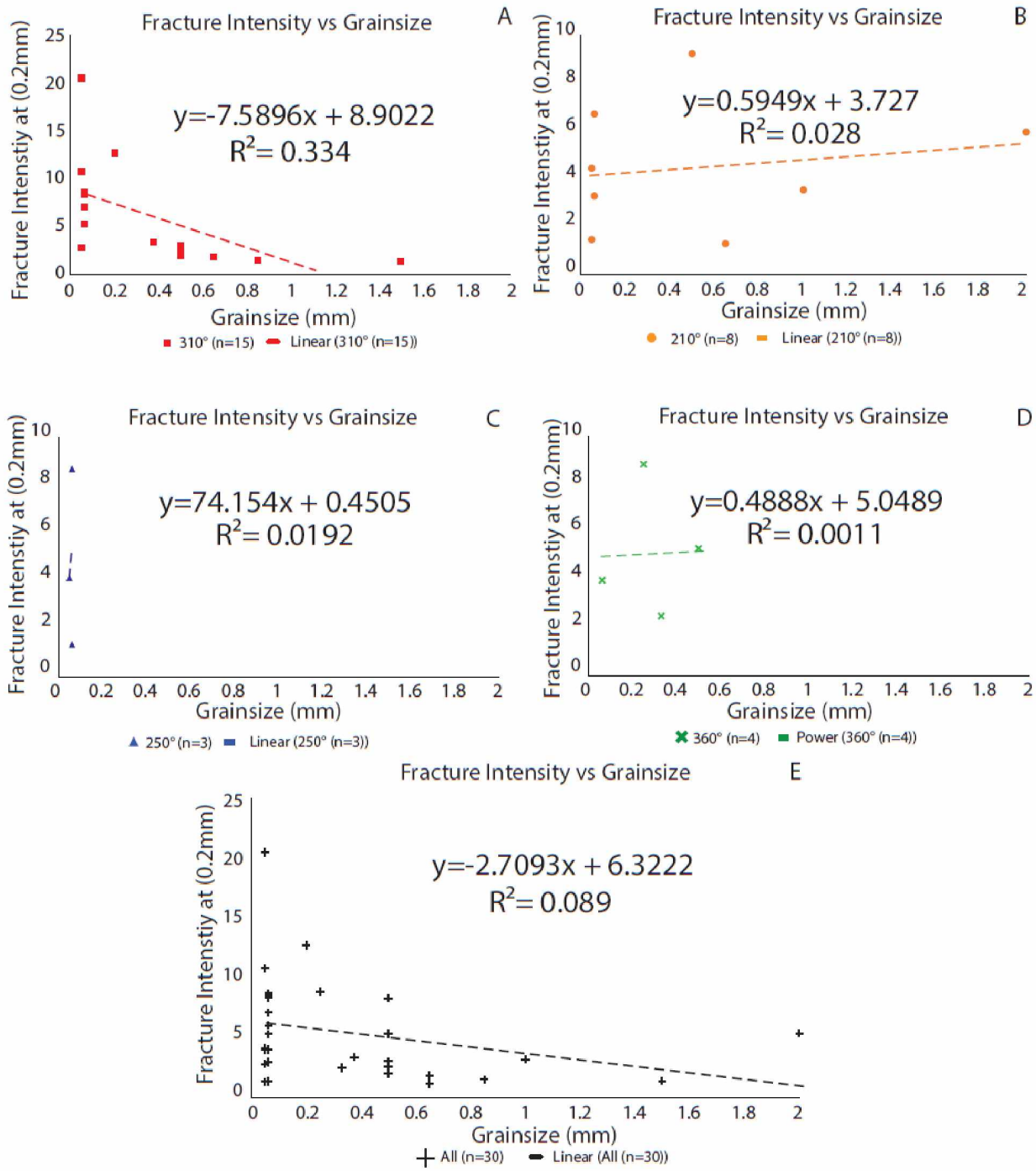

Figure 2.10 Fracture Intensity versus Grain Size

Fracture Intensity vs grain size. Fracture set labeled at top of figure. X and y axes are logarithmic with grain size in mm on the x axis and fracture intensity of 0.2 mm on the y axis. Regression shown as dashed line on graph. See text for discussion.

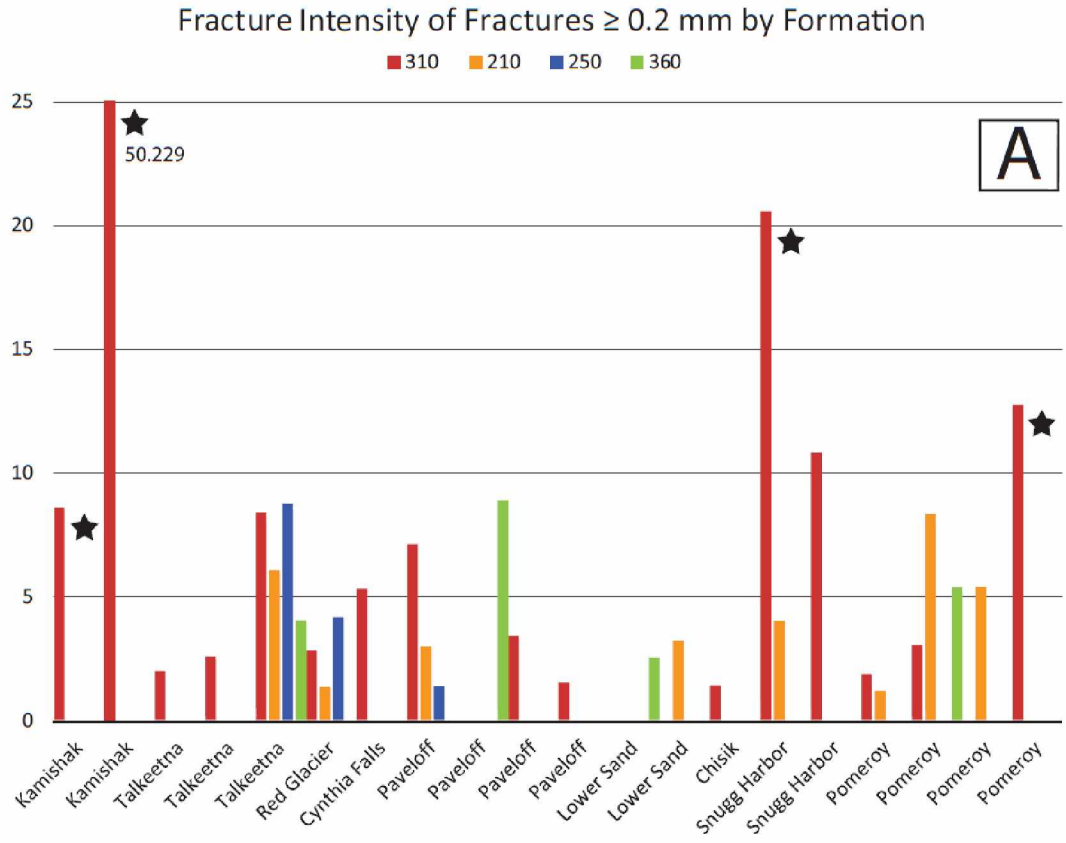
Fracture Intensity of Fractures ≥ 0.2 mm by Formation
310
210
250
360
25
20
15
10
5
0
50.229
A
Kamishak
Kamishak
Talkeetna
Talkeetna
Talkeetna
Red Glacier
Cynthia Falls
Paveloff
Paveloff
Paveloff
Paveloff
Lower Sand
Lower Sand
Chisik
Snugg Harbor
Snugg Harbor
Pomeroy
Pomeroy
Pomeroy
Pomeroy

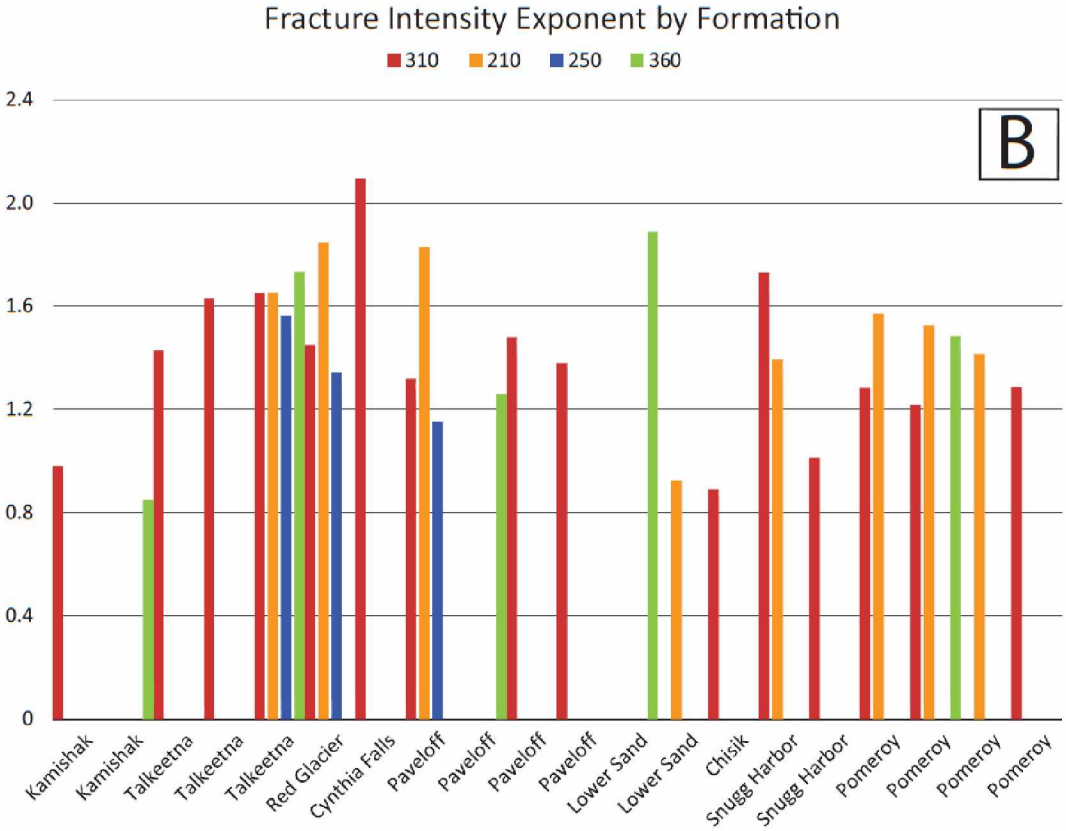
Fracture Intensity Exponent by Formation
310
210
250
360
2.4
2.0
1.6
1.2
0.8
0.4
0
B
Kamishak
Kamishak
Talkeetna
Talkeetna
Talkeetna
Red Glacier
Cynthia Falls
Paveloff
Paveloff
Paveloff
Paveloff
Lower Sand
Lower Sand
Chisik
Snugg Harbor
Snugg Harbor
Pomeroy
Pomeroy
Pomeroy
Pomeroy

Figure 2.11 Fracture Intensity and Power Law Exponent vs Formation
Top) Fracture intensity of fractures ≥ 0.2 mm vs formation. Fracture intensities are organized by fracture set and color coded on graph and organized by formation labeled on the x axis. See text for discussion. Bottom) Power law regression exponent vs formation. Power law regression exponents are organized by fracture set and color coded on graph and organized by formation labeled on the x axis. See text for discussion. Black stars denote stations with relatively high fracture intensities that are near faults.

located near faults (i.e., the Bruin Bay fault, figure 2.1). Thus, it is likely that faults locally increased the intensity of fracture sets.

When the exponents are compiled in figure 11b, there is a small amount of variability across all formations and no trend is apparent. Slopes generally range from -1 to - 1.2 and seem to be well characterized by that exponent. Because there are not trends in the data (i.e., consistently higher or lower fracture intensity [figure 2.11a] or exponents [figure 2.11b] within formations), I conclude that the fracture intensity is not controlled by lithologic changes across formations.

To describe the bulk distribution of fracture intensity throughout the study area, figure 2.12 shows the histograms of fracture intensity (figure 2.12a) (F>0.2mm) as well as the coefficients (figure 2.12b) and exponents (figure 12c) of the regression equations throughout the study area. Fracture intensities for fractures ≥ 0.2 mm range from 1.17 to 20.536, or one order of magnitude (figure 2.12a). The power law coefficients are not normally distributed and have significant outliers. The mean coefficient is 0.816 for the study area. The fracture intensity exponents are normally distributed with a slight skew to the left. The 95% confidence intervals of fracture intensity coefficients and slopes are 0.816 (± 1.212) and -1.188 (± 0.504), respectively (figure 2.12b, c).

To further test the hypothesis that fracture intensity varies by fracture set, intensities for the four fracture sets were statistically analyzed using a box plot (figure 2.13). This shows that while there is more variability within the 310° fracture set, all four fracture sets are fairly close in median fracture intensity. The box plot tails show the range of fracture intensity for each set and the boxes show the 1st, 2nd (median value) and 3rd quartile of the distribution (figure 2.13; table 2.3). The data suggests that fracture intensity does not vary significantly by fracture set.

Fracture Spacing

Finally, to qualitatively evaluate if the relative densities of fracture sizes varied along the scan lines spatially, I plotted fracture aperture vs distance along the scan line (figure 2.14 and 2.15). In all four examples, large fractures cluster closely together, separated by numerous smaller fractures. I interpret this clustering to indicate that opening and slip on large fractures creates and proliferates additional smaller fractures locally (Pollard and Segall, 1987).

Discussion

In the previous section, I tested for a correlation between fracture intensity (of fractures ≥ 0.2 mm), power law regression coefficients and slopes with formation, grain size, and fracture set as well as spatial clustering of large fractures. I now discuss those results in the context of previous work. I begin the discussion by offering explanations for the variation in fracture intensity in my field area. I then move on to discuss variability in fracture intensity at outcrop, power law regression slope by formation, power law scaling relationships, and lastly the implications for micro fractures as predictors of macro fractures.

Results indicate that within the study area, variation in fracture intensity does not correlate with grain size. Ortega et al. (2010), correlate fracture intensity with dolomite content, mud content, and facies changes. Thus, it is plausible that through additional sedimentary analysis of the studied lithology, one could find further lithologic controls on fracture intensity using this data as a starting point. Possible lithologic controls could be cement type, cement percentage, and depositional environment (i.e., subtidal, intertidal, etc.). However, there is little variation in fracture intensity across formations that were deposited in different depositional environments within the field area (figure 2.11). Thus, it is likely that variation in fracture intensity does not vary with lithologic changes in the study area.

Alternatively, I postulate that fracture intensity differences likely stem from changes in local structural complexity (i.e., nearby faults [Savage and Brodsky, 2011]) (figure 2.1; 2.11). Three stations (JR025, JR023, and JR026) were sampled near known mapped faults, and had higher fracture intensities than stations not sampled near faults. My fracture spacing data are consistent with observations made by Savage and Brodsky (2011) where fracture intensity increases as fractures are closer to faults and other large fractures (figure 2.14-2.15). High strain localized along faults and/or other large fractures could likely cause fractures to coalesce and locally increase the fracture density.

The slopes (exponents) of power law regressions that quantify fracture intensity show little variation on average throughout the study area with overall a small range in values (figure 2.11; 2.12). This suggests that relative fracture frequency between fracture sizes (i.e., 10 small fractures for 1 big fracture) are consistent across a wide range of lithologies and locations within my field area. This observation is consistent with previous work in fracture intensity, where it has been proposed that one could use a

universal scaling exponent for power law correlations in specific rock types and regions (e.g., Hooker et al., 2014). Thus, given the consistency and normal distribution of slopes across my study area, I suggest that a universal scaling exponent could be used when discussing fracture intensities in the region. I propose that an exponent of -1.188 (± 0.504) could accurately estimate 95% of slopes for power law regressions in the Cook Inlet.

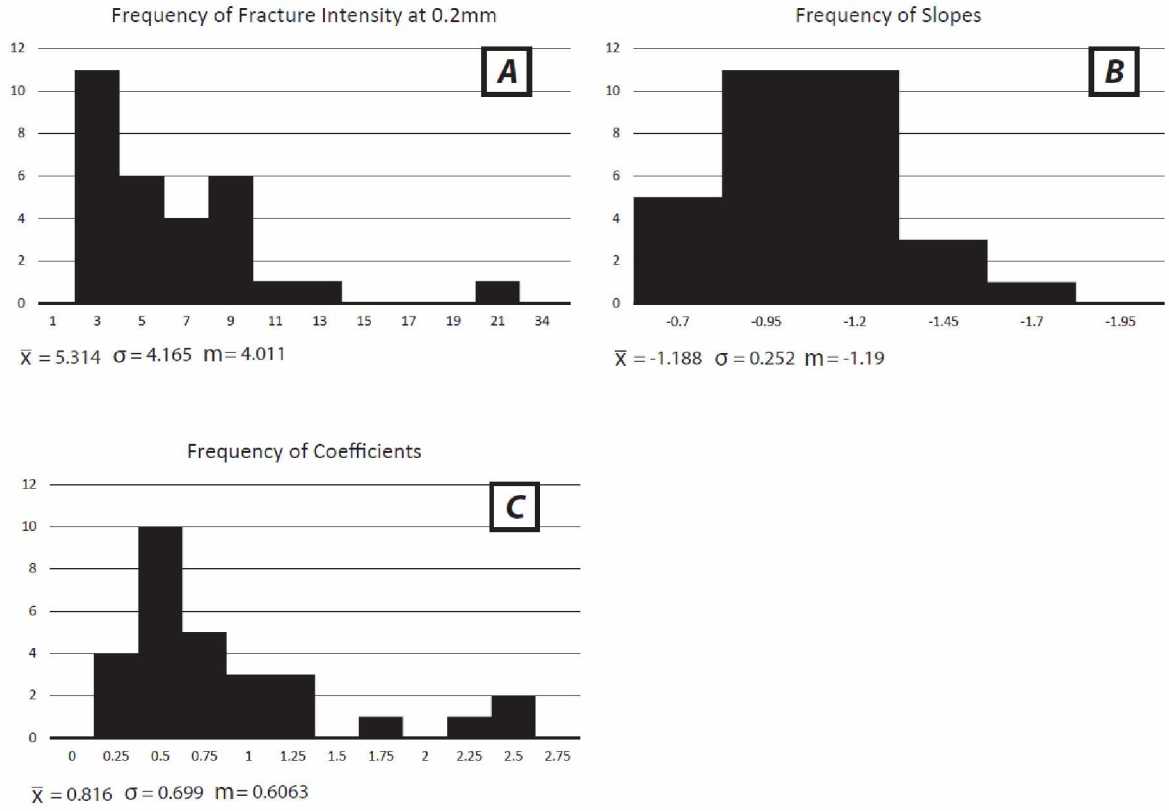

Figure 2.12 Histograms of Fracture Intensity, Coefficient, and Slope
Histograms of fracture intensity of 0.2 mm of larger and slope. A) Fracture intensities of 0.2mm or larger are not normally distributed as evidenced by significant difference in median and mean. A significant tail to the right and a skewed peak on left of graph effectively demonstrates a skewed distribution. B) Frequency of slopes are apparently normally distributed as evidence by similar median and mean. There is a very slight left skew. C) Coefficients are not normally distributed showing significant outliers to the right with a strong left skew. See text for discussion.

Micro fractures from my samples span 2.5 orders of magnitude in size and generally show stronger truncation and observation biases than the macro fracture data (figure 2.9). Due to limitations in resolution, I could not measure the smallest of micro fractures. Thus, I could potentially miss and therefore not quantify the true abundance of micro fractures (e.g., Hooker et al., 2014). Large fractures were rare in my thin sections, likely because the samples I collected were often plucked from the

margins of preexisting macro fractures in the field; statistically reducing the likelihood of their presence in my samples.

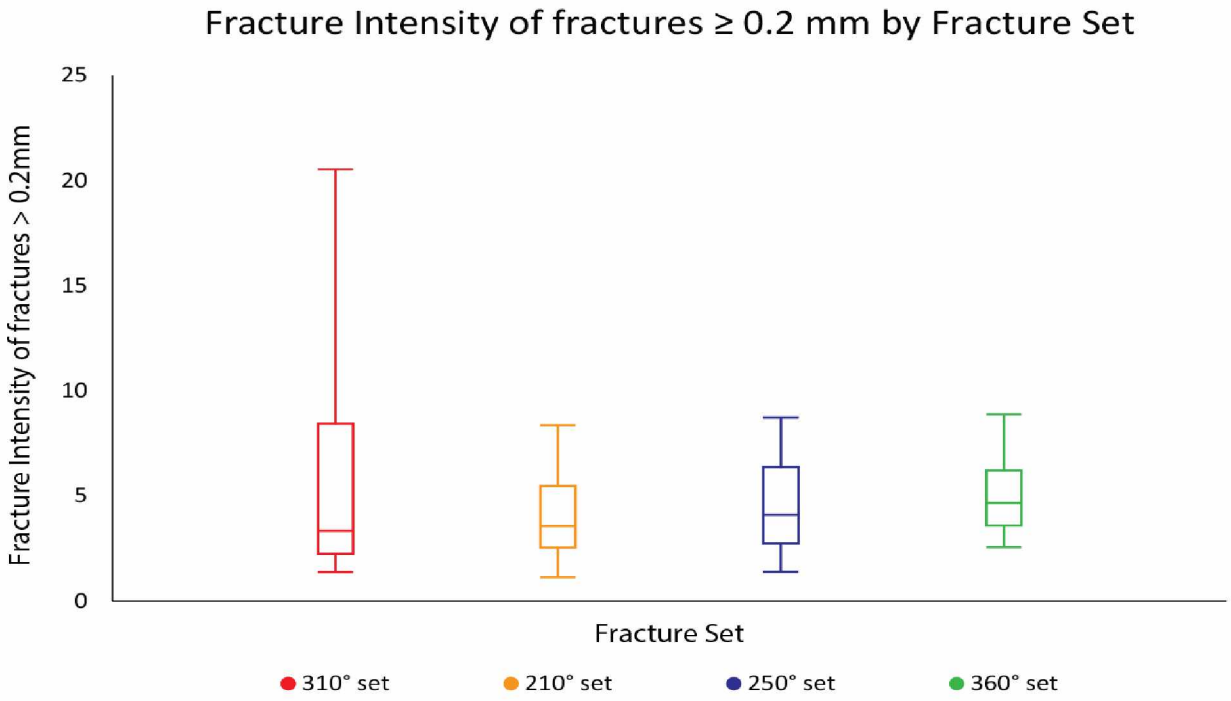

Figure 2.13: Box Plots of Fracture Intensity by Set
Box plots for fracture intensities of 0.2 mm of the four fracture sets. Minimum and maximum intensities shown with tails, and 1st 2nd and 3rd quartiles are shown by boxes, with the lower margin of the box representing the 1st quartile, middle representing the 2nd quartile, and the top of the box representing the 3rd quartile.

The exponents and coefficients of the regression equations for micro fractures are well within the 95% confidence interval for slopes and coefficients established by outcrop analysis of macro fractures. Projecting the power law regressions established from micro fractures into the domain of macro fractures demonstrates that by measuring the former, I can aptly characterize the latter of the same fracture set (figure 2.9). Thus, one could accurately estimate macro fracture abundance (and therefore better characterize fluid flow) by measuring micro fractures. Therefore, because measuring macro fractures in the sub-surface is difficult (e.g., Narr and Suppe, 1991; Laubach, 2003), one could measure micro fractures in core and accurately estimate macro fracture intensities in the sub-surface.

I did not sample fractures from sub-surface core, however, previous workers have established that micro fractures can be used to predict macro fracture abundances on measurements from sub-surface core (e.g., Hooker et al., 2014). Fractures are commonly filled with minerals precipitated from fluids

circulating through fractures in the sub-surface. Thus, I infer that filled fractures exposed in the study area likely formed at depth. The sampled micro fractures, despite not being filled, show strong correlations in spacing and relative frequency to the filled macro fractures at the surface. Therefore I suggest that while micro fractures are not important for fluid flow (Laubach, 1997), they can serve as a proxy for estimating macro fracture distributions which are important for understanding fluid flow in reservoirs, thus, microfracture intensity measured in core may be a useful indicator of macrofracture intensity (c.f. Laubach, 1997).

My results indicate that in feldspathic and lithic sandstones, fracture size distributions can be quantified using cumulative frequency plots and power law regressions (figure 2.5-2.9). My observations suggest that fractures in the lithic and feldspathic sandstones follow power law scaling relationships across five orders of magnitude in a given fracture set (figure 2.9). This is consistent with previous work on scaling relationships of micro and macro fractures (e.g., Marrett et al., 1999; Hooker et al., 2009; 2014).

Table 2.3: Fracture Intensity Statistics by Set

Fracture Set	310	210	250	360
Maximum	20.53639	8.322538	8.721814	8.866363
Q3	8.480769	5.540687	6.440032	6.231078
Median	3.399201	3.601819	4.15825	4.683238
Q1	2.268229	2.55744	2.766318	3.64065
Minimum	1.403274	1.174606	1.374385	2.521124
Average	6.133049	4.052329	4.751483	5.18849
n =	15	8	3	4

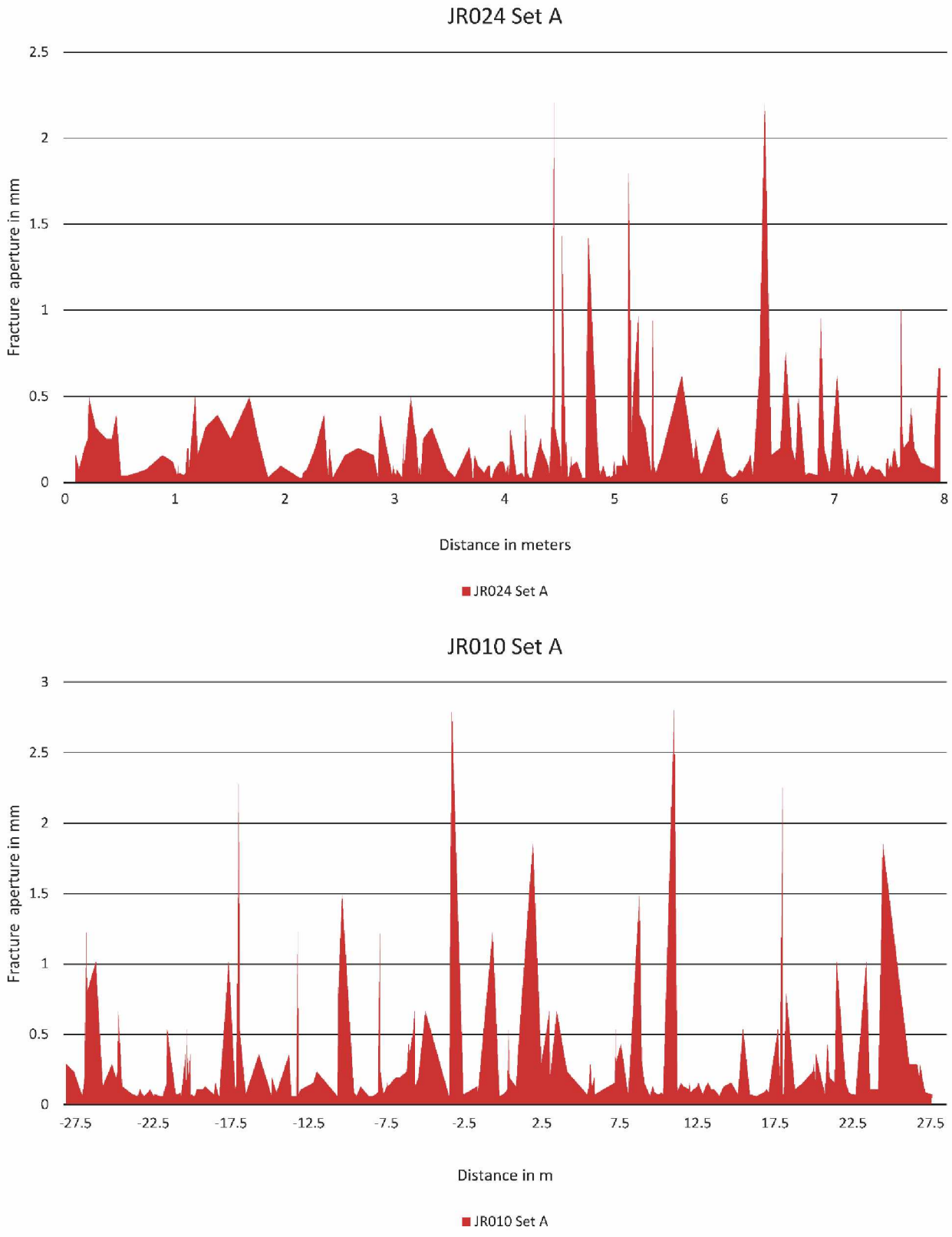

Figure 2.14 Fracture Aperture Size versus Distance along the Scan Line

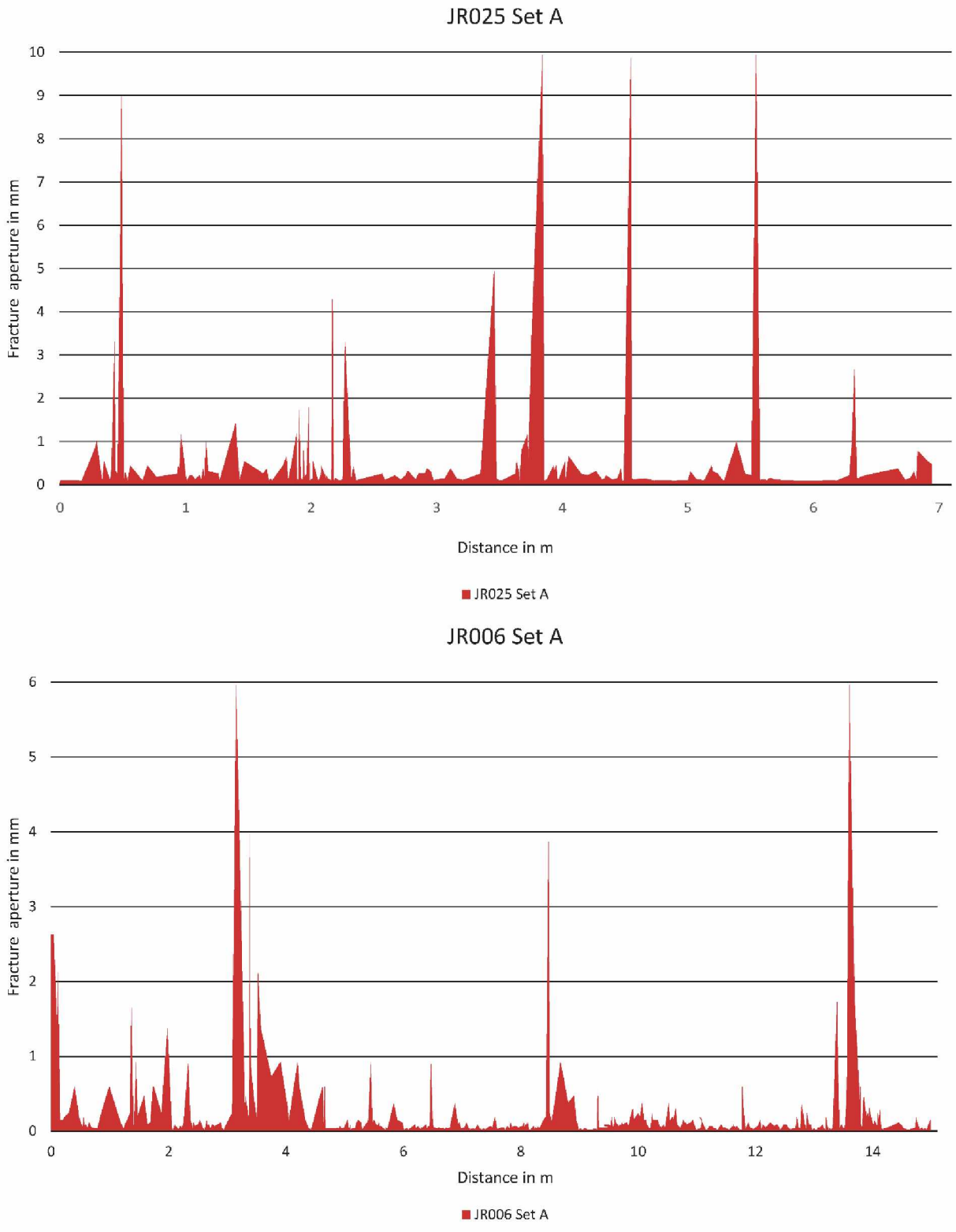

Figure 2.15 Fracture Aperture Size versus Distance along the Scan Line

Figure 2.15-2.16: Fracture aperture size versus distance along the scan line.
Fracture aperture size versus distance along the scan line. I chose four representative scan lines from the 310° fracture set. Station location and set denoted at top of graph. X axis has distance in meters along the scan line and y axis has width of fracture aperture in mm. See text for discussion.

Conclusions

Average fracture intensities for fractures ≥ 0.2 mm in the 310°, 210°, 250°, and 360° fracture sets are 6.13, 4.05, 4.75, and 5.1885, respectively. These fracture sets share similar fracture intensities, and despite being slightly different, the range of values from Q1 to Q3 is similar for all four fracture sets (figure 2.13). However, the 310 set has the highest recorded fracture intensity and the largest range.

Power law regression slopes that quantify the size normalized cumulative frequency plots suggest that the range and relative frequency of fracture sizes is similar for all formations across the study area (figure 2.11; 2.12). I suggest that a scaling exponent of -1.188 (± 0.504) would accurately quantify 95% of the slopes for future regressions done in the area.

Grain size does not correlate with fracture intensity in the studied strata, and thus, fracture intensity must be controlled by other variables. I hypothesize that lithologic parameters such as cement percentage, cement type, and facies might show a stronger correlation with fracture intensity, and that these variables should be taken into account for future work.

Fracture intensity locally increases near faults or other large fractures. Two outcrops (JR025 and JR026) located near the Bruin Bay fault show the highest FI in the study, while one outcrop near a small cross fault also shows higher fracture intensity (JR023). Similarly, fracture spacing data in figures 2.14 and 2.15 show that fractures of larger sizes cluster more closely together. I suggest that as fractures and faults open through progressive coalescence of smaller fractures, stress continues to accumulate in the surrounding rock body. When this stress accumulates in the surrounding rock body, other fractures will form, leaving behind permanent strain that localizes near areas where stress is concentrated (faults and large fractures). Thus, regions that could most likely serve as locations for concentrated fluid flow would be locations near large fractures, or small faults.

Micro fractures can be used as a proxy for determining the fracture intensity of macro fractures at larger scales. Micro fractures can accurately predict relative abundances of macro fractures within an order of magnitude (figure 2.9). Thus, I suggest that microfractural analysis of core, thin sections, and hand samples will effectively predict macro fracture intensity within one order of magnitude. Furthermore, my results show that feldspathic and lithic sandstones and siltstones follow power law spacing

relationships across five orders of magnitude, similar to other previously studied lithologies (e.g., Marrett et al., 1999; Ortega et al., 2010; Hooker et al., 2014).

Although there is little variation in fracture intensities between sets, the average fracture intensity for the 310° (Set A) fracture set is slightly greater than the others, and the 310° set has the largest range in fracture intensity (table 2.3). This fracture set is also the most likely to open or reopen under the modern stress regime (see Ruppert, 2008). Therefore, I suggest that the 310° fracture set likely has the greatest influence on fluid migration in the Cook Inlet Basin. Absolute ages of this fracture set are difficult to interpret. In chapter 1, I demonstrate that these fractures are at least Oligo-Miocene in age. Therefore, 310° fractures could have aided hydrocarbon migration in the Cook Inlet Basin since perhaps as early as Oligo-Miocene time.

3. General Conclusions

To understand the relationships of fractures and faults with regional deformation, I mapped fractures across a wide area in the southwestern Cook Inlet. I specifically mapped fracture orientations, fracture type, and relative fracture ages across all possible structural domains within the field area to constrain the genetic relationships of brittle deformation with folded and tilted strata as well as regional faults (e.g., Ahmadhadi et al., 2007; Lacombe et al., 2011; Branellec et al., 2015; Pastor-Galán et al., 2011). I attempt to constrain the possibility of small scale localized vertical axis rotations of fracture sets, using a widespread strike test (e.g., Pastor-Galán et al., 2011; Yonkee and Weil, 2010a; 2010b). In order to understand if the fracture sets observed in our study are part of a regional fracture system, I traced lineaments along the coast of our study area to constrain a regional deformation pattern (e.g., Ahmadhadi et al., 2008). The distribution of observed fracture sets, combined with relative ages determined from fold and strike tests, fracture stratigraphy, and cross cutting relationships allow me to make assertions as to the relative ages of mesoscopic brittle deformation with respect to folding and faulting in the region (e.g., Bergbauer and Pollard, 2004; Bellahsen et al., 2006; Engelder et al., 2009). The second portion of this study assesses the density of regionally mapped fracture sets, across five orders of magnitude in size, to address the scaling relationships of fractures in the Cook Inlet (e.g., Ortega et al., 2006), and determine if fracture density correlates with changes in structural position or lithology (e.g., Ortega et al., 2010; Savage and Brodsky 2011).

This study had three objectives:

1. What was the timeline of deformation in the Cook Inlet, and what were the major tectonic driver(s) for the deformation?
2. What controls fracture intensity within the fractured Mesozoic section of Cook Inlet?
3. What role do fractures play in the unconventional fractured resource potential of the region?

Chapter one addresses objective one. I identify four regionally present fracture sets within the Mesozoic – Cenozoic sedimentary section of the lower Cook Inlet. I interpret these four sets, oriented 360°, 310°, 250° and 210°, as having opened as a result of several tectonic events, initiating primarily in late Cretaceous – Early Paleocene and terminating after Oligo-Miocene or younger time. I interpret the oldest of these four fracture sets (360° fracture set) as having opened in response to N-S convergence

and subduction of the Kula plate in Late Cretaceous time. More 360° fractures and some 310° fractures formed as a conjugate pair during ridge subduction in early Cenozoic time roughly 52Ma. After the subduction of the Kula – Resurrection spreading ridge, the 250° and 310° fracture sets open and proliferate, respectively. This likely reflects a stress reversal after the removal of the compressional stresses from the colliding ridge. Lastly, the arrival of Yakutat in the late Oligocene or re-initiation of subduction after the passing of the ridge further proliferated the 310° fracture set, opened the 210° fracture set, and folded and tilted the Mesozoic and Cenozoic strata.

Chapter two addresses objectives two and three. I determine that rock type, formation, and grain size show no correlation with fracture intensity, and that it is likely that structural position plays the largest role in a rocks fracture intensity. I outline that scan lines on microscopic fractures correlate well with scan lines in macroscopic fractures. Studying micro fractures then could allow one to accurately characterize macro fracture abundance at the reservoir scale. This is enormously useful as measuring sub-surface fractures is notoriously difficult. These fractures are the most likely migration pathways for sub-surface hydrocarbons, as the rocks of the lower Cook Inlet are characterized by low permeability (Helmold et al., 2013).

Future Work

While I demonstrated a correlation between macrofractures and micro fractures at the surface, it would be useful for one to correlate micro fractures from sub-surface core with macro fractures from outcrop. Though the filled fractures at outcrops imply a sub-surface origin, it's still uncertain at what depth these fractures filled, and what caused the fractures to fill. If the mechanism for fracture fill was near surface groundwater mixing with connate water in the sub-surface, then it is possible that the majority of fractures in the sub-surface remain as open fluid flow pathways. These two research ideas (understanding fracture fill mechanisms and sub-surface micro fractures) would be excellent objectives for future work regarding the sub-surface reservoir potential of lower Cook Inlet.

Further field work in the Cretaceous strata south of Kamishak Bay, and in the Cenozoic strata north of Tuxedni Bay would serve as excellent objectives for further exploring stratigraphic partitions of fracture sets. By evaluating fracture stratigraphy in a larger interval of Cretaceous strata (rather than only one station in the Maastrichtian succession near saddle mountain in the study area) one could further

narrow down which fracture sets can be attributed to certain tectonic events, and potentially unravel the stress history of the Cretaceous in the forearc.

Intrusive dikes following fracture sets could help establish additional absolute age constraints for regional brittle deformation. Dikes were observed and sampled throughout the study area. Fractures commonly cross cut these dikes, and these dikes commonly intruded fracture sets. One dike at Ursus Head returned a geochronologic age of 33.6 Ma (J. Benowitz, 2016, Personal Correspondence). This dike was found heavily deformed in the hanging wall of the Bruin Bay Fault and would serve as an excellent timing constraint for slip on the fault. It could allow for connecting regional fracturing to regional faulting (see station JR025 for location at Ursus Head in Figure 2.1).

Paleomagnetic analysis for the sedimentary section in the Cook Inlet could also help confirm the amount of vertical axis rotation determined by this study. I show evidence of local vertical axis rotation of the four present fracture sets related to folding. Sampling south of Kamishak Bay and North of Tuxedni Bay would allow one to test for regional rotations (maybe due to oroclinal bending), local rotations (due to faulting or folding), or rotations stratigraphically (i.e. determining which stratigraphic units have experienced vertical axis rotation). While the estimations test for variability locally, a more regional sampling of fractures and paleomagnetic analysis could allow for a better regional understanding of deformation. While the effect of local small block rotations could skew analysis, it is likely that a regional sampling would effectively eliminate the noise from small scale structural variations (e.g., Yonkee and Weil, 2010a).

These data, combined with the data presented in this study, could be instrumental for interpreting forearc basin response to various tectonic events, and understanding the complex tectonic history of Alaska's southern margin.

References

Ahmadhadi, F., Lacombe, O., and Daniel, J., 2007, Early reactivation of basement faults in Central Zagros (SW Iran): evidence from pre-folding fracture populations in Asmari Formation and lower Tertiary paleogeography, in Thrust Belts and Foreland Basins; *From fold kinematics to hydrocarbon systems, Frontiers in Earth Sciences,* p. 205-228

Ahmadhadi, F., Daniel, J. M., Azzizadeh, M., and Lacombe, O., 2008, Evidence for pre-folding vein development in the Oligo-Miocene Asmari Formation in the Central Zagros Fold Belt, Iran, Tectonics v. 27, doi: 10.1029/2006TC001978, 22 pp.

Alaska Oil and Gas Conservation Commission (AOGCC), 2015, Well History Files On-line database. Last accessed November 17, 2015. http://aogweb.state.ak.us/WebLink8/Browse.aspx?dbid=0

Allmendinger, R. W., Cardozo, N. C., and Fisher, D., 2013, Structural Geology Algorithms: Vectors and Tensors: Cambridge, England, Cambridge University Press, 289 pp.

Amrouch, K., Lacombe, O., Bellahsen, N., Daniel, J., and Callot, J., 2010, Stress and strain patterns, kinematics and deformation mechanisms in a basement-cored anticline: Sheep Mountain Anticline, Wyoming: Tectonics, v.29, doi: 10.1029/2009TC002525, 27 pp.

Aydin, A., and Degraff, J. M., 1988, Evoluton of polygonal fracture patterns in lava flows: Science, v. 239, p. 471-476, doi: 239/4839/471

Bellahsen, N., Fiore, P., and Pollard, D. D., 2006, The role of fractures in the structural interpretation of Sheep Mountain Anticline, Wyoming: Journal of Structural Geology, v. 28, p. 850-867

Benowitz, J. A., Layer, P. W., and Vanlaningham, S., 2014, Persistent long-term (c. 24 Ma) exhumation in the Eastern Alaska Range constrained by stacked thermochronology: Geological Society, London, Special Publications, v. 378, p. 225-243

Benowitz, J. A., Haeussler, P. J., Layer, P. W., O'Sullivan, P. B., Wallace, W. K., and Gillis, R. J., 2012, Cenozoic tectono-thermal history of the Tordrillo Mountains, Alaska: Paleocene-Eocene ridge subduction, decreasing relief, and late Neogene faulting, Geochemical Geophysical Geosystems, 13, Q04009, doi:10.1029/2011GC003951

Bergbauer, S., and Pollard, D. D., 2004, A new conceptual fold-fracture model including prefolding joints, based on the Emigrant Gap anticline, Wyoming: Geological Society of America Bulletin, v. 116, p. 294-307

Betka, P. M., and Gillis, R. J., 2016, Observations on the Bruin Bay fault system between Chinitna and Tuxedni bays, Cook Inlet, Alaska, in Herriott, T.M., Petroleum-related geologic studies in lower Cook Inlet during 2015, Iniskin-Tuxedni region, south-central Alaska: Alaska Division of Geological and Geophysical Surveys Preliminary Interpretive Report 2016-1-10, p. 73-78. doi:10.14509/29544

Betka, P. M., and Gillis, R. J., 2015, The superposition of strike-slip and reverse-slip faults in the Bruin Bay fault system, Ursus Head, lower Cook Inlet, in Wartes, M.A., ed., Energy-related studies during the 2014 field season, western Cook Inlet, Alaska: Alaska Division of Geological and Geophysical Surveys Preliminary Interpretive Report 2015-5-2, p. 5-8. doi:10.14509/29457

Betka, P. M., and Gillis, R. J., 2014a, Preliminary characterization of brittle deformation on the Iniskin Peninsula: Implications for the kinematic history of the Bruin Bay fault system, lower Cook Inlet, Alaska: Alaska Division of Geological and Geophysical Surveys Preliminary Interpretive Report 2014-5, 14 p. doi:10.14509/29130

Betka, P. M., and Gillis, R. J., 2014b, Preliminary kinematic evidence for right-lateral slip along a system of steeply-dipping faults in the hanging wall of the Bruin Bay Fault, Iniskin Peninsula, lower Cook Inlet, Alaska, in Gillis, R.J., ed., Cook Inlet program 2013 field studies: Observations and preliminary interpretations from new 1:63,360-scale geologic mapping of the Iniskin Peninsula, lower Cook Inlet, Alaska: Alaska Division of Geological and Geophysical Surveys Preliminary Interpretive Report 2014-2-4, p. 17-22. doi:10.14509coe/27309

Blasko, D.P., 1976, Oil and gas seeps in Alaska, Alaska Peninsula, western gulf of Alaska: U.S. Bureau of Mines Report of Investigations 8122, 80 pp.

Bradley, D. C., Parrish, R., Clendenen, W., Lux, D., Layer, P., Heizler, M., and Donley, D.T., 2000, New geochronological evidence for the timing of early Tertiary ridge subduction in southern Alaska: US Geological Survey Professional Paper, v. 1615, p. 5-21

Bradley, D. C., Kusky, T. M., Haeussler, P. J., Goldfarb, R. J., Miller, M. L., Dumoulin, J. A., Nelson, S. W., and Karl, S. M., 2003, Geologic signature of Early Tertiary ridge subduction in Alaska, in Sisson, V. B., Roeske, S. M., and Pavlis, T. L., eds., Geology of a Transpressional Orogen Developed during Ridge-Trench Interaction along the North Pacific Margin: Geological Society of America Special Paper 371, p. 19–49

Branellec, M., Callot, J., Nivière, B., and Ringenbach, J., 2015, The fracture network, a proxy for mesoscale deformation: Constraints on layer parallel shortening history from the Malargüe fold and thrust belt, Argentina: Tectonics, v. 34, p. 623-647

Bruhn, R. L., and Haeussler, P. J., 2006, Deformation driven by subduction and microplate collision: Geodynamics of Cook Inlet basin, Alaska: Geological Society of America Bulletin, v. 118, p. 289-303

Byrne, T., 1979, Late Paleocene demise of the Kula-Pacific spreading center, Geology, v. 7, p. 341-344

Calderwood, K. W., and Fackler, W. C., 1972, Proposed stratigraphic nomenclature for the Kenai Group, American Association of Petroleum Geologists Bulletin v. 56, no. 4, p. 739-754

Cardozo, N., and Allmendinger, R. W., 2013, Spherical projections with OSXStereonet: Computers and Geosciences, v. 51, no. 0, p. 193 - 205, doi: 10.1016/j.cageo.2012.07.021

Clift, P. D., Draut, A. E., Kelemen, P. B., Bluszatajn, J., and Greene, A., 2005a, Stratigraphic and geochemical evolution of an oceanic arc upper crustal section: The Jurassic Talkeetna Volcanic Formation, south-central Alaska: Geological Society of America Bulletin, v. 117, no. 7/8, p. 902–925

Clift, P. D., Pavlis, T. L., DeBari, S. M., Draut, A. E., Rioux, M., and Kelemen, P. B., 2005b, Subduction erosion of the Jurassic Talkeetna-Bonanza arc and the Mesozoic accretionary tectonics of western North America: Geology, v. 33, p. 881–884

Cloos, M., 1993, Lithospheric buoyancy and collisional orogenesis: Subduction of oceanic plateaus, continental marginas, island arcs, spreading ridges, and seamounts: Geological Society of America Bulletin, v. 105, no. 6, p. 715-737

Coe, R. S., Globerman, B. R., Plumley, P. W., and Thrupp, G. A., 1985, Paleomagnetic results from Alaska and their tectonic implications, in Howell, D. G., ed., Tectonostratigraphic terranes of the circum-Pacific region: Circum- Pacific Council for Energy and Mineral Resources, Earth Science Series, no. 1, p. 85–108

Corrigan, J., Mann, P., and Ingle, J. C., 1990, Forearc response to subduction of the Cocos Ridge, Panama-Costa Rica: Geological Society of America Bulletin, v. 102, p. 628-652

Delaney, P. T., Pollard, D. D., Ziony, J. I., and McKee, E. H., 1986, Field relations between dikes and joints: emplacement processes and paleostress analysis: Journal of Geophysical Research: Solid Earth, v. 91, p. 4920-4938

Detterman, R. L., and Hartsock, J. K., 1966, Geology of the Iniskin-Tuxedni Peninsula region, Alaska: USGS Professional Paper 512, 78 p., 7 plates

Detterman, R. L., and Reed, B. L., 1980, Stratigraphy, structure, and economic geology of the Iliamna Quadrangle, Alaska: USGS Bulletin 1368-B, 86 p., scale 1:250,000, 1 plate

Dickenson, W. R., and Seely, D. R., 1979, Structure and Stratigraphy of Forearc Regions: American Association of Petroleum Geologists Bulletin, v. 63, p. 2-31

Dickinson, W. R., 1995, Forearc basins, in Busby, C. J., and Ingersoll, R. V., eds.: Tectonics of sedimentary basins: Blackwell Science, p. 221–261

Dominguez, S., Lallemand, S. E., Malavieille, J., and Von Huene, R., 1998, Upper plate deformation associated with seamount Subduction, Tectonophysics, v. 293, p. 207-224

Doubrovine, P. V., and Tarduno, J. A., 2008, A revised kinematic model for the relative motion between Pacific oceanic plates and North America since the Late Cretaceous, Journal of Geophysical Research, v. 113, doi:10.1029/2008JB005585

Eberhart-Phillips, D., Christensen, D. H., Brocher, T. M., Hansen, R., Ruppert, N. A., Haeussler, P. J., and Abers, G. A., 2006, Imaging the transition from Aleutian subduction to Yakutat collision in central Alaska, with local earthquakes and active source data: Journal of Geophysical Research, v. 111, doi:10.1029/2005JB004240

Engebretson, D. C., Cox, A., and Gordon, R. G., 1985, Relative motions between oceanic and continental plates in the Pacific Basin, Geological Society of America Special Papers, v. 206, 59 pp.

Engelder, T., and Geiser, P., 1980, On the use of regional joint sets as trajectories of paleostress fields during the development of the Appalachian Plateau, New York: Journal of Geophysical Research, v. 85, p. 6319-6341

Engelder, T., 1987, Joints and Shear Fractures in Rock, in Fracture Mechanics of Rock: Academic Press Incorporated (London) Limited, p. 27-38

Engelder, T., Lash, G. G., and Uzcátegui, R. S., 2009, Joint sets that enhance production from Middle and Upper Devonian gas shales of the Appalachian Basin: American Association of Petroleum Bulletin, v. 93, p. 857-889

Finzel, E. S., Trop, J. M., Ridgway, K. D., and Enkelmann, E., 2011, Upper plate proxies for flat-slab subduction processes in southern Alaska, Earth and Planetary Science Letters, 303(3-4), 348-360, doi: 10.1016/j.epsl.2011.01.014

Finzel, E. S., Ridgway, K. D., and Trop, J. M., 2015, Provenance signature of changing plate boundary conditions along a convergent margin: Detrital record of spreading-ridge and flat- slab subduction processes, Cenozoic forearc basins, Alaska, Geosphere, 11, doi: 10.1130/GES01029.1

Finzel, E.S., Enkelmann, E., Falkowski, S., and Hedeen, T., 2016, Long Term Forearc Basin Evoluion in Response to Changing Subduction Styles in Southern Alaska, Tectonics, 10.1002/TECT.20440

Fisher, M. A., and Magoon, L. B., 1978, Geologic framework of lower Cook inlet, Alaska: American Association of Petroleum Geologists Bulletin, v. 62, p. 373-402

Fletcher, H. J., and Freymueller, J. T., 2003, New constraints on the motion of the Fairweather fault, Alaska, from GPS observations: Geophysical Research Letters, v. 30, no. 3, p. 139–142

Friedman, M., 1969, Structural analysis of fractures in cores from Saticoy Field, Ventura County, California: American Association of Petroleum Geologists Bulletin, v. 53, p. 367-389.

Fuis, G. S., Moore, T. E., Plafker, G., Brocher, T. M., Fisher, M. A., Mooney, W. D., Nokleberg, W. J., Page, R. A., Beaudoin, B. C., Christensen, N. I., Levander, A. R., Lutter, W. J., Saltus, R. W., Ruppert, N. A., 2008, Trans-Alaska Crustal Transect and continental evolution involving subduction underplating and synchronous foreland thrusting. Geology, v. 36, p. 267–270.

Gardner, M., Bergman, S., Cushing, G., MacKevett, E., Plafker, G., Campbell, R., Dodds, C., McClelland, W., and Mueller, P., 1988, Pennsylvanian pluton stitching of Wrangellia and the Alexander terrane, Wrangell Mountains, Alaska: Geology, v. 16, p. 967-971.

Gillis, R. J., Reifenstuhl, R. R., and Decker, P. L., 2008, Implications of New Apatite and Zircon Fission Track Thermochronology for Mesozoic and Tertiary Basin Margin Exhumation, Upper Alaska Peninsula, 11th International Conference on Thermochronometry, Anchorage, Alaska, September 15th-19th, 2008: Alaska Division of Geological & Geophysical Surveys, 1 sheet

Gillis, R. J., Wartes, M. A., and O'Sullivan, P. B., 2011, Preliminary findings from reconnaissance structural studies along the Bruin Bay fault system and adjacent areas, south-central Alaska: American Association of Petroleum Geologists Pacific Section Meeting, Anchorage, Alaska, May 10, 2011: Alaska Division of Geological & Geophysical Surveys

Gillis, R. J., Maley, M. R., Frohman, R. A., and Peterson, C. S., 2013a, Fracture studies in Upper Cretaceous and Upper Jurassic strata on the upper Alaska Peninsula and lower Cook Inlet, in Gillis, R. J., ed., Overview of 2012 field studies: Upper Alaska Peninsula and west side of lower Cook Inlet, Alaska: Alaska Division of Geological and Geophysical Surveys Preliminary Interpretive Report 2013-1D, p. 13-17. doi:10.14509/24847

Gillis, R. J., Swenson, R. F., Wartes, M. A., and Frohman, R. A., 2013b, Reconnaissance investigations of the Bruin Bay fault system along the western margin of lower Cook Inlet and upper Alaska Peninsula, in Gillis, R. J., ed., Overview of 2012 field studies: Upper Alaska Peninsula and west side of lower Cook Inlet, Alaska: Alaska Division of Geological and Geophysical Surveys Preliminary Interpretive Report 2013-1G, p. 33-37. doi:10.14509/24850

Gillis, R. J., Shellenbaum, D. P., Herriot, T. M., Mauel, D. J., Wartes, M. A., Decker, P. L., Freeman, L. K., Lepain, D. L., Gregerson, L. S., Elliott, B. A., Benowitz, J. A., and O'Sullivan, P. B., 2016, Results of new 1:63,360-scale geologic mapping and related field studies in the south-central Tyonek Quadrangle, south-central Alaska: Middle Eocene transtension and post-Oligocene inversion on the northwest periphery of the Cook Inlet forearc basin, Alaska Geological Society Technical Conference, Program with Abstracts, p. 20

Glen, J. M. G., 2004, A kinematic model for the southern Alaska orocline based on regional fault patters, in Sussman, A. J., and Weil, A. B., eds., Orogenic Curvature: Integrating Paleomagnetic and Structural Analyses: Geological Society of America Special Paper 383, p. 161–172

Gomez, L. A., and Laubach, S. E., 2006, Rapid digital quantification of microfracture populations: Journal of Structural Geology, v. 28, p. 408–420

Haeussler, P. J., Bradley, D. C., Wells, R. E., and Miller, M. L., 2003, Life and death of the Resurrection plate: Evidence for its existence and subduction in the northeastern Pacific in Paleocene–Eocene time: Geological Society of America Bulletin, v. 115, p. 867-880

Haeussler, P. J., Bruhn, R. L., and Pratt, T. L., 2000, Potential seismic hazards and tectonics of the upper Cook Inlet basin, Alaska, based on analysis of Pliocene and younger deformation: Geological Society of America Bulletin, v. 112, p. 1414-1429

Hampton, B. A., Ridgway, K. D., O'Neill, J. M., Gehrels, G. E., Schmidt, J., and Blodgett R. B., 2007, Pre-, syn-, and postcollisional stratigraphic framework and provenance of Upper Triassic-Upper Cretaceous strata in the northwestern Talkeetna Mountains, Alaska, in *Tectonic Growth of a Collisional Continental Margin: Crustal Evolution of Southern Alaska*, Geological Society of America Special Paper, pp. 401-438

Hancock, P., 1985, Brittle microtectonics: principles and practice: Journal of Structural Geology, v. 7, p. 437-457

Harrison, T. M, Heizler, M. T., Lovera, O. M., Wenji, C., Grove, M., 1994, A chlorine disinfectant for excess argon released from K-feldspar during step heating Earth Planetary Science Letters, v. 123, p. 95–104

Helmold, K. P., LePain, D. L., Wilson, M. D., and Peterson, C. S., 2013, Petrology and reservoir potential of Tertiary and Mesozoic sandstones, Cook Inlet, Alaska: A preliminary analysis of outcrop samples collected during 2007-2010 field seasons: Alaska Division of Geological & Geophysical Surveys Preliminary Interpretive Report 2013-5, 34 pp.

Herriot, T. M., Wartes, M. A., and Decker, P. L., 2016, Deep-Water Canyons and Sequence Stratigraphic Framework of the Upper Jurassic Naknek Formation, Cook Inlet Forearc Basin, South-Central Alaska, Alaska Division of Geological and Geophysical Surveys Report of Investigations (in press)

Hooker, J., Gale, J., Gomez, L., Laubach, S., Marrettt, R., and Reed, R., 2009, Aperture-size scaling variations in a low-strain opening-mode fracture set, Cozzette Sandstone, Colorado: Journal of Structural Geology, v. 31, p. 707-718

Hooker, J., Laubach, S., and Marrettt, R., 2014, A universal power-law scaling exponent for fracture apertures in sandstones: Geological Society of America Bulletin, v. 126, p. 1340-1362

Hudson, L., Plafker, G., and Peterman, Z. E., 1979, Paleogene anatexis along the Gulf of Alaska margin: Geology, v. 7, p. 573-577

Hults C. P., Wilson F. H., Donelick R. A., O'Sullivan P. B., 2013, Two flysch belts having distinctly different provenance suggest no stratigraphic link between the Wrangellia composite terrane and the paleo-Alaskan margin: Lithosphere, v. 5, p. 575–594.

Kirschner, C. E., and Minard, D. L., 1949, Geology of the Iniskin Peninsula, Alaska: U.S. Geol. Survey Oil and Gas Investigations Preliminary Map 95, scale: 1 inch=4,000 feet.

Kirschner, C., and Lyon, C., 1973, Stratigraphic and tectonic development of Cook Inlet petroleum province: Arctic Geology: American Association of Petroleum Geologists Memoir, v. 19, p. 396-407

Kulander, B. K., Barton, C. C., and Dean, S. L., 1979, Applications of Fractography to Core and Outcrop Investigations: US Department of Energy METC, v. 3, 79 pp.

Lacombe, O., Bellahsen, N., and Mouthereau, F., 2011, Fracture patterns in the Zagros Simply Folded Belt (Fars, Iran): constraints on early collisional tectonic history and role of basement faults: Geological Magazine, v. 148, p. 940-963

Laubach, S. E., 2003, Practical approaches to identifying sealed and open fractures: American Association of Petroleum Bulletin, v. 87, p. 561-579

Laubach, S. E., 1997, A method to detect natural fracture strike in sandstones: American Association of Petroleum Bulletin, v. 81, p. 604-623

Laursen, J., Scholl, D. W., and Von Huene, R., 2002, Neotectonic deformation of the Central Chile Margin: Deepwater forearc basin formation in response to hot spot ridge and seamount subduction: Tectonics, Vol. 21, No. 5, 1038, doi: 10.1029/2001TC901023

Layer, P. W., Hall, C. M. and York, D., 1987, The derivation of 40Ar/39Ar age spectra of single grains of hornblende and biotite by laser step heating: Geophysical Research Letters, v. 14, 757-760

LePain, D. L., Stanley, R. G., Gillis, R. J., Helmold, K. P., Peterson, C. S., and Wartes, M. A., 2011, Deposition of Middle Jurassic Tuxedni Group, lower Cook Inlet, Alaska: Initial exhumation of an Early Jurassic island arc and incipient motion on the Bruin Bay fault zone: Program with Abstracts, American Association of Petroleum Geologists Pacific Section Annual Meeting, p. 71

LePain, D., Stanley, R., Helmold, K., and Shellenbaum, D., 2013, Geologic framework and petroleum systems of Cook Inlet basin, south-central Alaska: Oil and Gas Fields of the Cook Inlet Basin, Alaska: American Association of Petroleum Memoir, v. 104, p. 37-116

Lianbo, Z., and Xiang-Yang, L., 2009, Fractures in sandstone reservoirs with ultra-low permeability: A case study of the Upper Triassic Yanchang Formation in the Ordos Basin, China: American Association of Petroleum Bulletin, v. 93, p. 461-477

Lillis, P. G., and R. G. Stanley, 2011, Petroleum generation modeling for Cook Inlet Basin, Alaska: American Association of Petroleum Geologists, Program with Abstracts, Pacific Section Annual Meeting, p. 72

Lonsdale, P., 1988, Paleogene history of the Kula plate - offshore evidence and onshore implications: Geological Society of America Bulletin, v. 99, p. 733-754, doi:10.1130/00167606

Madsen, J. K., Thorkelson, D. J., Friedman, R. M., and Marshall, D. D., 2006, Cenozoic to Recent plate configurations in the Pacific Basin: Ridge subuction and slab window magmatism in North America: Geosphere, v. 2, no.1, p. 11-34, doi: 10.1130/GES00020.1

Magoon, L. B., Egbert, R. M., and Petering, G., 1978, Upper Jurassic and Cretaceous rocks of the Kamishak Hills-Douglas River area, lower Cook Inlet: USGS Circular 772-B, p. B57–B59

Magoon, L., and Anders, D., 1990, Oil-source rock correlation using carbon isotope data and biological marker compounds, Cook Inlet-Alaska Peninsula, Alaska: American Association of Petroleum Bulletin, v. 74, 25 pp.

Magoon, L. B., 1994, Tuxedni-Hemlock (!) petroleum system in Cook Inlet, Alaska: American Association of Petroleum Geologists Memoirs, v. 60, p. 359-359

Magoon, L. B., 1986, Geologic Studies of the Lower Cook Inlet COST No. 1 Well, Alaska Outer Continental Shelf: US Geological Survey Bulletin, v. 1596, 88 pp.

Magoon, L. B., and Claypool, G. E., 1981, Petroleum geology of Cook Inlet basin--an exploration model: American Association of Petroleum Bulletin, v. 65, p. 1043-1061

Magoon, L. B., Griesbach, F. B., and Egbert, R. M., 1980, Nonmarine Upper Cretaceous Rocks, Cook Inlet, Alaska: American Association of Petroleum Bulletin, v. 64, p. 1259-1266

Marrettt, R., Ortega, O. J., and Kelsey, C. M., 1999, Extent of power-law scaling for natural fractures in rock: Geology, v. 27, p. 799-802

McDougall, I. and Harrison, T. M., 1999, Geochronology and Thermochronology by the 40Ar/39Ar method-2nd ed: Oxford University Press, 269 pp.

Meigs, A., Johnston, S., Garver, J., and Spotila, J., 2008, Crustal-scale structural architecture, shortening, and exhumation of an active, eroding orogenic wedge (Chugach/St. Elias Range, southern Alaska): Tectonics, v. 27, doi:10.1029/2007TC002168

Mobasher, K., and Babaie, H. A., 2008, Kinematic significance of fold-and fault-related fracture systems in the Zagros mountains, southern Iran: Tectonophysics, v. 451, p. 156-169

Moll-Stalcup, E. J., 1994, Latest Cretaceous and Cenozoic magmatism in mainland Alaska, in Plafker, G., and Berg, H.C., eds., The Geology of Alaska: Boulder, Colorado, Geological Society of America, Geology of North America, v. G-1, p. 589–619

Moore, J. C., Byrne, T., Plumley, P. W., Reid, M., Gibbons, H., and Coe, R. S., 1983, Paleogene evolution of the Kodiak Islands, Alaska: Consequences of ridge-trench interaction in a more southerly latitude: Tectonics, v. 2, p. 265-293

Narr, W., 1996, Estimating average fracture spacing in sub-surface rock: American Association of Petroleum Bulletin, v. 80, p. 1565-1585

Narr, W., 1991, Fracture Density in the Deep Sub-surface: Techniques with Application to Point Arguello Oil Field (1): American Association of Petroleum Bulletin, v. 75, p. 1300-1323

Narr, W., and Suppe, J., 1991, Joint spacing in sedimentary rocks: Journal of Structural Geology, v. 13, p. 1037-1048

Nelson, R. A., 1985, Geologic analysis of naturally fractured reservoirs: Houston, Gulf Publishing, 320 pp.

Nokleberg, W. J., Parfenov, L. M., Monger, J. W. H., Norton, I. O., Khanchuck, A. I., Stone, D. B., Scotese, C. R., Scholl, D. W., and Fujita, K., 2001, Phanerozoic tectonic evolution of the Circum-North Pacific: U.S. Geological Survey Professional Paper 1626, 122 pp.

Nokleberg, W.J., Plafker, G., and Wilson, F.H., 1994, Geology of south-central Alaska, in Plafker, G., and Berg, H. C., eds., The geology of Alaska: GSA, The geology of North America, v. G-1, p. 311–366

Ortega, O. J., Gale, J. F., and Marrettt, R., 2010, Quantifying diagenetic and stratigraphic controls on fracture intensity in platform carbonates: an example from the Sierra Madre Oriental, northeast Mexico: Journal of Structural Geology, v. 32, p. 1943-1959

Ortega, O. J., Marrettt, R. A., and Laubach, S. E., 2006, A scale-independent approach to fracture intensity and average spacing measurement: American Association of Petroleum Bulletin, v. 90, p. 193-208

Ortega, O., and Marrettt, R., 2000, Prediction of macro fracture properties using micro fracture information, Mesaverde Group sandstones, San Juan basin, New Mexico: Journal of Structural Geology, v. 22, p. 571-588

Pastor-Galán, D., Gutiérrez-Alonso, G., and Weil, A. B., 2011, Orocline timing through joint analysis: Insights from the Ibero-Armorican Arc: Tectonophysics, v. 507, p. 31-46

Pavlis, T. L., and Roeske, S. M., 2007, The Border Ranges fault system, southern Alaska, in Ridgway, K. D., Trop, J. M., Glen, J. M. G., and O'Neill, J.M., eds., Tectonic Growth of a Collisional Continental Margin: Crustal Evolution of Southern Alaska: Geological Society of America Special Papers, v. 431, doi: 10.1130/2007.2431(05)

Pavlis, T. L., and Sisson, V. B., 2003, Development of a subhorizontal decoupling horizon in a transpressional system, Chugach metamorphic complex, Alaska: Evidence for rheological stratification of the crust, in Sisson, V. B., Roeske, S. M., and Pavlis, T. L., eds., Geology of a Transpressional Orogen Developed during Ridge-Trench Interaction along the North Pacific Margin: Geological Society of America Special Papers, v. 371, p. 191–216

Plafker, G., 1987, Regional geology and petroleum potential of the northern Gulf of Alaska continental margin, in Scholl, D. W., Grantz, A., and Vedder, J. G., eds., Geology and Resource Potential of the Continental Margin of Western North America and Adjacent Ocean Basins: Houston, Texas, Circum-Pacific Council for Energy and Mineral Resources, Earth Science Series, v. 6, p. 229–268

Plafker, G., and Berg, H. C., 1994, Overview of the geology and tectonic evolution of Alaska, in Plafker, G., and Berg, H. G., eds., The Geology of Alaska: Boulder, Colorado, Geological Society of America, Geology of North America, v. G-1, p. 989–1021

Plafker, G., Moore, J. C., and Winkler, G. R., 1994, Geology of the southern Alaska margin, in Plafker, G., and Berg, H. G., eds., The Geology of Alaska: Boulder, Colorado, Geological Society of America, Geology of North America, v. G-1, p. 389–450

Plafker, G., Nokleberg, W. J., and Lull, J. S., 1989, Bedrock geology and tectonic evolution of the Wrangellia, Peninsular, and Chugach terranes along the Trans-Alaskan Crustal Transect in the northern Chugach Mountains and southern Copper River basin, Alaska: Journal of Geophysical Research, v. 94, p. 4255–4295

Pollard, D. D., and Aydin, A., 1988, Progress in understanding jointing over the past century: Geological Society of America Bulletin, v. 100, p. 1181-1204

Pollard, D., and Segall, P., 1987, Theoretical displacements and stresses near fractures in rock: with applications to faults, joints, veins, dikes, and solution surfaces: Fracture Mechanics of Rock, v. 277, p. 277-349

Price, N. J., 1966, Fault and Joint Development in Brittle and Semi-Brittle Rock: Pergamon Press, Oxford, 176 pp.

Renne, P. R., Deino, A. L., Walter, R. C., Turrin, B. D., Swisher, C. C., Becker, T. A., Curtis, G. H., Sharp. W. D., and Jaouni, A. R., 1994, Intercalibration of astronomical and radioisotopic time. Geology, v. 22, p. 783-786

Ridgway, K., Skulski, T., and Sweet, A., 1986, Cenozoic strike-slip tectonics along the Duke River Fault, St. Elias Mountains; Intracontinental transform fault response to terrane accretion: Geological Society of America Abstracts with Programs, p. 313

Ridgway, K. D., Skulski, T., and Sweet, A. R., 1996, Cenozoic strike-slip tectonics along the Duke River fault, St. Elias Mountains: Intracontinental transform fault response to terrane accretion: Geological Society of America Abstracts with Programs, v. 28, no. 7, p. 313

Ridgway, K. D., Trop, J. M., Nokleberg, W. J., Davidson, C. M., and Eastham, K. D., 2002, Mesozoic and Cenozoic tectonics of the eastern and central Alaska Range: Progressive basin development and deformation within a suture zone: Geological Society of America Bulletin, v. 114, p. 1480–1504

Rioux, M., Hacker, B., Mattinson, J., Kelemen, P., Blusztajn, J., Hanghoj, K., and Amato, J., 2006, Tectonic and geochemical evolution of the accreted Talkeetna arc, south-central Alaska: Implications for a type section of intra-oceanic arc crust: AGU Fall Meeting Abstracts, p. 07

Rives, T., Rawnsley, K., and Petit, J., 1994, Analogue simulation of natural orthogonal joint set formation in brittle varnish: Journal of Structural Geology, v. 16, p. 419-429

Roeske, S. M., Snee, L. W., and Pavlis, T. L., 2003, Dextral-slip reactivation of an arc-forearc boundary during Late Cretaceous-Early Eocene oblique convergence in the northern Cordillera: Geological Society of America Special Papers, v. 371, p. 141-169

Rosenthal, J. L., Betka, P. M., Nadin, E. S., and Gillis, R. J., 2015b, Deformational history and fracture intensity of the Iniskin Peninsula, Cook Inlet, Alaska: Geological Society of America, Abstracts with Programs vol. 47, no. 4, p. 21

Rosenthal, J. L., Betka, P. M., Gillis, R. J., and Nadin, E. S., 2015a, Preliminary investigation of fracture populations in Mesozoic strata of the Cook Inlet forearc basin: Iniskin Peninsula and Lake Clark National Park, Alaska, in Wartes, M. A., ed., Energy-related studies during the 2014 field season, western Cook Inlet, Alaska: Alaska Division of Geological and Geophysical Surveys Preliminary Interpretive Report 2015-5-3, p. 9–13, doi:10.14509/29458

Rosenthal, J. L., Betka, P. M., Gillis, R. J., and Nadin, E., 2016, Fracture intensity in the Paveloff Siltstone Member (Chinitna Formation) and Pomeroy Arkose Member (Naknek Formation), Iniskin Peninsula, Alaska: Implications for hydrocarbon migration in Cook Inlet basin, in Herriott, T. M., Petroleum-related geologic studies in lower Cook Inlet during 2015, Iniskin-Tuxedni region, south-central Alaska: Alaska Division of Geological and Geophysical Surveys Preliminary Interpretive Report 2016-1-9, p. 67-72. doi:10.14509/29543ogical Society of America, p. 141-170

Ruppert, N. A., 2008, Stress map for Alaska from earthquake focal mechanisms: Active Tectonics and Seismic Potential of Alaska, p. 351-367

Samson, S. D., and Alexander, E. C., 1987 Calibration of the interlaboratory 40Ar/39Ar dating standard, MMhb1: Chemistry and Geology, v. 66, 27-34

Savage, H. M., and Brodsky, E. E., 2011, Collateral damage: Evolution with displacement of fracture distribution and secondary fault strands in fault damage zones: Journal of Geophysical Research: Solid Earth, v. 116, 14 pp.

Schwartz, S. Y., and R. Van der Voo (1983), Paleomagnetic evaluation of the orocline hypothesis in the central and southern Appalachians, Geophysical Research Letters, v. 10, p. 505–508

Sinclair, S. W., 1980, Analysis of macroscopic fractures on Teton anticline, northwestern Montana: M.S. thesis, Texas A&M University, College Station, Texas, 102 pp.

Sisson, V. B., and Pavlis, T. L., 1993, Geological consequences of plate reorganization: An example from the Eocene southern Alaska fore arc: Geology, v. 21, p. 913–916

Stanley, R. G., Pierce, B. S., and Houseknecht, D. W., 2011, US Geological Survey 2011 Assessment of Undiscovered Oil and Gas Resources of the Cook Inlet Region, South-Central Alaska, USGS Fact Sheets, v. 3068, 2 pp.

Stearns, D. W., and Friedman, M., 1972, Reservoirs in fractured rock: Geologic exploration methods: in *Stratigraphic Oil and Gas Fields--Classification, Exploration Methods, and Case Histories*, p. 82-106

Stephenson, B. J., Koopman, A., Hillgartner, H., McQuillan, H., Bourne, S., Noad, J. J., and Rawnsley, K., 2007, Structural and stratigraphic controls on fold-related fracturing in the Zagros Mountains, Iran: implications for reservoir development: Geological Society of London Special Publications, v. 270, p. 1-21

Triplehorn, D., Turner, D. L., and Naeser, C. W., 1984, Radiometric age of the Chickaloon Formation of south-central Alaska: Location of the Paleocene - Eocene boundary, Geological Society of America Bulletin, v. 95, p. 740-742

Trop, J. M., 2008, Latest Cretaceous forearc basin development along an accretionary convergent margin: South-central Alaska: Geological Society of America Bulletin, v. 120, p. 207-224

Trop, J. M., and Ridgway, K. D., 2007, Mesozoic and Cenozoic tectonic growth of southern Alaska: A sedimentary basin perspective: Geological Society of America Special Papers, v. 431, p. 55-94

Trop, J. M., Hampton, B., Ridgway, K., and Gehrels, G., 2005, Latest Cretaceous sedimentary record of forearcarc-retroarc relationships in south-central Alaska, in Geological Society of America Annual Meeting, Salt Lake City, Program with Abstracts, p. 81

Trop, J. M., Ridgway, K. D., Manuszak, J. D., and Layer, P. W., 2002, Sedimentary basin development on the allochthonous Wrangellia composite terrane, Mesozoic Wrangell Mountains basin, Alaska: Along-term record of terrane migration and arc construction: Geological Society of America Bulletin, v. 114, p. 693–717

Trop, J. M., and Ridgway, K. D., 1999, Sedimentology and provenance of the Paleocene-Eocene Arkose Ridge Formation, Cook Inlet-Matanuska Valley forearc basin, southern Alaska: Short notes on Alaskan geology, Alaska Division of Geological and Geophysical Surveys: Professional Report, v. 119, p. 129–144

Wallace, W. K., and Engebretson, D. C., 1984, Relationships between plate motions and Late Cretaceous to Paleogene magmatism in southwestern Alaska: Tectonics, v. 3, p. 295-315

Wartes, M. A., T. M. Herriott, K. P. Helmold, R. J. Gillis, D. L. LePain, and R. G. Stanley, 2011, Stratigraphic evidence for Late Jurassic activity on the Bruin Bay fault, Iniskin Peninsula, lower Cook Inlet, Alaska: Programs with Abstracts American Association of Petroleum Geologists, Pacific Section Annual Meeting, p. 96

Wartes, M. A., Herriott, T. M., Helmold, K. P., and Gillis, R. J., 2013, Preliminary stratigraphic interpretation of the Naknek Formation: Evidence for Late Jurassic activity on the Bruin Bay fault, Iniskin Peninsula, lower Cook Inlet, in Gillis, R. J., ed., Overview of 2012 field studies: Upper Alaska Peninsula and west side of lower Cook Inlet, Alaska: Alaska Division of Geological and Geophysical Surveys Preliminary Interpretive Report 2013-1H, p. 39-46, doi:10.14509/24851

Wartes, M. A., and Herriott, T. M., 2014, A new occurrence of oil-stained rocks within a small fault zone involving the Middle Jurassic Cynthia Falls Formation, Tuxedni Group, northern Iniskin Peninsula, in Gillis, R. J., ed., Cook Inlet program 2013 field studies—Observations and preliminary interpretations from new 1:63,360-scale geologic mapping of the Iniskin Peninsula, lower Cook Inlet, Alaska: Alaska Division of Geological and Geophysical Surveys Preliminary Interpretive Report 2014-2-5, p. 23–27

Weil, A. B., and Yonkee, W. A., 2012, Layer-parallel shortening across the Sevier fold-thrust belt and Laramide foreland of Wyoming: spatial and temporal evolution of a complex geodynamic system: Earth and Planetary Science Letters, v. 357, p. 405-420

Winkler, G. R., 2000, A geologic guide to Wrangell-Saint Elias National Park and Preserve, Alaska: A tectonic collage of northbound terranes: USGS Professional Paper 1616, 188 p.

Wolfe, J. A., Hopkins, D. M., and, Leopold, E. B., 1966, Tertiary Stratigraphy and Paleobotany of the Cook Inlet Region, Alaska: Discussion of stratigraphic significance of fossil plants from the Chickaloon, Kenai, and Tsadaka Formations, United States Geological Survey Professional Paper, v. 398-A, 33 pp.

Wolfe, J. A., 1969, Paleogene floras from the Gulf of Alaska Region: United States Geological Survey Professional Paper, v. 997, 108 pp.

Yamazaki, T., and Yukinobu, O., 1989, Subducting seamounts and deformation of overriding forearc wedges around Japan: Tectonophysics, v. 160, p. 207-229

Yonkee, A., and Weil, A. B., 2010a, Quantifying vertical axis rotation in curved orogens: Correlating multiple data sets with a refined weighted least squares strike test: Tectonics, v. 29, 31 pp.

Yonkee, A., and Weil, A. B., 2010b, Reconstructing the kinematic evolution of curved mountain belts: Internal strain patterns in the Wyoming salient, Sevier thrust belt, USA: Geological Society of America Bulletin, v. 122, p. 24-49

York, D., Hall, C. M., Yanase, Y., Hanes, J. A. and Kenyon, W. J., 1981, 40Ar/39Ar dating of terrestrial minerals with a continuous lasers: Geophysical Research Letters, v. 8, p. 1136-1138

Zeumann, S., and Hampel, A., 2015, Deformation of erosive and accretive forearcs during subduction of migrating and non-migrating aseismic ridges: Results from 3-D finite element models and application to the Central American, Peruvian, and Ryukyu margins: Tectonics, v. 34, p. 1769-1791

Appendix

Definitions for Supplemental Files

Fracture Orientations

Fractures have been back-tilted and rotated about a vertical axis to a common reference strike (40°). Data are color coded by fracture set: Red = 310°; Light Red = Possible 310°; Green = 360°; Light Green = Possible 360°; Blue = 250°; Light Blue = Possible 250°; Orange = 210°; Light Orange = Possible 210°; Tan/Gold = Noise or otherwise unidentified. Fracture sets are delimited into individual sheets.

Macro fracture Scan lines

Scan lines data are organized by formation, station, and then fracture set sampled. Distances along scan line and apertures are in mm.

Micro fracture Scan lines

Scan lines data are organized by location. Fracture set sampled in title of excel spreadsheet. Within spread sheet, observation, and aperture in mm are listed.